

IMI-La Trobe Joint Conference

Mathematics for Materials Science and Processing

Editors: Institute of Mathematics for Industry, Kyushu University - Australia Branch

九州大学マス・フォア・インダストリ研究所

IMI-La Trobe Joint Conference

**Mathematics for Materials
Science and Processing**

Editors: Institute of Mathematics for Industry,
Kyushu University — Australia Branch

About MI Lecture Note Series

The Math-for-Industry (MI) Lecture Note Series is the successor to the COE Lecture Notes, which were published for the 21st COE Program “Development of Dynamic Mathematics with High Functionality,” sponsored by Japan’s Ministry of Education, Culture, Sports, Science and Technology (MEXT) from 2003 to 2007. The MI Lecture Note Series has published the notes of lectures organized under the following two programs: “Training Program for Ph.D. and New Master’s Degree in Mathematics as Required by Industry,” adopted as a Support Program for Improving Graduate School Education by MEXT from 2007 to 2009; and “Education-and-Research Hub for Mathematics-for-Industry,” adopted as a Global COE Program by MEXT from 2008 to 2012.

In accordance with the establishment of the Institute of Mathematics for Industry (IMI) in April 2011 and the authorization of IMI’s Joint Research Center for Advanced and Fundamental Mathematics-for-Industry as a MEXT Joint Usage / Research Center in April 2013, hereafter the MI Lecture Notes Series will publish lecture notes and proceedings by worldwide researchers of MI to contribute to the development of MI.

October 2014
Yasuhide Fukumoto
Director
Institute of Mathematics for Industry

IMI-La Trobe Joint Conference

Mathematics for Materials Science and Processing

MI Lecture Note Vol.67, Institute of Mathematics for Industry, Kyushu University
ISSN 2188-1200

Date of issue: February 5, 2016

Editors: Institute of Mathematics for Industry, Kyushu University — Australia Branch

Publisher:

Institute of Mathematics for Industry, Kyushu University

Graduate School of Mathematics, Kyushu University

Motooka 744, Nishi-ku, Fukuoka, 819-0395, JAPAN

Tel +81-(0)92-802-4402, Fax +81-(0)92-802-4405

URL <http://www.imi.kyushu-u.ac.jp/>

Printed by

Kijima Printing, Inc.

Shirogane 2-9-6, Chuo-ku, Fukuoka, 810-0012, Japan

TEL +81-(0)92-531-7102 FAX +81-(0)92-524-4411

IMI-La Trobe Joint Conference:

Mathematics for Materials Science and Processing

Venue: Institute for Advanced Studies, La Trobe University, Melbourne

Dates: Feb.15(Mon)-Feb.17(Wed), 2016

Organising committee:

Philip Broadbridge	La Trobe University / Kyushu University
Pierluigi Cesana	IMI Australia Branch, Kyushu University / La Trobe University
Dimetre Triadis	IMI Australia Branch, Kyushu University / La Trobe University
Trina Dreher	Suez Oil & Gas Sysytems
Kenji Kajiwara	IMI, Kyushu University

This is a 3-day international conference organised jointly by the Department of Mathematics and Statistics, La Trobe University and the Institute of Mathematics for Industry, Kyushu University, also held as a Joint Use Research Program - Conference Category (I) supported by the Ministry of Education, Culture, Sports, Science and Technology of Japan (MEXT).

Industrial collaboration and industrially relevant research are major objectives of the conference. One can identify two broad research groups engaged in solid mechanics, fluid mechanics and nanotechnology. On the one hand many academics are engaged with technical issues of uniqueness and existence for various boundary value problems. Conversely, the focus of many engineers and industrial researchers is on computational fluid dynamics for simulating complicated systems of industrial relevance.

There is clear potential and reward for both camps moving towards one another through collaboration. With an awareness of pressing industrial problems, academics may provide valuable insights into standard and limiting system behaviour that are not clear through simulation. Such insights can often be incorporated into computational algorithms by engineers who are engaged with theoreticians, increasing accuracy and enabling more challenging systems to be simulated.

This conference aims to foster communication and collaboration between disparate groups, drawing many into the middle ground for the benefit of all.

Australia Branch
Institute of Mathematics for Industry
Kyushu University

IMI-La Trobe Joint Conference

Mathematics for Materials Science and Processing



Dates: **Feb.15 (Mon.)–Feb.17 (Wed.), 2016**

Invited speakers:

Bob Anderssen, CSIRO Australia

Philip Broadbridge, La Trobe University

David Boger, The University of Melbourne

Veronique Bonnelye, Suez Water & Treatment Solutions

Trina Dreher, Suez Oil & Gas Systems

Yasuhide Fukumoto, IMI, Kyushu University

Tony Guttman, The University of Melbourne

Bronwyn Hajek, University of South Australia

Shaun Hendy, University of Auckland

Keisuke Matsuya, Musashino University, Tokyo

Mark Nelson, University of Wollongong

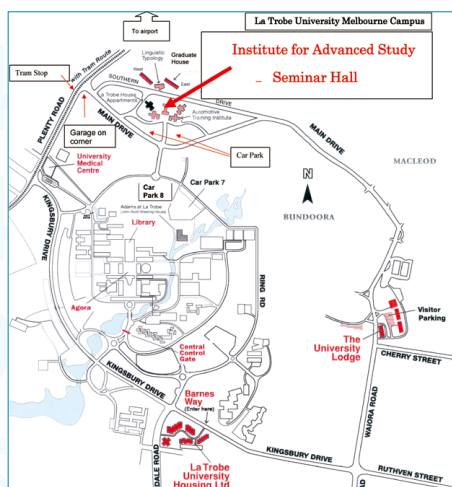
John Sader, The University of Melbourne

Aleksandar Staykov, I²CNER, Kyushu University

Daisuke Tagami, IMI, Kyushu University

Graeme Wake, Massey University

Annette Worthy, University of Wollongong



Venue:

**Institute for Advanced Study – Seminar Hall
La Trobe University, Melbourne, Australia**

Organizing Committee:

Philip Broadbridge

(La Trobe University)

Pierluigi Cesana

(IMI Australia Branch, Kyushu University / La Trobe University)

Dimetre Triadis

(IMI Australia Branch, Kyushu University / La Trobe University)

Trina Dreher

(Suez Oil & Gas Systems)

Kenji Kajiwar

(IMI, Kyushu University)

Registration: https://latrobe.onestopsecure.com/onestopweb/LTUEv/createbooking?e=SHE_EV32



Contact: Institute of Mathematics for Industry, Kyushu University
mail: kyoten-jimu@imi.kyushu-u.ac.jp

	Monday 15th February	Tuesday 16th February	Wednesday 17th February		
9:00 am	Conference Registration	Bob Anderssen Food rheology: wheat grain hardness and wheat flour dough	Shaun Hendy Modelling micro and nanostructured surfaces	9:00 am	
9:15 am				9:15 am	
9:30 am	Welcome to Conference			9:30 am	
9:45 am	Graeme Wake Fires in stored materials - assessment of risk	Trina Dreher Electrostatic desalter optimisation	Keisuke Matsuya Spatial pattern of discrete and ultradiscrete Gray-Scott model	9:45 am	
10:00 am				10:00 am	
10:15 am		Veronique Bonnelye Water - new challenges		10:15 am	
10:30 am	Morning Tea		Morning Tea	10:30 am	
10:45 am		Morning Tea		10:45 am	
11:00 am	Annette Worthy Various studies to generate and control solitons in nematic liquid crystals	Mark Nelson The biological treatment of wastewater	Daisuke Tagami Finite element analysis of viscoelastic flow problems with application incorporating the Oldroyd-B model	11:00 am	
11:15 am				11:15 am	
11:30 am				11:30 am	
11:45 am	Tony Guttman Polymers pulled from, and pushed towards, a wall	Bronwyn Hajek Electrokinetic behaviour of concentrated colloidal suspensions	Philip Broadbridge Continuum modelling of grain boundary evolution on metal surfaces	11:45 am	
12:00 pm				12:00 pm	
12:15 pm				12:15 pm	
12:30 pm	Lunch		Lunch	12:30 pm	
12:45 pm		Boxed lunch		12:45 pm	
1:00 pm		Excursion - Bus leaves La Trobe for Healsville Sanctuary			1:00 pm
1:15 pm					1:15 pm
1:30 pm			1:30 pm		
1:45 pm	John Sader Viscoelastic flows generated by vibrating nanoscale structures in simple liquids		1:45 pm		
2:00 pm		2:00 pm			
2:15 pm	David Boger From Boger fluids to environmental rheology	Aleksandar Staykov Application of the non-equilibrium Green's function method in the design of nanoelectronic devices		2:15 pm	
2:30 pm			2:30 pm		
2:45 pm	Yasuhide Fukumoto Topological idea combined with asymptotic expansions for vortex motion			2:45 pm	
3:00 pm		Conference Closing Remarks	3:00 pm		
3:15 pm	Afternoon Tea	Excursion - Bus leaves Sanctuary		3:15 pm	
3:30 pm				3:30 pm	
3:45 pm	Student Poster Presentations			3:45 pm	
4:00 pm				4:00 pm	
4:15 pm				4:15 pm	
4:30 pm				4:30 pm	
4:45 pm				4:45 pm	
5:00 pm				5:00 pm	

IMI-La Trobe Joint Conference

Mathematics for Materials Science and Processing

Institute for Advanced Study – Seminar Hall
La Trobe University, Melbourne, Australia, February 15 -17, 2016

Table of Contents

Fires in stored materials – assessment of risk	1
Graeme Wake (Massey University)	
Various studies to generate and control solitons in nematic liquid crystals	4
Annette L. Worthy (University of Wollongong)	
Polymers pulled from, and pushed towards, a wall	9
Tony Guttman (The University of Melbourne / ARC Centre of Excellence for Mathematics and Statistics of Complex Systems, MASCOs)	
Topological idea combined with asymptotic expansions for vortex motion	12
Yasuhide Fukumoto (Kyushu University)	
Food rheology: wheat grain hardness and wheat flour dough	18
Bob Anderssen and Reka Haraszi (CSIRO Australia)	
Electrostatic Desalter Optimisation	24
Trina Dreher (Suez Oil & Gas Systems)	
Water - New challenges	30
Veronique Bonnelye (Suez Water & Treatment Solutions)	
The biological treatment of wastewater	34
Mark Nelson (University of Wollongong)	
Electrokinetic behaviour of concentrated colloidal suspensions	40
Bronwyn Hajek (University of South Australia)	
Modelling micro and nanostructured surfaces	45
Shaun Hendy (University of Auckland)	
Spatial pattern of discrete and ultradiscrete Gray-Scott model	48
Keisuke Matsuya (Musashino University)	

Finite element analysis of viscoelastic flow problems, with application incorporating the Oldroyd-B model	54
Daisuke Tagami (Kyushu University)	
Continuum modelling of grain boundary evolution on metal surfaces	56
Philip Broadbridge (Kyushu University / La Trobe University)	
Viscoelastic Flows Generated by Vibrating Nanoscale Structures in Simple Liquids	61
John E. Sader (The University of Melbourne)	
Application of the non-equilibrium Green's function method in the design of nanoelectronic devices	64
Aleksandar Staykov (Kyushu University)	

Fires in stored materials — assessment of risk

Graeme Wake

Centre for Mathematics-in-Industry,
Massey University, Auckland, New Zealand

The classical theory of thermal condition has been developed using the stationary theory for a nonlinear heat conduction equation. The ignition threshold is then obtained as a bifurcation point in parameter space. This is well-suited for obtaining the critical storage conditions in steady ambient conditions, or its critical thermal properties above/below which it will/will-not catch fire. This theory was applied successfully in a substantial legal investigation of a fire on the container vessel Aconcagua (Figure 1) which severely damaged the vessel. The fire occurred on 30th December 1998, in the Pacific Ocean resulting in extensive damage to vessel and cargo on board. The source of the explosion was immediately identified to be a container loaded with 334 kegs (plastic drums, known as quadritainers) of calcium hypochlorite shipped by a major shipper. Ten years later the English courts found the shipper liable to the carrier under the bill of lading contract for shipping dangerous goods in breach of the Hague Rules, with an initial judgment amount in the sum of USD 27.75 million, and further extensive quantum issues still to be resolved. The evidence provided was based on the theory described here.



FIGURE 1. Fire on the container vessel Aconcagua

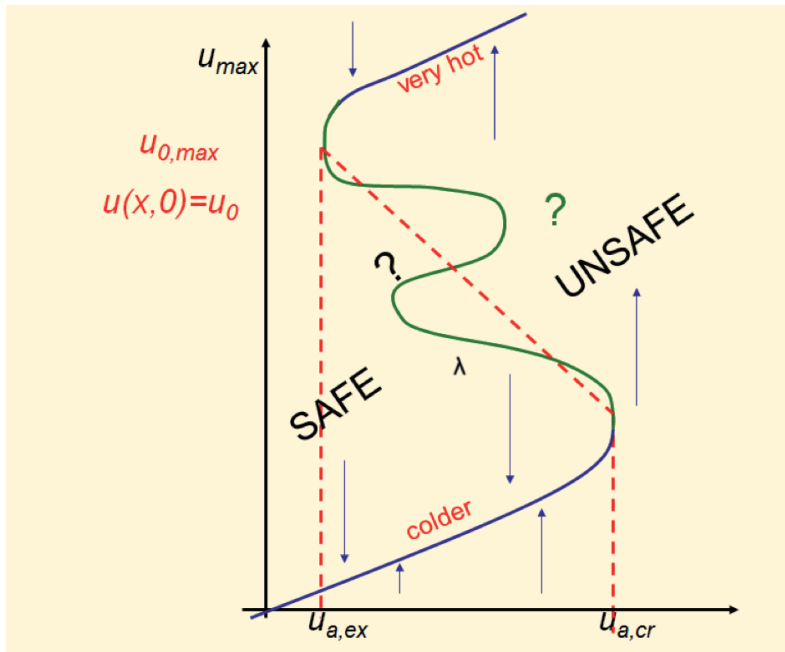


FIGURE 2. Schematic bifurcation diagram for steady-state nonlinear heat conduction

This stationary theory is captured in the steady-states of the nonlinear heat conduction equation

$$\Delta u + \lambda \exp(-1/u) = \frac{\partial u}{\partial t} \quad \text{in the region } \Omega, t > 0;$$

with a (say Dirichlet) boundary condition $u = u_a$ on the spatial boundary $\partial\Omega$. Here u is a measure of the dimensionless temperature, and λ is a measure of the exothermicity of the material. Here we have neglected the effect of reactant consumption and mass transfer, which is a reasonable assumption for many ignition events.

A schematic representation of the resulting bifurcation diagram, using u_a (a measure of the ambient stored temperature) as the distinguished parameter and λ as a co-parameter is shown in Figure 2.

The number of intermediate solutions is dependent on the geometry and λ . It is known that, in general, only the smallest and highest solutions are asymptotically stable and therefore attracting with time t . Some actual computed bifurcation diagrams are shown in Figure 3. Here U is the ambient temperature, $n = 0, 1, 2$ are the infinite slab (one-dimension), infinite circular cylinder, and unit sphere respectively. The highest stable solution is not shown as it is much larger. Of those that are shown, only the smallest is stable.

Recently a raft of consulting problems have arisen where the ignition is triggered by “super-critical” initial conditions — that is, the material stored in safe ambient conditions, but is assembled too hot. This suggests the existence of a nonlinear manifold $\{u(x,0)\}$ of critical initial conditions. Similarly, situations are now arising in applications where the variations in the ambient temperature can trigger a thermal

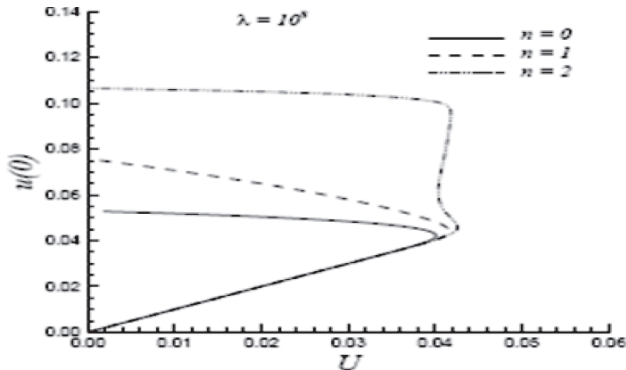


FIGURE 3. Path-following outputs; Stationary solutions

spontaneous ignition, while the average suggests that the material is sub-critical. Thus new algorithms are needed to determine critical thresholds for both these transient scenarios to provide under-pinning decision support for legal assessments.

Numerical procedures have been developed for this purpose for defining the thresholds for thermal ignition for both of these scenarios. These are used commercially to assist assessment of new ignition scenarios. The shape of the initial temperature profile is also investigated, using the moments of the profile. Recently a coal mine disaster in New Zealand, where a “flashover event” was deemed to be part of the tragedy which cost 29 miners their lives, gave rise to a mathematical investigation involving non-local calculus, where cause and event are spatially separated. This situation will be illustrated on a video clip.

REFERENCES

- [1] Boddington T., P. Gray, and G. C. Wake, “Criteria for thermal explosions with and without reactant consumption”, Proc. Royal. Soc. Lond. Series A 357, 1977, pp. 403–422.
- [2] Gong R., J. G. Burnell and G. C. Wake, “Modelling spontaneous combustion in wet lignite”, Combustion Theory Modelling 3, 1999, pp. 215–232.

Various studies to generate and control solitons in nematic liquid crystals

Annette L. Worthy

School of Mathematics and Applied Statistics, University of Wollongong, Northfields Avenue, Wollongong, New South Wales, 2522, Australia

(joint work with Antonmaria A. Minzonia^a, Luke W. Sciberras^b Noel F. Smyth^c)

a Fenomenos Nonlineales y Mecanica (FENOMECA), Department of Mathematics and Mechanics, Instituto de Investigacion en Matematicas Aplicadas y Sistemas, Universidad Nacional Autónoma de México, 01000 México D.F., Mexico

b School of Mathematics and Applied Statistics, University of Wollongong, Northfields Avenue, Wollongong, New South Wales, 2522, Australia

c School of Mathematics and Maxwell Institute for Mathematical Sciences, University of Edinburgh, Edinburgh EH9 3FD, Scotland, UK

1. SOLITARY WAVES

Zabusky and Kruskal [25] coined the term soliton to describe this particle-like behaviour of the solitary waves. A mathematical definition of a soliton was developed using two prominent features of the propagation of nonlinear waves. These features being that a soliton has a profile which is asymptotically constant at infinity; and solitons interact without changing their form or identity. The only effect of solitons colliding may be a phase change.

In the 1960's, theoretical developments sparked interest in finding physical applications of solitary waves in mediums which included nonlinear optical media. The first exploration of solitary waves in nonlinear optics began with Franken [7] who undertook experiments into optical second harmonics. It was later found that solitary waves or optical beams existed in two forms. These being temporal and spatial solitary waves. Each form are defined by a different nonlinear effect(s). These being:

- **Temporal solitary waves.** These waves occur in a medium which is dispersive, such as, silica glass fibres [10], with a temporal broadening of the beam. The mechanism that drives dispersion is a phase velocity difference between the frequency components of the beam. As the pulse evolves the beam frequency broadens since different components have different phase velocities, resulting in the frequencies moving at varying speeds. Finally, the beam disperses.
- **Spatial solitary wave.** These waves are signified by the broadening of the beam due to diffraction. The differences in the spatial phase velocity of each of the components causes the beam to diffract.

Both temporal and spatial solitary waves or beams can only occur if there is a counterbalance to the beams dispersion/diffraction by the propagation medium. Here the broadening of the wave or beam (in both cases) is balanced by the localised change in the refractive index of the medium. That is, the nonlinearity of the medium modifies the refractive index. This leads to light induced lensing [21] or self focusing [3] so that the combination of self-focusing and beam broadening allows the propagation (or

evolution) of temporal and spatial solitary waves in nonlinear media. Nonlinear self-focusing is, therefore, a change in the refractive index of a medium by the beam. When this occurs the beam has formed its own waveguide and is said to be self-trapped [21].

In our discussion, spatial solitary waves will be considered based upon the following observations:

- the large nonlinearities associated with the media that supports spatial solitary waves which produce different physical effects;
- the equations that govern the evolution of spatial solitary waves are highly dependent on the properties of the propagation medium.
- keen interest has been aroused through the proposed use of spatial solitary waves or laser light in technology, especially in electronic switches and gates.

2. LIQUID CRYSTAL: MEDIUM OF PROPAGATION

Although there are numerous optical media that allow the formation of solitary waves, such as lead glass [19], [20], thermal liquids [6], ion gases [23], photo refractive crystals [22], [13] and Bose-Einstein condensates [15], [9], none of these media possess the same nonlinear refractive index as liquid crystals. A liquid crystal medium has a response that extends way beyond the local change in the refractive index to include the surrounding area of the media. The term used in this respect is ‘nonlocal effect’.

Recently, liquid crystals have received intense acknowledgement due to their unique physical and optical properties. Physically, the liquid crystal molecules can flow like a liquid, but also maintains some degree of crystalline structure. Apart from this, liquid crystals can integrate seamlessly with current opto-electronic devices (due to their chemical stability), allowing for an easy transition to its use in all-optical communications. The remarkable benefit that liquid crystals have over other optical media is its large nonlinearity. This nonlinearity extends to in all of its physical states.

Further, liquid crystals are a thermotropic medium, which means that the three phases of a liquid crystal are temperature dependent. These three distinct phases vary from a highly ordered molecular state (cold temperature) to a highly disordered molecular state (hot temperature). The anisotropic, or smectic phase, is a highly structured phase for which the molecules maintain positional and directional ordering in layers, similar to crystal lattices. The next phase is the nematic phase, for which the medium develops the fluidity of a liquid and loses positional ordering within the crystal. However, directional ordering is maintained in the form of a preferred average direction. The final phase is the isotropic phase, for which all order within the crystal is lost [11], [12].

3. NEMATIC LIQUID CRYSTAL (NLC)

Based on the above explanations spatial solitary waves in nonlinear soft media are deemed to have a nonlocal response. In particular, soft matter like nematic liquid crystals, has nonlinear response which is deemed to be nonlocal. As a consequence, nematic liquid crystals, will be a subject of discussion in the talk given.

It is noted that a nematic liquid crystal (NLC) or the nematic phase of the liquid crystal has molecules that are rod-like structures [11], [12], [17] with no positional order, but a tendency to naturally align due to intermolecular forces, with the long axes of the molecules being close to parallel and in a common direction. These molecules are able to move and are randomly positioned as if in a liquid. However, a long-ranged

directional ordering is preserved in space. This, orientational average molecule ordering and having a degree of angular/rotational ordering make NLC an attractive and flexible propagation medium to be used in optical technologies.

4. NEMATICON: A SOLITARY WAVE IN NLC

It is noted that if an optical beam enters an optically dense medium, such as an NLC, the beam itself linearly diffracts. This beam can induce a local change in the refractive index of the medium, which results in a self-focusing of the optical beam to a point. Due to these properties in the medium, the formation of a solitary wave exists. Hence, when a coherent optical beam enters the NLC medium there is a balance between two optical effects, that is, linear diffraction and self-focusing. Imposing the nonlinear compensation of diffraction results in a self-trapped beam solitary wave termed a ‘nematicon’ [2]. The stability of a nematicon is due to the nonlocality of the NLC which can be demonstrated by looking at a local medium such as a Kerr medium. Nonlinear beam propagation in local Kerr media is governed by the nonlinear Schrödinger (NLS) equation

$$i\frac{\partial u}{\partial z} + \frac{1}{2}\nabla^2 u + |u|^2 u = 0.$$

In one space dimension we have that

$$\nabla^2 u = u_{xx}$$

and hence the NLS equation is exactly integrable [5] where the solitary wave solutions are stable. However, in two space dimensions,

$$\nabla^2 u = u_{xx} + u_{yy}$$

solitary wave solutions of the NLS equation show catastrophic collapse. That is, they develop into waves with infinite amplitude and zero width in finite z .

In contrast to the above Kerr affect, as a consequence of the elastic forces where the NLC’s response is nonlocal, its affect extends beyond the optical beam. Thus, the refractive index perturbation is wider than the actual beam itself. That is, the NLC has an affects on the nematic molecules outside of the optical beam [1]. The result is that there is stabilisation of the nematicon [17]. Further, an increase in the power of the beam prevents the usual collapse associated with solitary waves in $2D$ local media therefore sustaining the nematicon.

5. FREÉDERICKSZ THRESHOLD

The self-focusing of an optical beam in NLC is enabled provided a minimum power requirement is met. This is known as the Freédericksz threshold, Eth [17], [14]. If an optical beams power is below the Freédericksz threshold then no NLC molecular rotation will occur.

At the beginning, when NLC was first being considered as a propagation medium [4], difficulties in obtaining a self-focusing response were encountered. It was discovered that the use of large optical beam powers $O(1)W$ induced a change in the refractive index, but at the same time introduced thermal effects due to localised heating of the NLC. Cumbersome, external cooling of the NLC was then attempted to counteract the localised heating. A dye introduced into the NLC, reduced the power level of the optical beam that was needed to obtain self-focusing. It was observed that there

was an increase in the nonlinear response [24]. However, thermal effects were still present which altered the properties of the nematic. An idea emerged to use the pre-existing properties of the NLC to an advantage, which allowed for smaller optical beam powers to be used $O(1)\text{mW}$. This meant, at last, the removal of the thermal effects. Noting that self-focusing of the optical beam requires the nematic molecules to be rotated, a low-frequency static external electric field across the NLC meant that nematic molecules could pre-tilt [2]. This electric field is perpendicular to the direction of the optical beam propagation. Consequently, the balance required to self-trap/form a nematicon is struck at low optical powers. It was found that the Freédricksz threshold is reduced to zero [16] when the NLC molecular pre-tilt angle is $\pi/4$ with the beam direction of propagation.

6. VARIOUS STUDIES TO GENERATE AND CONTROL SOLITONS IN NEMATIC LIQUID CRYSTALS

The following discussions, work and talk are based on collaborations with Professors Smyth (Edinburgh University, Scotland), Minzoni (UNAM, Mexico) and Assanto (Roma 3, Italy) with contributions by Dr Sciberras (Wollongong University).

Great interest exists in using soliton solutions in non-linear optics. Importantly, the utilisation of spatial solitons (nematicons) in nematics liquid crystals is currently being studied as the backbone of photonic devices to produce all optical switching devices to improve, for instance, the speed of data transmission.

Based on a system of two non-linear partial differential equations where one is the NLS for the optical beam and the other for the nematic response, a mathematical treatise of experimental work on the generation and control of optical solitons in the nonlinear nonlocal nematic media will be discussed.

Using asymptotic methods along with the nematicon being is largely independent of functional form of its profile, it is shown how the optical beam evolves. It will be revealed that a nematicon sheds radiation whereby the velocity and position decoupled from its width and amplitude oscillations. It will be shown that having an additional localized voltage to form various suitable regimes causes the director or nematic to have different orientations with the cell. Some geometries that will be studied are the rectangular cross section, circular and elliptical regions. Further, due to the additional geometries caused by an external applied voltage to the nematic upon twisting the molecules, the resulting polarized self propagating beams distorts and refracts. The resulting mathematical analysis is quick and efficient and is shown to give excellent agreement to both experimental work and numerical simulations.

Also, the collision of two or more nematicons with relevance to the elasticity of the NLC will be discussed. This is modelled by considering a system of two non-linear partial differential equations with the assumption that the nematicons have a sech profile and cross-sectionally circular shape in an averaged Lagrangian are considered. Comparisons are made by with numerical methods. When the nematicons have an initial separation and angular momentum, it is found that the nematicons form a bounded state, called a nematic on dipole [8]. Due to different diffractions and coupling coefficients, the resulting bounded state exhibits walk-off. There is some disagreement between the analytic and the numerical solutions due to the change in nematic cross-section shape from circular to elliptical. Further, calculation of momentum loss due to shed radiation is less than the numerical.

REFERENCES

- [1] Alberucci, A., Assanto, G., Buccoliero, D., Desyatnikov, A. Marchant, T. and Smyth, N., Modulation analysis of boundary induced motion of optical solitary waves in a nematic liquid crystal. *Phys. Rev. A.*, vol. 79, p. 043816, 2009
- [2] Assanto, G., Peccianti, M. and Conti, C., Nematicons: Optical spatial solitons in nematic liquid crystals. *Optics & Photonics News*, vol. 14, pp. 4448, 2003
- [3] Beeckman, J., Neyts, K., Hutsebaut, X., Cambournac, C. and Haelterman, M., Time dependence of soliton formation in planar cells of nematic liquid crystals. *IEEE J. Quantum Electron.*, vol. 41, pp. 735740, 2005
- [4] Braun, E., Faucheux, L. and Libchaber, A., Strong self-focusing in nematic liquid crystals. *Phys. Rev. A.*, vol. 48, pp. 611622, 1993
- [5] Cao, L., Zhu, Y., Lu, D., Hu, W., and Guo, Q., 'Propagation of nonlocal optical solitons in lossy media with exponential-decay response.' *Optics Communications*, 281:50045008, 2008
- [6] Dreischuh, A., Neshev, D., Peterson, D., Bang, O. and Krolikowski, W., Observation of attraction between dark solitons. *Phys. Rev. Lett.*, vol. 96, p. 043901, 2006
- [7] Franken, P., Hill, A., Peters, C. and Weinreich, G., Generation of optical harmonics. *Phys. Rev. Lett.*, vol. 7, pp. 118119, 1961
- [8] Garcia Reimbert, C., Minzoni, A.A., Skuse, B.D., Smyth, N.F., Marchant, T.R. and Worthy, A.L., Mathematical Modelling of Nematicons and their Interactions. 2008 *IEEE/LEOS*, pp 119-120
- [9] Griesmaier, A., Werner, J., Hensler, S., Stuhler, J. and Pfau, T., Bose-einstein condensation of chromium. *Phys. Rev. Lett.*, vol. 94, p. 160401, 2005
- [10] Mollenauer, L., Stolen, R. and Gordon, J., Experimental observation of picosecond pulse narrowing and solitons in optical fibers. *Phys. Rev. Lett.*, vol. 45, pp. 10951098, 1980
- [11] Khoo, I., *Liquid Crystals: Physical Properties and Nonlinear Optical Phenomena*. Wiley, 2nd ed., 1995
- [12] Khoo, I., Nonlinear optics of liquid crystalline materials. *Phys. Rep.*, vol. 471, pp. 221267, 2009
- [13] Krolikowski, W., Saffman, M., Luther-Davies, B. and Denz, C., Anomalous interaction of spatial solitons in photorefractive media. *Phys. Rev. Lett.*, vol. 80, pp. 32403243, 1998
- [14] McLaughlin, D., Muraki, D. and Shelley, M., Self-focussed optical structures in a nematic liquid crystal. *Physica D*, vol. 97, no. 4, pp. 471497, 1996
- [15] Parola, A., Salasnich, L. and Reatto, L., Structure and stability of bosonic clouds: Alkali-metal atoms with negative scattering length. *Phys. Rev. A.*, vol. 57, pp. R3180R3183, 1998
- [16] Peccianti, M., Brzdakiewicz, K. and Assanto, G., Nonlocal spatial soliton interactions in nematic liquid crystals. *Opt. Lett.*, vol. 27, pp. 14601462, 2002
- [17] Peccianti, M. and Assanto, G., Nematicons. *Phys. Reports*, vol. 516, pp. 147208, 2012
- [18] Rotschild, C., Alfassi, B., Cohen, O. and Segev, M., Long-range interactions between optical solitons. *Nat. Phys.*, vol. 2, pp. 769774, 2006
- [19] Rotschild, C., Cohen, O., Manela, O., Segev, M. and Carmon, T., Solitons in nonlinear media with an infinite range of nonlocality: first observation of coherent elliptic solitons and of vortex-ring solitons. *Phys. Rev. Lett.*, vol. 95, p. 213904, 2005
- [20] Rotschild, C., Alfassi, B., Cohen, O. and Segev, M., Long-range interactions between optical solitons. *Nat. Phys.*, vol. 2, pp. 769774, 2006
- [21] Segev, M. Optical spatial solitons. *Opt. & Quantum Electron.*, vol. 30, pp. 503533, 1998
- [22] Segev, M., Crosignani, B., Yariv, A. and Fisher, B., Spatial solitons in photorefractive media. *Phys. Rev. Lett.*, vol. 68, pp. 923926, 1992
- [23] Suter, D. and Blasberg, T., Stabilization of transverse solitary waves by a nonlocal response of the nonlinear medium. *Phys. Rev. A.*, vol. 48, pp. 45834587, 1993
- [24] Warenghem, M., Henninot, J. and Abbate, G., Nonlinearly induced self wave guiding structure in dye doped nematic liquid crystals confined in capillaries. *Opt. Express*, vol. 2, pp. 483490, 1998
- [25] Zabusky, N. and Kruskal, M., Interaction of solitons in collisionless plasma and the recurrence of initial states. *Phys. Rev. Lett.*, vol. 15, pp. 240243, 1965

Polymers pulled from, and pushed towards, a wall

Tony Guttman

School of Mathematics and Statistics, The University of Melbourne, Australia.
ARC Centre of Excellence for Mathematics and Statistics of Complex Systems,
MASCOS

In recent years there have been important experiments involving the pulling of polymers from a wall. These are carried out with atomic force microscopes and other devices to determine properties of polymers, including biological polymers such as DNA. A version of the experimental set-up is shown in Figure 1 (left).

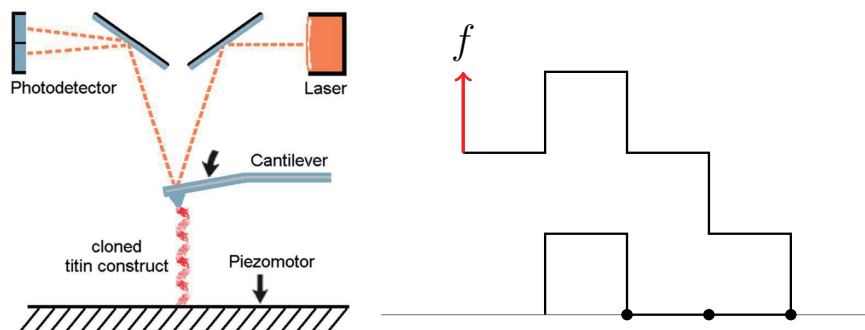


Figure 1. Experimental setup (left), and self-avoiding walk model (right).

We have studied a simple model of this system, as modelled by two-dimensional self-avoiding walks (SAWs), anchored to a wall at one end and then pulled from the wall at the other end. In addition, we allow for binding of monomers in contact with the wall. The geometry is shown in Figure 1 (right). Thus there are two parameters in the model, the strength of the interaction of monomers with the surface (wall), and the force, normal to the wall, pulling the polymer.

We have constructed (numerically) the complete phase diagram, and can prove the locus of certain phase boundaries in that phase diagram, and also the order of certain phase transitions as the phase boundaries are crossed. A schematic of the phase diagram is shown in Figure 2.

Most earlier work focussed on simpler models of random, directed and partially directed walk models. There has been little numerical work on the more realistic SAW model. A recent rigorous treatment by van Rensburg and Whittington established the existence of a phase boundary between an adsorbed phase and a ballistic phase when the force is applied normal to the surface. We give the first proof that this phase transition is first-order. As well as finding the phase boundary very precisely, we also estimate various critical points and exponents to high precision, or, in some cases exactly (conjecturally).

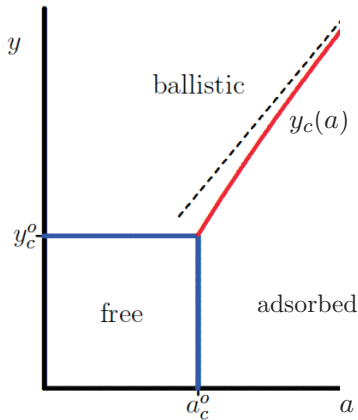


Figure 2. Phase diagram for a polymer pulled from a wall. Here $y = \exp[f/k_B T]$ is related to the applied force f , and $a = \exp[-\epsilon/k_B T]$ is related to a surface interaction energy ϵ , where k_B is Boltzmann's constant and T is the absolute temperature.

We use exact enumeration and series analysis techniques to identify this phase boundary for SAWs on the square lattice.

Our results are derived from a combination of three ingredients:

- (i) Rigorous results.
- (ii) Faster algorithms giving extended series data.
- (iii) New numerical techniques to extract information from the data.

A second calculation considers polymers squeezed towards a surface by a second wall parallel to the surface wall. In this problem we ignore the interaction between surface monomers and the wall.

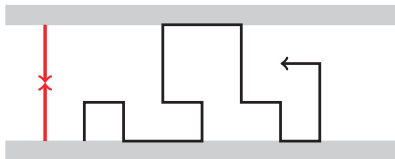


Figure 3. Self-avoiding walk model for polymer squeezed between two walls.

Consider a walk ω in the upper half-plane, starting at the origin and reaching maximum height $h(\omega)$. Give it a *Boltzmann weight* $e^{-f \cdot h(\omega)}$. For example, the walk above receives weight e^{-3f} .

The *partition function* of walks of length n is

$$Z_n(f) = \sum_{|\omega|=n} e^{-f \cdot h(\omega)}$$

and the *free energy* is

$$\lambda(f) = \lim_{n \rightarrow \infty} \frac{1}{n} \log Z_n(f)$$

which can be shown to exist for all f .

The case $f > 0$ represents a force pushing down towards the surface, while $f < 0$ represents a force pulling away from the surface. When f is large and positive, walks

with small $h(\omega)$ dominate the partition function. When f is large and negative, walks with large $h(\omega)$ dominate.

The free energy $\lambda(f)$ is a continuous, convex function of f , and is almost-everywhere differentiable. Nick Beaton [NRB15] has proved that $\lambda(f)$ has a point of non-analyticity at $f = 0$: it is strictly decreasing for $f < 0$, but $\lambda(f) = \log \mu$ for $f \geq 0$:

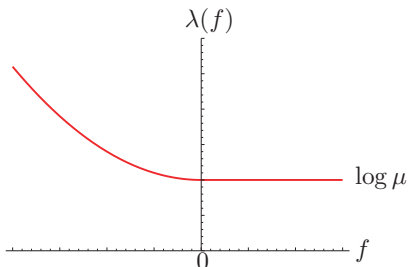


Figure 4. Variation of $\lambda(f)$ with applied force f .

This indicates a *phase transition* at $f = 0$.

We find, remarkably, that in this geometry there arises an unexpected stretched exponential term in the asymptotic expression for the number of configurations. We show explicitly that this can occur even if one uses random walks as the polymer model, rather than the more realistic self-avoiding walks.

This situation has not been studied experimentally, as far as we are aware, but it would be interesting to do so.

Aspects of this work have been carried out with Nick Beaton, Iwan Jensen, Greg Lawler and Stu Whittington.

REFERENCES

- [1] Anthony J. Guttmann, Iwan Jensen, Stu G. Whittington, Pulling adsorbed self-avoiding walks from a surface, arXiv:1309.7401.
- [2] Nicholas R. Beaton, Anthony J. Guttmann, Iwan Jensen, Gregory F. Lawler, Compressed self-avoiding walks, bridges and polygons, arXiv:1506.00296.

Topological idea combined with asymptotic expansions for vortex motion

Yasuhide FUKUMOTO

Institute of Mathematics for Industry, Kyushu University, Japan

1. INTRODUCTION

Vortex rings are ubiquitous coherent structures in high-Reynolds-number flows, and are of fundamental importance in fluid mechanics. Vortex rings are used for producing thrust and lift by insects, fishes and animals. Vortex rings are capable of transporting neutrally buoyant materials. Recently they find their utility for creating virtual reality in the field of entertainment. There is an attempt to use an air cannon, as a means of olfactory display, to deliver smells encapsulated in a vortex ring to a targeted person. In a theater, virtual reality contents are created solely by image and sound. Reality is enhanced if we appeal to tactile display. A mini-theater is planned in which air cannons are designed to produce vortex rings, in synchronization with the image and the sound, so that the audience experiences direct impact and freshness. These applications to entertainment necessitate controlled vortex rings, and raise questions pertaining to an inverse problem. When does a vortex ring arrive at a specified point? How far does the ring travel? How large the vortex ring has grown at the moment of impact? This talk addresses these questions.

In 1858, the field of vortex dynamics started with a single piece of paper written by Helmholtz. In his seminal paper [1], Helmholtz proved a distinguishing feature of the vorticity that vortex lines are frozen into the fluid. In the same paper, he studied motion of vortex rings. By an elaboration from the Euler equations, now being widely known through Lamb's textbook [2], Helmholtz had reached an identity for traveling speed of a thin axisymmetric vortex ring, steadily translating in an inviscid incompressible fluid of infinite extent. Helmholtz-Lamb's method is recapitulated in a recent article [3].

By a deep insight into the formation of a columnar vortex along the central line of a rotating tank filled with water, Kelvin [4] envisioned that a columnar vortex should be a state of the maximum of the kinetic energy, with respect to perturbations that maintain the circulation. An almost century passed before Kelvin's variational principle was mathematically formulated and proved. Arnol'd [5] proved that a steady solution of the Euler equations of an incompressible fluid is an extremal of the total kinetic energy with respect to the kinematically accessible perturbations. We mean by *kinematically accessible perturbations* the perturbation flow field for which the perturbed vorticity is frozen into the perturbed flow field. The kinematically accessible perturbations may be alternatively said to be the *isovortical perturbations* or occasionally the *rearrangements*. Mathematical proof for steady isolated vortex as the maximum-energy states uses rearrangement inequalities (see, for example, [6]).

Kelvin's variational principle can be extended to make allowance for motion by adding a constraint of constant impulse [7, 8, 9]; a stationary configuration of vorticity in an inviscid incompressible fluid, in a steadily moving frame, is realizable as an extremal of energy on an isovortical sheet under the constraint of constant impulse.

Our main concern lies in the variational principle for motion of vortex rings. Kelvin-Benjamin's variational principle is adapted to find the traveling speed of steady vortices [9, 10]. This variational principle is applied to motion of vortex rings.

Finite-thickness effect of vortex tubes is a common problem in the dynamics of interacting vortices in two dimensions, and has been intensively studied so far. Compared with the axisymmetric problem, less is known about interaction of (anti-) parallel vortex tubes. For motion of a curved vortex tube, the correction of curvature origin appears at first order in a small parameter, the ratio of the core- to the curvature radii, but, for a planar problem, the finite-size effect of the core makes its appearance at a high order in the ratio of the core radius to the vortex distance. The last section is concerned with motion of a counter-rotating vortex pair [18].

2. KELVIN-BENJAMIN'S VARIATIONAL PRINCIPLE

We assume that the fluid is incompressible, and take the density of fluid to be $\rho_f = 1$. In addition, we assume that the vorticity $\boldsymbol{\omega} = \nabla \times \mathbf{u}$ is localized in some finite region in such a way that the velocity decreases sufficiently rapidly. Define the total kinetic energy H and the hydrodynamic impulse \mathbf{P} , of the fluid filling an unbounded space, by

$$(1) \quad H = \frac{1}{2} \iiint \mathbf{u}^2 dV, \quad \mathbf{P} = \frac{1}{2} \iiint \mathbf{x} \times \boldsymbol{\omega} dV.$$

We confine ourselves to steady motion, with constant speed \mathbf{U} , of a region with vorticity and assume that the flow is stationary in a frame moving with \mathbf{U} . It is expedient to partition the velocity \mathbf{u} as $\mathbf{u} = \bar{\mathbf{u}} + \mathbf{U}$. By the assumption that the relative velocity $\bar{\mathbf{u}}$ is steady, it obeys

$$(2) \quad \nabla \times (\bar{\mathbf{u}} \times \boldsymbol{\omega}) = \mathbf{0}.$$

Suppose that fluid particles undergo an infinitesimal displacement $\delta \boldsymbol{\xi}$ while preserving the volume of an arbitrary fluid element:

$$(3) \quad \mathbf{x} \rightarrow \tilde{\mathbf{x}} = \mathbf{x} + \delta \boldsymbol{\xi}(\mathbf{x}); \quad \nabla \cdot \delta \boldsymbol{\xi} = 0.$$

We impose the condition that the flux of vorticity through an arbitrary material surface be unchanged throughout the process of the displacement. Its local representation is [8]

$$(4) \quad \delta \boldsymbol{\omega} = \nabla \times (\delta \boldsymbol{\xi} \times \boldsymbol{\omega}).$$

The translation velocity \mathbf{U} of a vortex ring is then calculable through the variation

$$(5) \quad \delta H - \mathbf{U} \cdot \delta \mathbf{P} = 0,$$

under the constraint that, for any smooth Lagrangian displacement of fluid particles, the vorticity is frozen into the fluid. Section 2 touches upon this principle, which is the theme of ref. [9]. Intriguingly, the same principle encompasses motion of a vortex ring ruled by the cubic nonlinear Schrödinger equation, which serves as a model for superfluid liquid helium and a Bose-Einstein condensate, at zero temperature [11].

In the sequel, we restrict this theorem to motion of a steadily moving axisymmetric vortex ring. An isovortical sheet is of infinite dimension. A family of solutions of the Euler equations includes a few parameters. By imposing certain relations among these parameters, we can maintain the solutions on a single isovortical sheet, and the restricted family of the solutions constitutes a finite dimensional set on the sheet.

3. HIGH-REYNOLDS-NUMBER VORTEX RING

The inner solution for steady motion of a vortex ring, or quasi-steady motion in the presence of viscosity, is found by solving the Euler or the Navier–Stokes equations, subject to the matching condition, in powers of the small parameter ε , the ratio of the core- to the ring-radii [15]. To work out the inner solution, we introduce the relative velocity $\tilde{\mathbf{u}}$ in the meridional plane by $\mathbf{u} = \tilde{\mathbf{u}} + (\dot{R}, \dot{Z})$. Here a dot stands for differentiation with respect to time. Let us non-dimensionalize the inner variables. We introduce, in the core cross-section, local polar coordinates (r, θ) around the core center. The radial coordinate is normalized by the core radius $\varepsilon R_0 (= \sigma)$ and the local velocity (u, v) , relative to the moving frame, by the maximum velocity $\Gamma/(\varepsilon R_0)$. The normalization parameter for the ring speed $(\dot{R}(t), \dot{Z}(t))$, the slow dynamics, should be Γ/R_0 . The suitable dimensionless inner variables are thus defined as

$$(6) \quad r^* = r/\varepsilon R_0, \quad t^* = t/\frac{R_0}{\Gamma}, \quad \psi^* = \frac{\psi}{\Gamma R_0}, \quad \zeta^* = \zeta/\frac{\Gamma}{R_0^2 \varepsilon^2}, \quad \tilde{\mathbf{u}}^* = \tilde{\mathbf{u}}/\frac{\Gamma}{R_0 \varepsilon}, \quad \dot{Z}^* = \dot{Z}/\frac{\Gamma}{R_0}.$$

The difference in normalization between the last two of (6) should be kept in mind. Correspondingly to (6), the kinetic energy H and the hydrodynamic impulse \mathbf{P} are normalized as $H^* = H/\Gamma^2 R_0$, $P_z^* = P_z/\Gamma R_0^2$. Hereinafter we drop the superscript $*$ for dimensionless variables. Dimensionless form of the radial position R of the core center is $R = 1 + \varepsilon^2 R^{(2)} + O(\varepsilon^3)$. We can maintain the first term to be unity by adjusting disposable parameters, bearing with the origin of coordinates, in the first-order field [15]. The second-order correction $\varepsilon^2 R^{(2)}$ is tied with the viscous expansion.

A glance at the Euler or the Navier–Stokes equations shows that the dependence, on θ , of the solution in a power series in ε is

$$(7) \quad \psi = \psi^{(0)}(r) + \varepsilon \psi_{11}^{(1)}(r) \cos \theta + \varepsilon^2 \left[\psi_0^{(2)}(r) + \psi_{21}^{(2)}(r) \cos 2\theta \right] + O(\varepsilon^3),$$

$$(8) \quad \zeta = \zeta^{(0)}(r) + \varepsilon \zeta_{11}^{(1)}(r) \cos \theta + \varepsilon^2 \left[\zeta_0^{(2)}(r) + \zeta_{21}^{(2)}(r) \cos 2\theta \right] + O(\varepsilon^3).$$

Upon substitution from (7) and (8), we obtain a representation, to $O(\varepsilon^2)$ in dimensionless form, $H = H^{(0)} + \varepsilon^2 H^{(2)}$ as

$$(9) \quad H^{(0)} = -2\pi^2 \int_0^\infty r \zeta^{(0)} \psi^{(0)} dr, \quad H^{(2)} = -2\pi^2 \int_0^\infty r \left(\frac{1}{2} \zeta_{11}^{(1)} \psi_{11}^{(1)} + \zeta^{(0)} \psi_0^{(2)} + \zeta_0^{(2)} \psi^{(0)} \right) dr.$$

The leading-order term $H^{(0)}$ of energy is evaluated with ease as

$$(10) \quad H_0/\Gamma^2 = \frac{1}{2} R_0 \left\{ \log \left(\frac{8R_0}{\sigma} \right) + A - 2 \right\},$$

where $H_0 = \Gamma^2 R_0 H^{(0)}$ and A is given by

$$(11) \quad A = \lim_{r \rightarrow \infty} \left\{ \frac{4\pi^2}{\Gamma^2} \int_0^r r' v_0(r')^2 dr' - \log \left(\frac{r}{\sigma} \right) \right\}.$$

The variation of (10) with respect to an isovortical perturbation is manipulated as

$$(12) \quad \delta H_0 = \frac{\Gamma^2}{2} \left[\log \left(\frac{8R_0}{\sigma} \right) + A - \frac{1}{2} \right] \delta R_0.$$

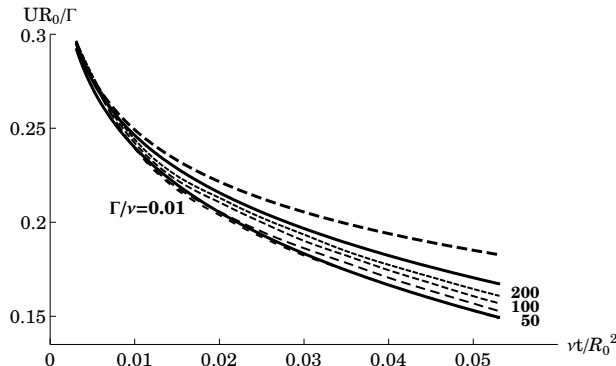


FIGURE 1. Variation of speed of a viscous vortex ring with time.

The variation of the leading term of impulse $P_0 = \Gamma\pi R_0^2$ is $\delta P_0 = 2\pi\Gamma R_0\delta R_0$, and application of (5) retrieves Fraenkel–Saffman’s formula [12, 14]:

$$(13) \quad U_0 = \frac{\Gamma}{4\pi R_0} \left\{ \log \left(\frac{8R_0}{\sigma} \right) + A - \frac{1}{2} \right\}.$$

The third-order correction U_2 to the translation speed of the vortex ring requires evaluation of $H^{(2)}$. For an inviscid vortex ring in steady motion, $R_2 = R_0\varepsilon^2 R^{(2)} \equiv 0$ without loss of generality, and, after some manipulations, we arrive at

$$(14) \quad U_2 = \frac{1}{R_0^3} \left\{ \frac{d_1}{2} \left[\log \left(\frac{8R_0}{\sigma} \right) - 2 \right] - \pi\Gamma B + \frac{\pi}{2\Gamma} \int_0^\infty r^4 \zeta_0 v_0 dr \right\},$$

where $v_0 = \Gamma v^{(0)}/\sigma$, $\zeta_0 = \Gamma \zeta^{(0)}/\sigma^2$ and d_1 is the dipole strength, and

$$(15) \quad B = \lim_{r \rightarrow \infty} \left\{ \frac{1}{\Gamma^2} \int_0^r r' v_0 \tilde{\psi}_{11}^{(1)} dr' + \frac{r^2}{16\pi^2} \left[\log \left(\frac{r}{\sigma} \right) + A \right] + \frac{d_1}{2\pi\Gamma} \log \left(\frac{r}{\sigma} \right) \right\}.$$

This is an extension, to $O(\varepsilon^3)$, of Fraenkel–Saffman’s formula (13).

Even if viscosity is switched on, the higher-order asymptotics U_2 is not invalidated at a large Reynolds number. Taking, as the initial condition, a circular line vortex of radius R_0 , the leading-order vorticity ζ_0 is given by

$$(16) \quad \zeta_0 = \frac{\Gamma}{4\pi\nu t} e^{-r^2/4\nu t},$$

where ν is the kinematic viscosity and t is the time measured from the instant at which the core is infinitely thin [12, 16], and the inhomogeneous heat-conduction equation governing $\zeta_0^{(2)}$ becomes tractable, with an introduction of similarity variables. we are eventually led to an extension of Saffman’s formula (13) in the form

$$(17) \quad U \approx \frac{\Gamma}{4\pi R_0} \left\{ \log \left(\frac{4R_0}{\sqrt{\nu t}} \right) - 0.55796576 - 3.6715912 \frac{\nu t}{R_0^2} \right\}.$$

Figure 1 displays the comparison of the asymptotic formula (17) with a direct numerical simulation of the axisymmetric Navier–Stokes equations [13]. The normalized speed UR_0/Γ of the ring is drawn as a function of normalized time $\nu t/R_0^2$ for its small values. The upper thick solid line is our formula (17), and the thick broken line is the

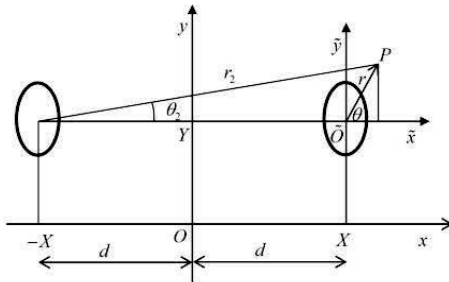


FIGURE 2. The Cartesian coordinates system (x, y) fixed in space and the polar coordinates system (r, θ) centered on (X, Y) in moving frame.

first-order truncation (13). The dashed lines are the results of the numerical simulations, attached with the circulation Reynolds number Γ/ν , ranging from 0.01 to 200. Augmented only with a single correction term, (14) appears to furnish a close upper bound on the translation speed. The lowermost solid line is the low-Reynolds-number limit obtained in a different manner [17]. Notably, the large-Reynolds-number asymptotic formula (17) compares fairly well with the numerical result of even moderate and small Reynolds numbers.

4. HIGH-REYNOLDS-NUMBER MOTION OF A VORTEX PAIR

The rest of this paper is concerned with motion of a counter-rotating vortex pair at very low Reynolds numbers [18].

4.1. Inner and outer expansions. Consider a counter-rotating vortex pair with circulations $\pm\Gamma$ moving in an inviscid fluid or a viscous fluid with the kinematic viscosity ν . The core radius σ of the two vortices is assumed to be much smaller than the distance $2d$ between the centroids of the two vortices. The outer solution is provided by the Biot–Savart law, though the distribution of vorticity remains to be calculated. The latter is found by the solution to the inner problem. The behavior of the Biot–Savart law valid near one of the vortex provides the matching condition on the inner solution.

4.2. Inner solution and traveling speed of a vortex pair. The inner solution is obtained by integrating the Navier–Stokes equation. We introduce the Cartesian coordinates (x, y) , fixed in space, with the x axis parallel to the direction of the line connecting the centroids. At the same time, we introduce local polar coordinates (r, θ) , centered at the centroid (X, Y) of one of the vortices, moving with it. The angle is measured from the direction parallel to the x -axis, and therefore the laboratory and the moving frames are viewed with each other through $x = X + r \cos \theta$ and $y = Y + r \sin \theta$ (figure 2). The radial coordinate r is non-dimensionalized by εd where $\varepsilon = \sigma/d = \sqrt{\nu/\Gamma}$ is a small parameter. The solution for the streamfunction ψ is sought in a power series in ε as

$$(18) \quad \psi = \psi^{(0)} + \varepsilon \psi^{(1)} + \varepsilon^2 \psi^{(2)} + \varepsilon^3 \psi^{(3)} + \varepsilon^4 \psi^{(4)} + \varepsilon^5 \psi^{(5)} + \dots$$

The Navier–Stokes equation dictates that $\psi^{(2)} = \psi_{21}^{(2)}(r, t) \cos 2\theta$ and $\psi^{(3)} = \psi_{31}^{(3)}(r, t) \cos 3\theta$. The matching condition at $O(\varepsilon^5)$ yields the correction, of $O(\varepsilon^4)$, to the traveling speed

\dot{Y} ,

$$(19) \quad \dot{Y}^{(4)} = \frac{\pi}{2} \int_0^\infty \frac{\partial a}{\partial r} \psi_{21}^{(2)} \psi_{31}^{(3)} r dr - \frac{q_2}{4}, \quad \text{where } a = -\frac{1}{v^{(0)}} \frac{\partial \zeta^{(0)}}{\partial r}; \quad \zeta^{(0)} = \frac{1}{r} \frac{\partial}{\partial r} (r v^{(0)}).$$

Here $v^{(0)}$ and $\zeta^{(0)}$ are respectively the local azimuthal velocity and the axial vorticity at $O(\varepsilon^0)$, the leading order, and q_2 is the strength of quadrupole of $O(\varepsilon^2)$.

Moreover, we notice that two terms in $\dot{Y}^{(4)}$ gives the same contribution, and as a consequence, $\dot{Y}^{(4)} = -q_2/2$. The eventual formula for the translation speed of a vortex pair includes the strength of the second-order quadrupole field only and is expressed, in terms of the dimensional variables,

$$(20) \quad \dot{Y} \approx -\frac{\Gamma}{4\pi d} \left(1 + \frac{2\pi}{\Gamma d^2} q \right); \quad q = \varepsilon^2 q_2; \quad \psi_{\text{right}} = -\frac{\Gamma}{2\pi} \log r + q \frac{\cos 2\theta}{r^2} + \dots$$

REFERENCES

- [1] Helmholtz, H. von.: Über integrale der hydrodynamischen gleichungen welche den wirbelbewegungen entsprechen. Crelles, J. **55**, 25 (1858). English translation by Tait, P. G.: On integrals of the hydrodynamical equations which express vortex-motion. Phil. Mag. (4) **33**, 485–512 (1867).
- [2] Lamb, H.: Hydrodynamics, Chap. 7. Cambridge University Press (1932).
- [3] Fukumoto, Y.: Global time evolution of viscous vortex rings. Theor. Comput. Fluid Dyn. **24**, 335–347 (2008).
- [4] Kelvin, Lord: On the stability of steady and of periodic fluid motion. Phil. Mag. **23**, 459–464 (1878).
- [5] Arnol'd, V. I.: Sur la géométrie différentielle des groupes de Lie de dimension infinie et ses applications à l'hydrodynamique des fluides parfaits. Ann. Inst. Fourier Grenoble **16**, 319–361 (1966).
- [6] Bahrami, F., Nycander, J. and Alikhani, R.: Existence of energy maximizing vortices in a three-dimensional quasigeostrophic shear flow with bounded height. Nonlinear Anal. Real World Appl. **11**, 1589–1599 (2010).
- [7] Benjamin, T. B.: The alliance of practical and analytical insights into the nonlinear problems of fluid Mechanics. Lecture Notes in Math. No. 503, 8–29, Springer-Verlag, Berlin (1976).
- [8] Moffatt, H. K.: Structure and stability of solutions of the Euler equations: a lagrangian approach. Phil. Trans. R. Soc. Lond. A **333**, 321–342 (1990).
- [9] Fukumoto, Y. and Moffatt, H. K.: Kinematic variational principle for motion of vortex rings. Physica D **237**, 2210–2217 (2008).
- [10] Donnelly, R. J.: Quantized Vortices in Helium II. Chap. 1. Cambridge University Press (1991).
- [11] Jones, C. A. and Roberts, P. H.: Motions in a Bose condensate: IV. Axisymmetric solitary waves. J. Phys. A: Math. Gen. **15**, 2599–2619 (1982).
- [12] Saffman, P. G.: The velocity of viscous vortex rings. Stud. Appl. Math. **49**, 371–380 (1970).
- [13] Stanaway, S. K., Cantwell, B. J. and Spalart, P. R.: A numerical study of viscous vortex rings using a spectral method. NASA Technical Memorandum **101041** (1988).
- [14] Fraenkel, L. E.: Examples of steady vortex rings of small cross-section in an ideal fluid. J. Fluid Mech. **51**, 119–135 (1972).
- [15] Fukumoto, Y. and Moffatt, H. K.: Motion and expansion of a viscous vortex ring. Part 1. A higher-order asymptotic formula for the velocity. J. Fluid Mech. **417**, 1–45 (2000).
- [16] Tung, C. and Ting, L.: Motion and decay of a vortex ring. Phys. Fluids **10**, 901–910 (1967).
- [17] Fukumoto, Y. and Kaplanski, F.: Global time evolution of an axisymmetric vortex ring at low Reynolds numbers. Phys. Fluids **20**, 053103 (2008).
- [18] Fukumoto, Y. and Habibah, U.: Finite thickness effect on speed of a counter-rotating vortex pair. submitted to *Fluid Dyn. Res.* (2016).

Food rheology: wheat grain hardness and wheat flour dough

Bob Anderssen and Reka Haraszi

CSIRO Data61, GPO Box 664, Canberra, ACT2601, Australia
and
Campden BRI, Station Road, Chipping Campden GL55 6LD, UK

The ready availability of food is a direct consequence of a number of key factors: historical and continuing plant breeding; the efficient harvesting of different types of materials (picking of a mango at a time that guarantees its ripening continues); the processing of the resulting produce to make food. All such steps involve a consideration of various aspects of material properties all of which involve information recovered from scientific experimentation, statistics and mathematical analysis and modelling. Here, the focus is wheat and, in particular, the material properties of wheat grains in relation to the wheat dough made from their flours and, subsequently, to the products made from the dough.

1. INTRODUCTION

At all stages in the production of food from plants, the properties of the materials at each step in the manufacturing process must be taken into account in order to guarantee cost-effective and quality end products. For example, in the processing of wheat, different sequences of material properties must be managed depending on the end product to be produced. In particular, for breads, cakes, noodles and pasta, the starting point is the choice of the wheat variety to be harvested which is then milled to produce the flour that is mixed with water and other components to make the dough, and then baked or dried to produce the planned end product.

The role and importance of mathematics in the study of the properties of wheat is reflected in the fact that hard wheats make great breads, soft wheats make excellent biscuits and cakes, durum wheat make great pasta (if correctly dried), and Australian wheat has been specifically bred to make noodles for the Japanese market.

Mathematics plays an important role starting with the plant breeding, the growing of the wheat and its subsequent harvesting.

With respect to the plant breeding, not only is experimental design involved, but also the rapid testing of a huge number of possibilities that result from a breeding trial. The testing involves, as well as grain quality, a wide variety of other considerations such as disease resistance, environmental stress tolerance and plant architecture. The last mentioned relates to how the plants will be harvested.

The focus here is the processing of the wheat grains after their harvesting. Though the subsequent processing are important, especially from the perspective of cost effectiveness, the fundamental determinant of end product quality is the harvested grain. In fact, the variety and its associated grain hardness are the key determinants. The breeding puts the varieties into bread, cake, biscuits, noodles and pasta equivalence

classes. The hardness of the grain determines how the grain should be milled to make the flour and can to a certain extent be used as a predictor of end product quality.

The role of mathematics with respect to the following material property stages in the processing of wheat to make bread and cakes will be considered: the rheology of grain hardness; the milling of wheat to make flour; and the mixing of flour with water and other ingredients to make the dough.

In the study of grain hardness, an overriding goal is the determination of the extent to which the measurement of grain hardness characteristics can be used as predictors of dough properties and end product quality. As explained below, mathematics is playing a key role in doing this.

2. THE MODELLING AND MEASUREMENT OF GRAIN HARDNESS

There are various ways in which wheat grain hardness has been assessed. Many are based on an analysis of the flour that they produce. Direct measurement of the actual hardness of individual grains can be performed using the SKCS 4100 device (Perten Instruments, Sweden) which measures, as an individual crush response profile (iCRP), the force with which an individual grain resists its crushing [1, 2]. Some representative iCRPs are plotted in Figure 1.

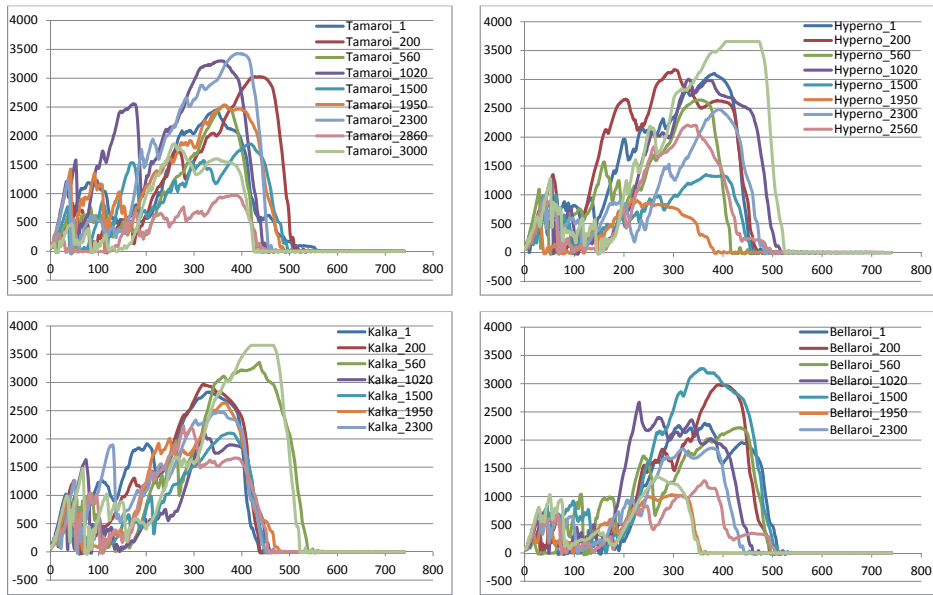


FIGURE 1. Some representative iCRPs for different durum varieties. The numbers refer to kernel numbers chosen at random of a larger sample in order to highlight the variation in iCRP structure.

The importance of such measurements is that the averaging of a large number (greater than 300) of randomly chosen iCRPs from the same wheat variety consistently gave the same average crush response profile (aCRP), as illustrated for a number of wheat varieties in Figure 2. As observed by Osborne and Anderssen [1], the structure of an aCRP represented a summary of the rheological response of a grain to its crushing: elastic response of the shell; the fragmentation of the shell and endosperm;

the viscoelastic response to the resulting granular material; the further collapse of the granular material. The rheological phenotype phases (RPPs) chosen to summarize the different phases in the rheological structure of an aCRP are illustrated in Figure 3.

The role of the averaging of a large number of iCRPs to obtain the underlying associated aCRPs was the need to average out all the variability associated with the individual measurements of iCRPs.

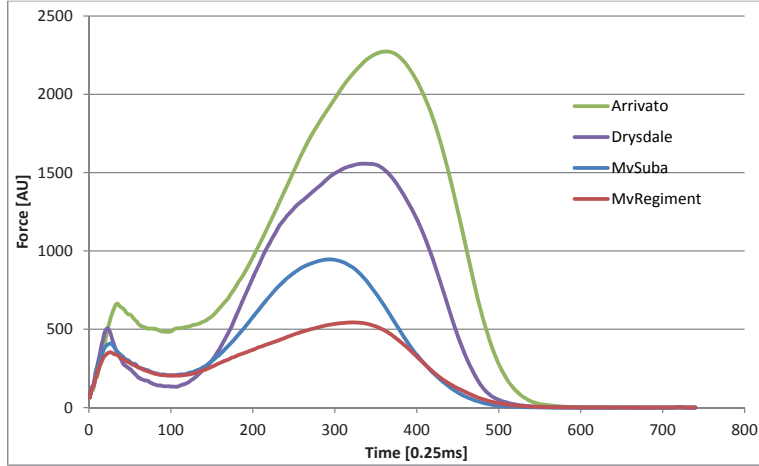


FIGURE 2. Average crush response profile (aCRP) of four wheat varieties representing different hardness classes: Arrivato (durum), Drysdale (hard), MvSuba (medium hard) and MvRegiment (soft).

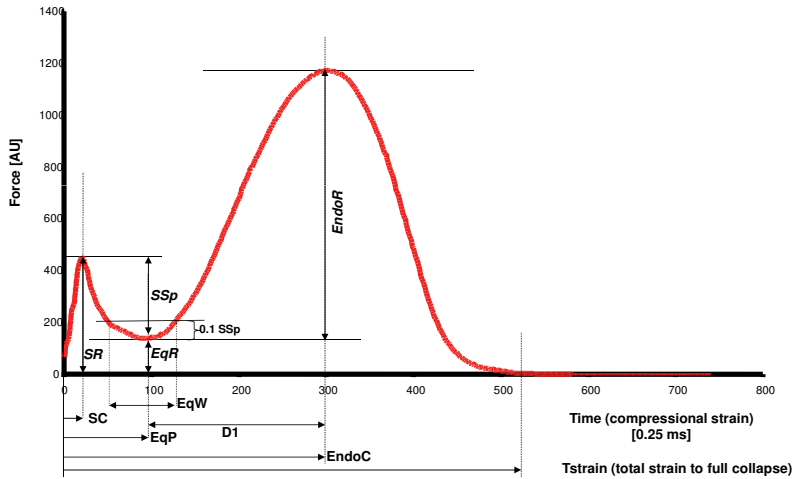


FIGURE 3. The rheological phenotype phases (RPPs) of an aCRP. Modified Figure 1 in [3].

Here, the relevant mathematics involved is quite simple involving averaging and determining the RPPs, and the correlation of properties of wheats with the RPPs. The

key step was the identification of the rheological interpretation of an aCRP in terms of how a wheat fragments under compression. Further details about the meaning of the RPPs, how they correlate and how they can be utilized to separate wheats into well-defined hardness classes can be found in [3].

3. THE MILLING WHEAT TO MAKE FLOUR

The flour of wheat depends on its hardness. In fact, the particle size index (PSI) [4] and the particle size distribution (PSD) [5] of the flour that a wheat produces represent qualitative ways to decide on whether that wheat should be classified as either hard or soft.

In turn, the hardness of the wheat to be milled must be taken into account in designing the milling configuration to be used. Here, commercial considerations play a central role, as the key goal, in performing the milling, is the maximization of the milling yield which measures the proportion of flour extracted [6].

Here, mathematics has been used to model grain shape [7] and the breakage process performed in the milling [8, 9].

4. THE MIXING OF WHEAT FLOUR DOUGH

The mixing of a wheat flour dough transforms the starting mixture of flour, water and additives into a biopolymer. An excellent example of the special properties of the biopolymer that results from the mixing of just durum semolina and water is illustrated in Figure 4.

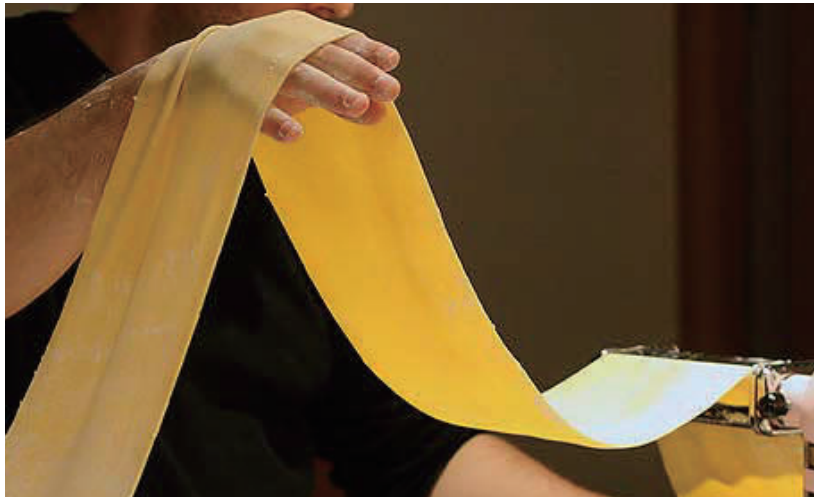


FIGURE 4. The durum dough biopolymer. From a “KitchenAid Stand Mixer” advertisement on Google Images.

This happens because the interaction of water with the gluten polymers in wheat flour is exothermic. The seminal experiment which established this fact was the temperature measurements of Li and Walker [10] of the mixing of a dough on a Mixograph.

A detailed discussion about the interpretation of their measurements and its importance in understanding the open loop hysteresis stress-strain dynamics of the mixing (Figure 5), which measures the elastic energy accumulation associated with the dough’s viscoelastic development, can be found in Anderssen [11].

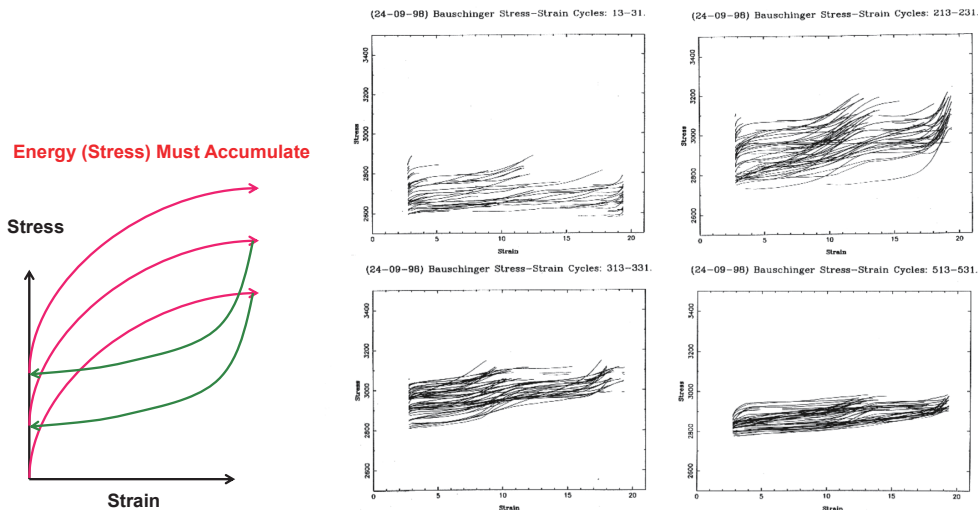


FIGURE 5. A stress accumulating open loop hysteresis (on the left) and experimental record of the upper successive loops from a mixing of a wheat flour dough (on the right) (Figure 7.8 in [11]).

There is a well established theory for closed loop hysteresis based on the Preisach hysteresis concept that the hysteretic behaviour of a material is the sum of the elementary hysteretic behaviour of the small domains that make up the material [12, 13].

For the modelling of open loop hysteretic processes, a different approach is required, such as representing the stress-strain dynamics of the mixing as a system of Duhem-Madelung hysteresis operators (Duhem-Madelung pairs) [14].

Interestingly, the rainflow counting ansatz of fatigue analysis [15, 16] can be utilized to perform a unique decomposition of a Mixograph into a rainflow counting matrix (two-dimensional histogram) of Duhem-Madelung pairs and an irreducible string. Interestingly, though the possibility has not been pursued, the irreducible strings represent a simple quantitative way of putting wheats into equivalence classes.

The observed rate independent of the mixing of a wheat-flour dough to peak dough development [17] has been modelled as the time evolution of a rate-independent elastic process [18].

Acknowledgments. The authors thank Mike Sissons (NSW DPI, Tamworth, Australia) and Mariann Rakszegi (AI CAR HAS, Martonvasar, Hungary) for performing the SKCS measurements. Further details about the analysis of this SKCS data can be found in [3].

REFERENCES

- [1] B. G. Osborne and R. S. Anderssen. Single-kernel characterization principles and applications. *Cereal Chemistry*, 80:613–622, 2003.

- [2] R. S. Anderssen and R. Haraszi. Characterizing and exploiting the rheology of wheat hardness. *Euro. Food Res. Tech.*, 229:159–174, 2009.
- [3] R. Haraszi, A. Juhasz, M. Sissons, M. Rakszegi, L. Tamas, and R. S. Anderssen. Rheological Hardness Index for Assessing Hardness of Hexaploids and Durums. *Cereal Chem.*, 90:430–438, 2013.
- [4] K. J. Symes. The inheritance of grain hardness in wheat as measured by the particle size index. *Crop and Pasture Science*, 16:113–123, 1965.
- [5] G. A. Hareland. Evaluation of flour particle size distribution by laser diffraction, sieve analysis and near-infrared reflectance spectroscopy. *Journal of cereal science*, 20:183–190, 1994.
- [6] A.-L. Choy, C. K. Walker, and J. Panozzo. An investigation of wheat milling yield based on grain hardness parameters. *Cereal Chemistry*, 92:544–550, 2015.
- [7] F. Mabille and J. Abecassis. Parametric modelling of wheat grain morphology: a new perspective. *Journal of Cereal Science*, 37:43–53, 2003.
- [8] G. M. Campbell, C. Sharp, K. Wall, F. Mateos-Salvador, S. Gubatz, A. Huttly, and P. Shewry. Modelling wheat breakage during roller milling using the double normalised kumaraswamy breakage function: Effects of kernel shape and hardness. *Journal of cereal science*, 55:415–425, 2012.
- [9] K. F. Fuh, J. M. Coate, and G. M. Campbell. Effects of roll gap, kernel shape, and moisture on wheat breakage modeled using the double normalized kumaraswamy breakage function. *Cereal Chemistry*, 91:8–17, 2014.
- [10] A. Li and C. E. Walker. Dough temperature changes during mixing in a mixograph. *Cereal chemistry*, 69:681–683, 1992.
- [11] R. S. Anderssen. Chapter 7, wheat-flour dough rheology. In P. Belton, editor, *The Chemical Physics of Food*. Blackwell Publishing Oxford, 2007.
- [12] I. D. Mayergoyz. Mathematical models of hysteresis. *Magnetics, IEEE Transactions on*, 22:603–608, 1986.
- [13] I. D. Mayergoyz. *Mathematical models of hysteresis and their applications*. Academic Press, 2003.
- [14] R. S. Anderssen, I. G. Götz, and K.-H. Hoffmann. The global behavior of elastoplastic and viscoelastic materials with hysteresis-type state equations. *SIAM Journal on Applied Mathematics*, 58:703–723, 1998.
- [15] M. Brokate, K. Dressler, and P. Krejci. Rainflow counting and energy dissipation for hysteresis models in elastoplasticity. *European journal of mechanics A/Solids*, 15:705–737, 1996.
- [16] M. Brokate and J. Sprekels. *Hysteresis and phase transitions*, volume 121. Springer Science & Business Media, 2012.
- [17] R. S. Anderssen, P. W. Gras, and F. MacRitchie. The rate-independence of the mixing of wheat flour dough to peak dough development. *Journal of Cereal Science*, 27:167–177, 1998.
- [18] R. Anderssen and Kružík Martin. Modelling of wheat-flour dough mixing as an open-loop hysteretic process. *Discrete and Continuous Dynamical Systems-Series B*, 18:283–293, 2013.

Electrostatic Desalter Optimisation

Trina Dreher

Suez Oil & Gas Systems

As crude oil is extracted from the ground it is usually accompanied by emulsified water and dissolved salts that must be removed to avoid downstream production issues. Electrostatic desalters are typically employed to purify the crude oil before further processing. As such, the phase separation of water in crude oil emulsions is an essential process in oil production however, it is a highly complex and poorly understood phenomenon.

A long list of operating variables and physical properties affects the efficiency of electrostatic desalters and given the difficulty of isolating individual factors it is unsurprising that no comprehensive theory has yet been developed. Instead, it is accepted that many different mechanisms work simultaneously on an emulsion subjected to an electric field such that the overall droplet growth is a balance between the hydrodynamic, electrostatic, chemical and physical properties of the emulsion. Given the difficulty in modelling these processes it is not surprising that, in general, the design of commercial electrostatic desalter equipment is performed using lab and pilot plant data and empirical correlations.

Even so desalter operation is governed by the general principles of drop coalescence and phase separation. Electrostatic desalters are essentially gravity separation devices governed by Stokes law so coalescing drops to form larger drops that settle more rapidly is a key to operational efficiency. In general, the coalescence of drops consists of three steps: (1) motion and approach of drops due to electrostatic force, (2) drainage of the film separating the drops and (3) breakdown of the film and coalescence of the drops. The electrical effect is primarily related to the first step, i.e. an increased rate of motion of the drops where the dipolar force induces mutual attraction between neighbouring drops due to the interaction of the dipoles induced by the electric field. Therefore, a second key to operational efficiency is adequate mixing of the emulsion to ensure the highest chance of contact and coalescence between the drops when subjected to the electric field.

Suez Oil & Gas Systems designs electrostatic desalters via a proprietary calculation spreadsheet based on a combination of theoretical and empirical data, which has proven accurate for relatively straight-forward design cases (mid-range API gravity crude oil, low basic sediment and water [BS&W]). However, to meet current market demands we wish to extend the spreadsheet for light and heavy crude oils and higher levels of BS&W. As we have little access to field data that could be used to correlate the design calculations, which is the preferred way to adjust the calculations, we seek a better understanding of electrostatic desalter theory and how it and experimental lab data relates to practical package design in order to remain competitive in the electrostatic desalter market.

1. INTRODUCTION

Crude oil produced from most oil fields is accompanied by water. The water is usually emulsified and contains dissolved salts such as chlorides of sodium, calcium and magnesium. This emulsified water and salts must be removed from the crude oil to avoid downstream processing issues such as corrosion, scaling, complications due to increased viscosity due to finely dispersed water drops in the crude oil, and the deactivation of catalysts by water. Furthermore, the presence of water adds to the transport and production costs hence there are a number of commercial reasons for removing emulsified water from the crude oil. The emulsified water drop diameter is typically in the order of 20 microns and as such, will not separate under gravity in a reasonable length of time so alternate methods are required to separate the water from the oil.

There are several methods available to remove a dispersed water phase from a continuous phase such as chemical demulsification, gravity or centrifugal settling, pH adjustment, filtration, heat treatment, membrane separation and electrostatic demulsification. Each of these methods has its own advantages and disadvantages however, electrostatic treatment has proven to be an efficient means of separating water in oil emulsions and the most suitable for crude oil emulsions [1]. The terms dehydration and desalting are used synonymously to describe the removal of water and/or salt from crude oil. In addition, during the desalting process solids present in the emulsion settle and are removed from the bottom of the vessel.

During crude oil desalting, water is mixed with the oil so that the salts can be diluted in water and washed from the organic phase. Some of the mixed water then forms an emulsion that must be demulsified to separate the water from oil. The emulsion enters a desalter vessel where it is subjected to a high voltage electric field. The field is induced by AC or DC current, although AC is more common. The electrostatic forces generated cause the drops to become polarised and attracted to each other causing the drops to collide and coalesce forming larger drops, which then settle due to gravity

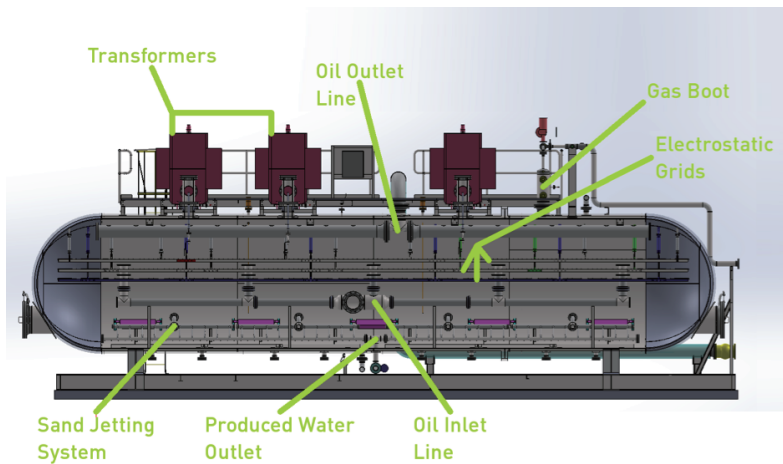


FIGURE 1. Cross-section of a typical crude oil desalter package



FIGURE 2. Typical crude oil desalter package

according to Stokes law. Larger drops settle more quickly so a key to desalting is to efficiently coalesce water drops to form larger drops.

A schematic of a typical crude oil desalter vessel is given in Figure 1 and a photo of a completed package in Figure 2. In the photo the oil inlet line is shown in the foreground and the transformers can clearly be seen on top of the desalter vessel.

2. THEORY

Ever since the 1911 invention of an electrostatic precipitator by Frederick Cottrell [2] there has been great interest in understanding and improving the process. It is known that several parameters affect the demulsification kinetics of water in oil emulsions and therefore the efficiency of an electrostatic desalter. The operating conditions to consider include the voltage, frequency, temperature, degree of mixing, and electrode configuration and the emulsion properties include the density, viscosity, interfacial tension, water drop size, holdup, surfactant concentration in the oil phase and the electrolyte concentration in the water phase [3]. With so many parameters to consider it is unsurprising that no comprehensive theory has been developed, especially since it is difficult to isolate individual factors, which has also contributed to contradictory results being obtained by different researchers. However, what can be said is that when a water in oil emulsion is treated in an electrostatic coalescing device it appears that there are many different mechanisms working simultaneously on the emulsion such that the overall droplet growth is a delicate balance of the hydrodynamic, electrostatic, chemical and physical properties of the emulsion being treated. Even so, electrostatic desalters are

essentially gravity separation devices governed by Stokes law:

$$V = \frac{2r^2\Delta\rho g}{9\mu_0}$$

where V = settling rate, m s^{-1}

r = drop radius, m

$\Delta\rho$ = density difference between aqueous and organic phases, kg m^{-3}

g = gravity, m s^{-2}

μ_0 = viscosity of oil, $\text{kg m}^{-1}\text{s}^{-1}$

Therefore, it is clear that an increased settling rate results from increasing the water drop diameter, increasing the density difference between the phases and decreasing the oil viscosity. The density and viscosity can be altered via temperature and the drop size controlled via the applied electric field. The practical operating temperature range is around 100–250 °C to avoid vaporization of the crude oil. In addition, crude oil conductivity increases with temperature thereby increasing power requirements and heating costs. It should be noted that although the above equation requires modification to account for multiple drops in a vessel the important point to note is that the settling velocity is proportional to the square of the drop size which indicates the importance of drop coalescence prior to phase separation. However, the electrical coalescence of drops is poorly understood due to the complexity of the hydrodynamic and electrical phenomenon of interfacial polarization.

In general, the coalescence of drops consists of three steps: (1) motion and approach of drops due to electrostatic force, (2) drainage of the film separating the drops and (3) breakdown of the film and coalescence of the drops. The electrical effect is primarily related to the first step, i.e. an increased rate of motion of the drops in an electric field. It is known that an electric field will assist in the separation of water in oil dispersions. Although many possible mechanisms have been proposed the mechanisms are not clearly understood other than the electrical forces facilitate the coalescence between small drops in order to attain larger drops that separate rapidly under gravity separation. Generally the coalescence rate increases as the applied electric field strength increases however, if the strength becomes too high then various drop breakup mechanisms can occur.

The dipolar force is considered to be one of the principal causes of drop coalescence. It induces mutual attraction between neighbouring drops due to the interaction of the dipoles induced by the electric field. The classical equation for dipole-dipole interaction between two similar spherical drops is:

$$F = \frac{24\pi\epsilon_0\epsilon_1r^6E^2}{(d+2r)^4}$$

where F = electrostatic force, N

ϵ_0 = permittivity of vacuum, F m^{-1}

ϵ_1 = dielectric constant of the continuous phase

r = drop radius, m

E = the electric field strength, V m^{-1}

d = distance between the near surfaces of the two drops, m

Although this equation is only a first order approximation to the actual short range force and ignores drop deformation, it indicates that the dipolar force is strongly dependent on the water drop size and the space between the drops. Therefore, as the

water content of the emulsion is reduced during the desalting process, due to ongoing phase separation, the effect of dipolar attraction will decrease as the distance between drops increases. In addition, large drops will separate quickly leaving small drops dispersed in the emulsion resulting in a further decrease in the contribution of dipolar attraction.

As electrostatic forces are essentially short range forces, when the drop spacing is large other forces are needed to bring the drops into close proximity and to allow the electrostatic forces to contribute to coalescence. This is primarily achieved via mechanical mixing of the emulsion prior to entry into the desalter vessel and via optimising the shape of the vessel to favour turbulence and mixing. However, too high turbulence will induce drop breakup and re-dispersion thereby decreasing the desalter efficiency.

3. PROCESS DESIGN

Electrostatic desalting is a complex but poorly understood process within the Oil and Gas industry. As such, most commercial designs are based on one of the first successfully operating units and few major design advances have been made since the installation of these original units. In addition, due to the difficulty in modelling the processes that occur during electrostatic desalting, in general the design of electrocoalescer equipment is carried out using lab and pilot plant data and empirical correlations.

Electrostatic desalters may encompass a one or two stage treatment (i.e. one or two desalter vessels operated in series) depending on the inlet and outlet water, salinity and sediment specifications. Typically the dehydration efficiency for one and two stage units is 95% and up to 99% respectively. Electrostatic desalters reduce basic sediment and water (BS&W) content from 5–10 v/v% to approximately 1.4–2.8 v/v%, which in the units conventionally used by the industry is equivalent to 5–10 PTB (pounds per thousand barrels of crude oil). The inlet salt concentration is typically in the order of 3–200 PTB and has to meet an outlet concentration of less than 10 PTB.

Suez Oil & Gas Systems (SOGS) has been designing and supplying electrostatic desalters for many years, principally to the Middle East region. Sizing of the desalter is calculated via a proprietary design spreadsheet where the inputs include the oil density, viscosity, water salinity, operating temperature, oil flow rate, water flow rate and vessel diameter. Various calculations then determine the required electrostatic grid area, vessel length and power based on the drop settling velocity. An adjustment for BS&W is made by factoring the base case settling velocity.

This design spreadsheet has proved accurate for relatively straight-forward design cases where the API gravity of the crude oil is mid-range and the BS&W is low. However, we are seeing more applications for light or heavy crude oils and higher levels of BS&W and need to have confidence in the design output for these cases.

The design spreadsheet has been used by SOGS for many years and over that time details as to its origins have been lost and various modifications made to the extent that at this point we are unable to determine the exact source of the theory and/or empirical data used in the various calculations. As such, currently we are unable to optimise the design calculations or determine if correction factors are required for the more difficult design cases we now regularly see. We suspect that the calculations are largely based on empirical data however, as we do not know the data's origin we are unsure of its validity range. As a consequence we are currently forced to add relatively large design margins to our desalter equipment that has the potential to make our packages uncompetitive, especially in the current tight economic market that the

Oil and Gas industry is experiencing. Although there is much theory published on electrostatic coalescence and its application to desalters it is not clear how this theory relates to practical desalter design.

Given the industry’s traditional reliance on empirical correlations for electrostatic desalter design SOGS approached various clients to obtain field data from installed packages. Unfortunately little information has been forthcoming either because the packages are yet to be commissioned or due to the reluctance of Oil and Gas companies to share highly confidential operating information or adjust parameters away from operating values for the purposes of testing. Therefore, SOGS seeks a better understanding of electrostatic desalter theory and how it and experimental lab data relates to practical package design in order to remain competitive in the electrostatic desalter market.

4. CONCLUSION

Electrostatic demulsification is commonly used in the Oil and Gas industry to remove water and salts from crude oil before further processing. Since the invention of the electrostatic precipitator in the early 20th century much work has been done on the use of electrostatic forces to enhance phase separation however, it remains a highly complex and poorly understood process. From the current body of work it appears that there are many different mechanisms working simultaneously on a water in oil emulsion subjected to an electric field such that the overall droplet growth is a delicate balance of hydrodynamic, electrostatic, chemical and physical properties of the emulsion being treated. Given the difficulty in modelling these processes it is not surprising that, in general, the design of commercial electrocoalescer equipment is performed using lab and pilot plant data and empirical correlations.

Suez Oil & Gas Systems designs electrostatic desalters via a proprietary calculation spreadsheet based on a combination of theoretical and empirical data, which has proven accurate for relatively straight-forward design cases (mid-range API gravity crude oil, low BS&W). However, we wish to extend the spreadsheet for light and heavy crude oils and higher levels of BS&W in order to meet current market demands. As we have little access to field data that could be used to correlate the design calculations we seek a better understanding of electrostatic desalter theory and how it and experimental lab data relates to practical package design in order to remain competitive in the electrostatic desalter market.

REFERENCES

- [1] Eow, J., Ghadiri, M., Sharif, A., Williams, T., Electrostatic enhancement of coalescence of water droplets in oil: a review of the current understanding, *Chem. Eng. J.*, 84 (2001), 173–192.
- [2] Cottrell, F., Process for separating and collecting particles of one liquid suspended in another liquid, US Patent 987114, 1911.
- [3] Hano, T., Ohtake, T., Takagi, K., Demulsification kinetics of W/O emulsion in an A.C. electric field, *J. Chem. Eng. Jpn.*, 21 (4) 1988, 345–351.

Water — New challenges

Veronique Bonnelye

Suez Water & Treatment Solutions

1. INTRODUCTION

The objective of this paper is to give an overview of the different fields where mathematics is used, or can be developed to assist in, the understanding and prediction of water processes. Water treatment groups different processes and technologies together to treat and separate impurities from water and provide a final product to the end user, the customer. Water is one of the most effective and accessible services supplied, and drinking water is also one of the most monitored products for human consumption. There are not one, but several treatment steps along the water cycle; from natural resource to drinking water or process water, from waste water to environment or recycling, from recycling to drinking water or process water. Nowadays, the main water treatment challenges are related to optimisation and rationalisation: improve the security, reduce the cost and the environmental footprint (energy, waste) and finally meet the customer expectations.

2. WATER TREATMENT PROCESSES

The most conventional drinking water processes separate particles, silt, and suspended solids by physical separation (clarification, filtration). Separation is enhanced by the use of chemical compound to bond the particles together. Coagulation and flocculation processes use a range of mineral (ferric and aluminium ions) and organic media, including large molecular weight compounds (polydadmec, polyacrylamide).

As water quality objectives evolve, more pollutants are targeted. Table 1 gives examples of pollutants and processes used in water production. As the feed water quality degrades, and the water quality requirements increase in the final product, processes and technologies need to be optimised and better controlled, operated and maintained. Hydraulics models and CFD are actively used to design and improve the reactors implemented to house those reactions and separation processes (Figure 1). Process modelling and development of new instrumentation for monitoring are keys to increasing the reliability and efficiency of the full scale installations.

One key field of development concerns the full automation and mastering of simple processes such as coagulation-filtration-clarification: how to adjust the dosing of different chemicals used to adapt the treatment to the variable resource water quality. Process optimisation is driven by new water quality standards and guidelines, as well as degradation of water resources quality (due to pollution and or exposure to larger range of weather events, from long periods of drought to heavy rain events and flooding).

3. PROCESS MODEL — THE QUEST FOR THE HOLY GRAIL

Facing degraded water quality, variable water resources, multi-barrier approach, and more stringent final quality targets, optimisation of a water treatment plant becomes

Compounds	Water Treatment Process
Silt and particles	Coagulation, flocculation (chemically assisted), settling, floatation, cloning
Natural organic matter	Coagulation, adsorption
Micropollutants (pesticides, herbicides) Natural toxins (algae toxins)	Adsorption on activated carbon, oxidation and advance oxidation (ozone, UV coupled with H_2O_2)
Hardness, alkalinity, salts	Ion exchange (resin), precipitation, evaporation, reverse osmosis
Assimilable organic carbon, some micropollutants and toxins, nitrate	Biological process (biofiltration)
Pathogen microorganisms including bacteria, protozoa and virus	Filtration (sand filters, ultrafiltration and micro-filtration membranes, reverse osmosis), oxidation (chlorine and chloramines, ozone, UV)

TABLE 1. Examples of compounds and water treatment processes

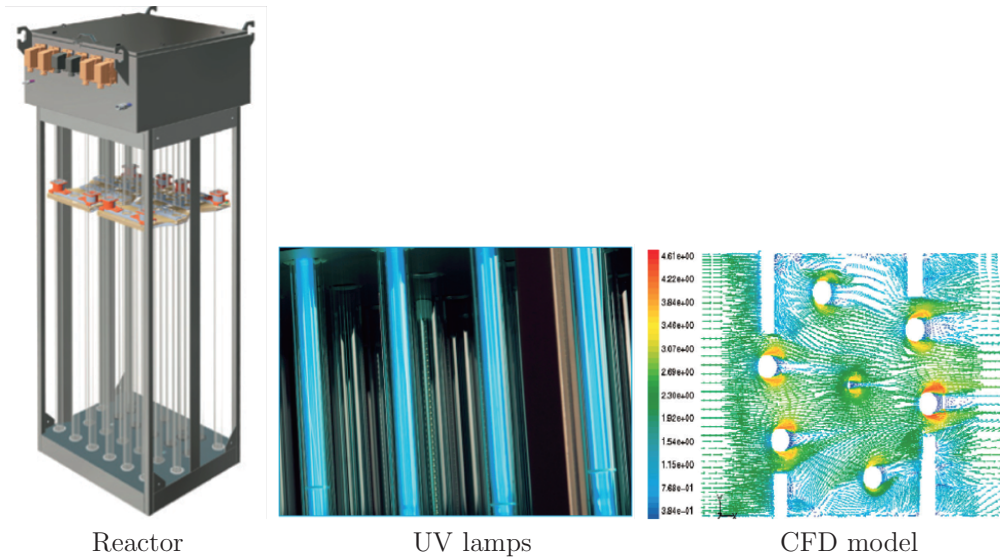


FIGURE 1. Example of CDF UV reactor — Aquaray HO (SUEZ Ozonia)

more and more difficult. Process models are developed to assist the operations team in the daily operation activity to ensure the design targets are met, but also so that the plant is always operated at its optimum points of efficiency (water efficiency, power efficiency, lower operation cost). The models used to optimise the processes depend on the reactions, and are usually a combination of multiple layers of process models. Control relies on on-line monitoring. Data management appears critical for the large systems. Tools are also developed to assist in the training of the operator. As an example, SUEZ developed a Process Simulation System (PSS), a virtual replication of

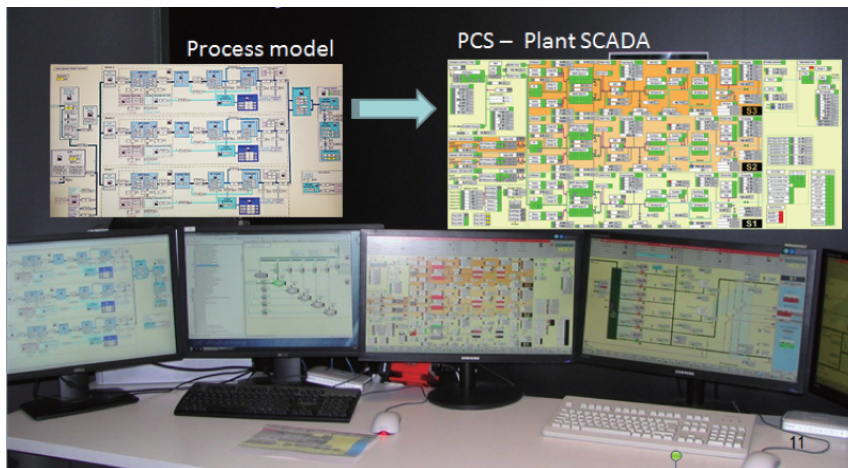


FIGURE 2. Desalination plant process modelling, Victorian Desalination Plant “flight simulator” [1].

the Melbourne Desalination Plant processes and control system. This “flight simulator” is used for the training of the plant operations team [1]. The PSS consists of a process simulation (ControlBuilt software) to provide dynamic feedback to an off line copy of a Plant Control System (Siemen PSC7)(Figure 2). The PSS simulates the plant hydraulics (flow, pressure) and part of the water treatment processes (reverse osmosis and remineralisation processes). Nevertheless, most of the processes involved in water treatment are still difficult to describe with a process model, due to the lack of proper characterisation of the compounds and understanding of the fundamental reactions involved.

4. WATER SERVICE TO CUSTOMER — TRANSFER OPTIMISATION

An often forgotten part of water production is the distribution system. This significant water production asset is a common source of leaks and possible water quality degradation. Responsible for an important part of the power consumption, the water transfer system is under scrutiny to improve both operation and maintenance costs. For example, several water operations across Australia, including Adelaide, are currently optimising their distribution system operating pressure in accordance with water demand to reduce water loss, burst frequency and energy consumption [2]. By reducing the pressure between 17 and 30%, the model predicts a reduction of 11 to 60% of busts, leakages (operation savings), energy, as well as increased asset life. This modelling requires managing a large number of monitoring points to optimise the network at a regional level.

Another example of water transfer optimisation is the study performed by MIT on the Saudi Arabia drinking water network, using a new network flow model called INFINIT (interdependent network flows with induced internal transformation) [3]. The model (Figure 3) is designed to allow multi-objective functions such as the total cost (CAPEX and OPEX) and the total CO₂ emission, and to both evaluate and refine complex scenarios addressing the location of water and energy investments.

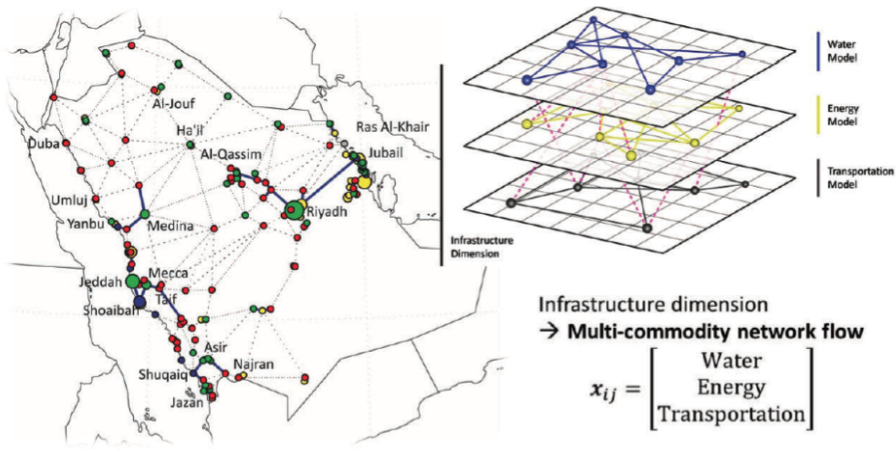


FIGURE 3. KSA Multi-Dimensional Infrastructure Network [3].

5. CONCLUSION — NEW CHALLENGES IN WATER TREATMENT

To increase process efficiency and control to achieve more stringent objectives, and increase security of supply by improved reactor design and process modelling are the new challenges of water production and distribution. In terms of process improvement, modelling is required to enhance the control, moving from feedback to forward control, increasing the reliability of the systems and allowing continuous optimisation and fully automated systems. Coming back to the “traditional” coagulation-flocculation process, we are still far from mastering the different reactions and processes, even if important progress has been made thanks to new instrumentation.

Modelling of processes at the water plant level, as well as in the distribution network (energy efficiency, operating cost and asset life), and modelling of water treatment and transfer at the region, State and Country levels to optimise water management, investment and operation costs are the next fields of improvement.

REFERENCES

- [1] Bonnelye, V., C. Rodriguez, G. Mercer and M. Jury, Innovative Flight Simulator to Secure Drinking Water Plant Operation: a Case Study, Australian Water Association, National Operation Conference, Cairns, 28–30 October 2014.
- [2] Fumex A., P. Vizioli, D. Sinapah, M. Nicholas, Pressure Management in Adelaide Metropolitan Network — Feasability Study, Ozwater15, Adelaide.
- [3] Ishimatsu, T., A. Doufene, A. Alawad, O. L. de Weck, Desalination Network Model Driven Decision Support System: A Case Study Of Saudi Arabia, IDA World Congress, San Diego, August 2015.

The biological treatment of wastewater

Mark Nelson

School of Mathematics and Applied Statistics, University of Wollongong, Wollongong,
Australia

1. THE HISTORY OF THE ACTIVATED SLUDGE PROCESS

In the first half of the nineteenth century the use of sewage systems emerged as a mechanism for the removal of sewage in cities. This replaced older processes which at one extreme simply involved the emptying of chamber pots into the street. However, sewage systems do not treat wastewater; they merely move the waste from one location to another. The need to actively clean wastewater, due to the role played by untreated water in spreading waterborne diseases, became clear by the mid 1880s. The need to produce a clean, healthy, water supply was exacerbated by both the large scale production of wastewaters and increasing population densities, both by-products of the burgeoning industrial world. These problems were particularly acute in England, leading to a Royal Commission on River Pollution being established in 1865 and re-established in 1874. The latter led to the Rivers Pollution Prevention Act (1876).

Some progress treating wastewaters containing pollutants in the form of waste organic matter was made in the second half of the 19th century using physico-chemical processes and anaerobic methods. Starting in the 1880s attempts were made at treatments based upon the biological oxidation of the pollutants. This involves bringing together a wastewater containing pollutants with aerobic microorganisms and oxygen. Biological oxidation has the potential to reduce the organic pollutants to a mixture of carbon dioxide, nitrogen, water and other compounds. These methods had little success because biological oxidation turned out to be a very slow process.

In the period 1913–1914 Edward Arden and William T. Lockett, working at the Davyhulme wastewater treatment plant (Manchester, UK), carried out a series of lab-scale experiments. During this they discovered the key step to making aerobic oxidation work. It was already known that aerobic oxidation produced a suspension, or ‘sludge’. In earlier work the resulting sediment had been removed from the reactor vessel. Arden and Lockett discovered that if the sediment was retained then the process became significantly more efficient. By retaining the sediment over a series of experiments they were able to reduce the time for “full oxidation” of sewage from weeks to less than twenty-four hours. Arden and Lockett named the sediment ‘activated sludge’, as it evidently contained an active agent that improved the process, and coined the phrase the ‘activated sludge process’.

At its heart the activated sludge process essentially entails the use of two units: an aerated biological reactor and a settling unit (or clarifier). In the former the pollutants are degraded by microorganisms (the active agent that puts the ‘activated’ into ‘activated sludge’). However, the key to the success of the activated sludge process is the use of a settling unit.

Although not directly realised at the time, aerobic microorganisms flocculate to form settleable solids. These solids are removed from the effluent stream by sedimentation and then returned to the aeration process in a more concentrated culture. It is this recycling of a concentrated activated sludge from the bottom of the clarifier to the biological reactor that drives down the time for “full oxidation” of the wastewater.

On April 3, 1914, at a meeting of the Society of Chemical Industry at the Grand Hotel in Manchester, England, Arden and Lockett presented their results in a now classic paper, “Experiments on the Oxidation of Sewage Without the Aid of Filters”, which was later published in the Journal of the Society of Chemical Industry. Following dissemination of their new method the activated sludge process was rapidly adopted by the waste-water treatment industry. By 1916 the first full-scale continuous-flow activated sludge process plant was being in use to treat wastewater at Worcester. One hundred years after this landmark event, the activated sludge process has become the most commonly used aerobic process for the biological treatment of both domestic and industrial wastewaters [19]. (Australia’s first activated sludge plant, the Glenelg Wastewater Treatment Plant, was fully operational by December 1932 [9]).

2. TOO MUCH OF ANYTHING IS BAD

Central to the success of the activated sludge process is the ‘activated sludge’. However, a significant drawback of the activated sludge process is the production of excess ‘sludge’. The expense for treating this can account for 50–60% of the total operating costs in a wastewater treatment plant [1, 4, 14]. Traditional methods for disposing of excess sludge, such as incineration, the use of landfill sites, and dumping at sea, are becoming increasingly regulated in many countries due to environmental concerns about the presence of potentially toxic elements. Furthermore, a combination of the limited amount of land available for landfill, particularly in urban areas, with increasingly stringent legislation has resulted in the economic costs of using landfill sites raising sharply. Thus there is a pressing need, and growing interest, in methods that reduce the volume and mass of excess sludge produced as part of biological wastewater treatment processes.

Excess sludge production can be reduced by increasing sludge biodegradability by disintegrating it within the reactor. This approach works primarily by disintegrating bacterial cell walls.

Although many different techniques to decrease sludge production have been investigated, the most widely adopted techniques in commercial activated sludge plants are chemical treatments and ozone treatments [15]. In these methods a part of the sludge is removed from the reactor and treated with ozone in a sludge disintegrator. This ozonation stage converts the live sludge into a mixture of soluble substrate and particulates. The liquidized sludge is then returned to the bioreactor as a feed solution where the soluble substrate is biodegraded by live sludge. This technique has been shown to lead to much lower levels of mixed liquor suspended solids (MLSS).

In practice a target value for the MLSS is specified. If the steady-state MLSS value is below (above) the target value then the plant is said to be operating in a state of negative (positive) excess sludge production. The transitional case when the

steady-state MLSS value is equal to the target value corresponds to zero excess sludge production.

The first mathematical model that was used to investigate how the process variables associated with a sludge disintegration unit (SDU) effect the steady-state MLSS value was developed and analysed by Yoon [20]. In Yoon's model the sludge disintegration unit is not modelled per se. Instead sludge disintegration terms are added to a conventional activated sludge model. These terms assume that the disintegrator unit destroys the biochemical activity of the sludge, converting a fraction, α , directly into usable substrate and the remainder, $(1 - \alpha)$, into organic particulates. This model forms the basis of all subsequent work in the area.

3. MICRO-POLLUTANTS

Wastewaters originating from the municipal sector contain an array of xenobiotic micropollutants. Common micropollutants include hormones, metals, pesticides, pharmaceutical compounds, polycyclic aromatic hydrocarbons (PAH), surfactants, and volatile organic compounds. Many of these products are characterised as pharmaceutical and personal care products (PPCPs).

Micropollutants leaving in the effluent stream of a wastewater treatment plant (WWTP), or entrapped in sludge that is removed from the WWTP, may have an adverse ecotoxic impact on the environment, particularly on aquatic ecosystems. Organic micropollutants (OMPs) have been detected downstream of WWTPs at concentrations in the range of ng/L to $\mu\text{g/L}$. OMPs have been detected in groundwaters, lakes, rivers and sediments. It is unsurprising then that they are detected in drinking waters. This has lead to legislation in Europe mandating that industry and states reduce their release.

Municipal WWTPs have been designed to remove biodegradable organic carbon residues. They have not been specifically designed for removing micropollutants. Consequently most of these compounds are only partially removed. However, WWTPs are the first line of defense (perhaps the only non-legislative line of defense?) against the environmental risk posed by micropollutants. There is therefore a growing scientific interest in investigating how effective WWTPs are in removing micropollutants and whether it is possible to optimise their removal without adversely effecting the effectiveness of WWTPs in removing macro-pollutants.

In WWTPs the main mechanisms by which micropollutants are removed include: biodegradation, cometabolism (the ability of microorganisms to degrade non-growth substrates in the presence of growth substrates [3]), sorption to sludge and volatilisation. These four mechanisms do not necessarily apply to all contaminants. For example, heavy metals are only removed by sorption and only volatile organic compounds are removed by mass transfer into the gas-phase. Additional mechanisms may apply to some contaminants. For example, heavy metals can be removed by precipitation.

Identifying the relative importance of these mechanisms for emerging new micropollutants is a major challenge and provide a major application of mathematical models. For example, understanding the relative importance of the main removal mechanisms

can lead to improved depletion of micropollutants in conventional WWTPs, reducing their environmental impact. Thus accurate and well developed mathematical models can help to optimise the removal of micropollutants from WWTPs without the need for significant plant upgrades. However, there is currently little agreement in the modelling literature as to how these processes should be modelled [18].

4. MATHEMATICAL MODELS

Although the activated sludge process was brought to the attention of engineers and scientists in 1914 (to be exact, on the 3rd April 1914) the first mathematical models for the process were not developed until almost 55 years latter, in the late 1960s and early 1970s [10, 11, 17].

These early models built upon a pioneering study in the field of microbiology [8]. In microbiology it is straightforward to design an experiment in which one micro-organisms grows through the consumption of one limiting substrate, all other substrates required for growth being in excess. Similarly the early models for the activated sludge process assumed that there is one limiting substrate, one limiting microorganism and one rate-limiting biochemical reaction. Although these are all valid assumptions in the microbiology context, there is no reason to believe that they are true for the activated sludge process: a typical wastewater contains many types of substrates and a typical aerated reactor contains many types of micro-organisms. However, the unreasonable effectiveness of mathematics in the natural sciences once again rears its head!

More detailed models have subsequently been devised. At one end this involves extensions of the basic model that remain analytically tractable. An important extension in this direction is due to Chung and Neethling [2] who enlarged the microbiology of the basic model in two ways. Firstly, they introduced a slowly biodegradable substrate component which is hydrolysed to produce small soluble organic materials. (These are the limiting substrate of the basic model). Secondly, they allowed a fraction of the dead biomass to be recycled back into the soluble substrate pool.

At the other end models have been developed which include sufficiently detailed microbiology that they are no longer amenable to analysis, an example of such models is the activated sludge models developed by the IWA [7, 12, 16]. Of these the activated sludge model number 1 (ASM1) [6] is the most well known. This has become an internationally accepted standard for activated sludge modeling, particularly of WWTPs.

The ASM1 model includes eight processes that are fundamental to the activated sludge process. These are: aerobic and anoxic growth of heterotrophic biomass, death of heterotrophic biomass, aerobic growth of autotrophic biomass, decay of autotrophic biomass, ammonification of soluble organic nitrogen and hydrolysis of both entrapped particulate organic matter and entrapped organic nitrogen. Together these processes describe nitrogen and chemical oxygen demand within suspended-growth treatment processes, including mechanisms for nitrification and denitrification.

Through its inclusion of the eight fundamental processes the model has been found to give a good description what happening in the activated sludge process *provided* that

the wastewater has been characterised and the model calibrated. Wastewater characterisation requires the determination of 12 parameters. Model calibration involves determining two physical parameters (associated with oxygen) and 19 parameters associated with microbial processes. Although some of the microbial parameters may be assumed to be relatively constant between different WWTPs, characterisation and calibration remain a non-trivial process. Finally, the wastewater must be of domestic or municipal, but not industrial, in origin.

Recent developments in the mathematical modeling of the activated sludge process are reviewed in [5, 13]. However, the ‘basic model’ and its extensions remains an attractive modelling approach for many exploratory investigations because such models are easy to calibrate.

5. SCOPE OF PRESENTATION

This presentation illustrates the use of the basic model and the two-step model, due to Chung and Neethling [2], to model: the activated sludge process, the problem of having too much sludge and the removal of micropollutants. An introduction will be provided to the ASM-1 model.

REFERENCES

- [1] A.P. Canales and J.L. Poles. Decreased sludge production strategy for domestic wastewater treatment. *Water Science and Technology*, 30(8):97–106, 1994.
- [2] Y-C. Chung and J.B. Neethling. Viability of anaerobic digester sludge. *Journal of Environmental Engineering*, 116(2):330–342, 1990.
- [3] C.S. Criddle. The kinetics of cometabolism. *Biotechnology and Bioengineering*, 41:1048–1056, 1993.
- [4] E. Egemen, J. Corpening, and N. Nirmalakhandan. Evaluation of an ozonation system for reduced waste sludge generation. *Water Science & Technology*, 44(2–3):445–52, 2001.
- [5] H. Hauduc, L. Rieger, A. Oehmen, M.C.M. van Loosdrecht, Y. Comeau, A. Heduit, P.A. Vanrolleghem, and S. Gillot. Critical review of activated sludge modeling: State of process knowledge, modeling concepts, and limitations. *Biotechnology and Bioengineering*, 110:24–46, 2013.
- [6] M. Henze, C.P.L. Grady Jr, W. Gujer, G.V.R. Marais, and T. Matsuo. A general model for single-sludge wastewater treatment systems. *Water Research*, 21(5):505–515, 1987.
- [7] M. Henze, W. Gujer, T. Mino, and van Loosdrecht. M. *Activated Sludge Models ASM1, ASM2, ASM2d and ASM3*. IWA Publishing., London, first edition, 2000.
- [8] D. Herbert, R. Elsworth, and R.C. Telling. The continuous culture of bacteria: a theoretical and experimental study. *Journal of General Microbiology*, 14:601–622, 1956.
- [9] B. Kent. Special treatment: Australia’s pioneering wastewater plant. Chemistry in Australia December 2014 – January 2015. Pages 24–25.
- [10] A.W. Lawrence and P.L. McCarty. Unified basis for biological treatment design and operation. *Journal of the Sanitary Engineering Division — ASCE*, 96(SA3):757–778, 1970.
- [11] A.W. Lawrence. Application of process kinetics to design of anaerobic processes. In F.G. Pohland, editor, *Anaerobic Biological Treatment Processes*, volume 105 of *Advances in Chemistry Series*, pages 163–189. American Chemical Society, Washington, D.C., 1971.
- [12] J. Makinia. *Mathematical Modelling and Computer Simulation of Activated Sludge Systems*. IWA Publishing, London, first edition, 2010.
- [13] C.J. Moretti, D. Das, B.T. Kistner, H. Gullicks, and Y-T Hung. Activated sludge and other aerobic suspended culture processes. *Water*, 3:806–818, 2011.
- [14] O. Nowak. Optimizing the use of sludge treatment facilities at municipal WWTPs. *Journal of Environmental Science and Health Part A — Toxic/Hazardous Substances & Environmental Engineering*, 41(9):1807–1817, 2006.

- [15] Y-K. Oh, K-R. Lee, K-B. Ko, and I-T Yeom. Effects of chemical sludge disintegration on the performance of wastewater treatment by membrane bioreactor. *Water Research*, 41:2665–2671, 2007.
- [16] D. Orhon, F.G. Babuna, and O. Karahan. *Industrial Wastewater Treatment by Industrial Sludge*. IWA Publishing, London, first edition, 2009.
- [17] E.A. Pearson. Kinetics of biological treatment. In E.F. Gloyna and W.W. Eckenfelder, editors, *Advances in water quality improvement*, pages 381–394. University of Texas Press, Austin, 1968.
- [18] M. Pomiès, J-M. Choubert, C. Wisniewski, and M. Coquery. Modelling of micropollutant removal in biological wastewater treatments: A review. *Science of the Total Environment*, 443:733–748, 2013.
- [19] Y. Wei, R.T. Van Houten, A.R. Borger, D.H. Eikelboom, and Y. Fan. Minimization of excess sludge production for biological wastewater treatment. *Water Research*, 37:4453–4467, 2003.
- [20] S-H. Yoon. Important operational parameters of membrane bioreactor-sludge disintegration (MBR-SD) system for zero excess sludge production. *Water Research*, 37:1921–1931, 2003.

Electrokinetic behaviour of concentrated colloidal suspensions

Bronwyn Hajek

Phenomics and Bioinformatics Research Centre,
School of Information Technology and Mathematical Sciences,
University of South Australia, Australia
(joint work with SJ Miklavcic, LR White)

Summary:

Electrokinetic techniques can be used to gather specific information about concentrated dispersions such as electronic inks, mineral processing slurries, pharmaceutical products and biological fluids (eg blood). But, like most experimental techniques, intermediate quantities are measured, and consequently the method relies explicitly on theoretical modelling to extract the quantities of experimental interest. This talk will outline the application of a self-consistent cell-model theory of electrokinetics to the problem of determining the dielectric response of a dense suspension of spherical colloidal particles [1]. The numerical predictions from the model will also be compared with published experimental results, with the model showing good agreement for the two measureable quantities [2]. The high frequency behaviour of the system is also analysed using matched asymptotic techniques. This produces simple expressions for the limiting forms of the measureable quantities. The expression for the dynamic mobility is valid in the megahertz range, making it useful in a laboratory situation [3].

The dynamic mobility and complex conductivity of a system are quantities that measure the dynamic response of a concentrated suspension of charged particles to an applied oscillating electric field. The response of the system is dependent upon properties such as the mean particle size, surface potential and surface charge. As such, measurement of the dielectric response provides a technique for determining these properties. Moreover, the dielectric response of the system is frequency dependent, and so this provides a useful means of monitoring and analysing particle interactions.

In the late 1980's, O'Brien developed a theoretical model which describes the behaviour of the electrokinetic response of a system to an applied oscillatory electric field of volume average $\langle \mathbf{E}(t) \rangle = \langle \mathbf{E} \rangle e^{-i\omega t}$ [4, 5, 6]. The model is based on the Navier-Stokes equations of hydrodynamics and the Poisson equation for the electric potential, and also includes ion conservation equations and ion transport equations. The electrolyte ion number densities, n_j , charge density, ρ_{ch} , electrochemical potentials, μ_j , drift velocities, \mathbf{v}_j , ($j = 1, 2, \dots, N$), the hydrodynamic flow field, \mathbf{u} , pressure, p , and electrostatic

potential, Ψ , are described by the following fundamental equations:

$$\begin{aligned}
\nabla^2 \Psi(\mathbf{r}, t) &= -\frac{1}{\varepsilon_s \varepsilon_0} \rho_{ch}(\mathbf{r}, t) \\
\rho_s \frac{\partial \mathbf{u}}{\partial t}(\mathbf{r}, t) &= -\nabla p(\mathbf{r}, t) - \rho_{ch}(\mathbf{r}, t) \nabla \Psi(\mathbf{r}, t) + \eta_s \nabla^2 \mathbf{u}(\mathbf{r}, t) \\
\nabla \cdot \mathbf{u}(\mathbf{r}, t) &= 0 \\
\mathbf{v}_j(\mathbf{r}, t) &= \mathbf{u}(\mathbf{r}, t) - \frac{1}{\lambda_j} \nabla \mu_j(\mathbf{r}, t) \\
\frac{\partial n_j}{\partial t}(\mathbf{r}, t) + \nabla \cdot [n_j(\mathbf{r}, t) \mathbf{v}_j(\mathbf{r}, t)] &= 0 \\
\mu_j(\mathbf{r}, t) &= -z_j e \Phi_j(\mathbf{r}, t) = \mu_j^\infty + z_j e \Psi(\mathbf{r}, t) + k_B T \ln[n_j(\mathbf{r}, t)]
\end{aligned}$$

with charge density

$$\rho_{ch}(\mathbf{r}, t) = \sum_{j=1}^N z_j e n_j(\mathbf{r}, t).$$

Here, e , ε_s , ε_0 , ρ_s , η_s , z_j , λ_j , k_B , and T are the electron charge, the relative fluid dielectric permittivity, vacuum permittivity, fluid mass density, fluid viscosity, valency and ionic drag coefficients of the j^{th} ion type, and the Boltzmann constant and temperature, respectively. The ion densities, n_j^∞ , are those of the reservoir. The drag coefficient, λ_j is related to the ionic limiting conductance, Λ_j^∞ , by

$$\lambda_j = \frac{N_A e^2 |z_j|}{\Lambda_j^\infty},$$

where N_A is Avogadro's number. The electrochemical potential functions $\Phi_j(\mathbf{r}, t)$ represent the deviations of the local ion densities from their (equilibrium) Poisson-Boltzmann expressions in terms of the local electrostatic potential $\Psi(\mathbf{r}, t)$. The Debye parameter is given by

$$\kappa^2 = \sum_{j=1}^N \frac{e^2 z_j^2 n_j^\infty}{\varepsilon_s \varepsilon_0 k_B T}.$$

For a more detailed explanation of these equations see [7].

These equations can be simplified in two ways. First, we assume that, under the influence of the oscillating field, the deviation of the field variables from their equilibrium values is sufficiently weak that a first order perturbation in the electric field strength is sufficient. As a result, the first order contributions can be expressed as a linear response. Second, we use symmetry arguments to remove the angular dependence of the problem so that all field variables are dependent on the radius from a (representative) particle centre only. Following these two simplifications, the field variables can be written as

$$\Xi(\mathbf{r}, t) = \Xi^{(0)}(r) + \Xi^{(1)}(r) e^{-\omega t} + O(\langle \mathbf{E}(t) \rangle^2),$$

where Ξ represents any of the field variables, Φ_j , Ψ , \mathbf{u} , ρ_{ch} , μ_j , n_j , and p . Simplification of the governing equations follows.

We require a number of boundary conditions to solve the model. At the slipping plane of the particle surface, we require that the electrostatic potential is equal to the zeta potential of the particle; we apply Neumann boundary conditions to the electrochemical potential; we require a stick boundary condition with regards to the flow; and we specify that ions cannot penetrate the particle surface.

This model was originally applied to the case of a dilute suspension and in that case, the suspension is approximated by an isolated particle so that the conditions in the far field may be used as the remaining boundary conditions for the system. For example, the fluid velocity far from the particle is considered zero and the electrostatic potential is equal to the applied potential [8].

In a concentrated suspension, each particle cannot be considered as isolated and the far field conditions can no longer be applied. In the concentrated case, the double layers of neighbouring particles may overlap, and the long range perturbation fields and the induced dipole fields will certainly overlap. In order to take account of the concentrated nature of the suspension, a self-consistent cell model was proposed [1, 7, 9]. The cell model theory reduces the problem to solving the equations within a geometric spherical cell that surrounds an individual (representative) charged particle. This enables us to generate a natural set of boundary conditions to close the model system of equations. For a suspension of particle volume fraction ϕ , an ensemble averaging over all particle positions relative to a chosen particle gives rise to a spherical cell of radius

$$b = a\phi^{-1/3},$$

so that the ratio of particle to fluid volume in the cell is the same as the particle volume fraction of the suspension. The model equations can then be solved within this one representative symmetry preserving, concentric cell with appropriate boundary conditions applied on the boundary of the cell, together with the usual boundary conditions at the particle slipping plane. The relevant cell boundary conditions can be derived from volume averaged global constraints on the physical quantities as follows: the whole system is electrically neutral, therefore each cell must also be; there must be no net flow of ions; and there must be no pressure gradient. A volume averaged momentum balance on the suspension is used to close the system [6], and numerical solution is performed using the COLSYS collocation package [10] in Fortran.

After solving the governing equations, we can calculate the quantities of experimental interest. First, the complex conductivity, K^* , represents the constant of proportionality between the measured current and the applied electric field,

$$\langle \mathbf{i} \rangle = K^* \langle \mathbf{E} \rangle,$$

where

$$K^*(\omega) = K_{\text{sol}}^*(\omega) + \Delta K^*(\omega)$$

contains a contribution from the bulk electrolyte, K_{sol}^* , and the charged particle dispersion and its associated electrical double layers, ΔK^* . It is this deviation from the bulk value that is of predominant interest. The real part of this deviation is the conductivity increment, while the imaginary part is the dielectric permittivity increment, $\Delta\epsilon(\omega)$,

$$\Delta K^*(\omega) = \text{Re}(\Delta K^*(\omega)) - i\omega\epsilon_0\Delta\epsilon(\omega).$$

The second quantity of experimental interest is the dynamic electrophoretic mobility, μ , which is given by

$$\mathbf{U} = \mu\mathbf{E},$$

where a particle in the presence of the applied electric field $\mathbf{E}e^{-i\omega t}$ oscillates about its equilibrium position with velocity $\mathbf{U}e^{-i\omega t}$.

To our knowledge, the cell model described herein provides the best way of accounting for the electrical double layer interactions in a dense suspension of colloidal particles. As described above, there are two quantities of experimental interest – of

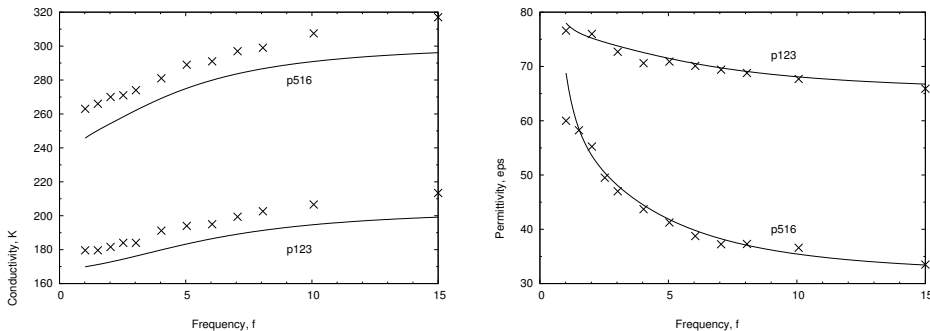


FIGURE 1. (a) Conductivity and (b) Permittivity of a polystyrene latex suspension at two different volume fractions. Crosses represent the experimental results (from [11]) and the solid lines show theoretical results using the present theory with $\zeta = -162\text{mV}$. Spherical particles, $a = 253\text{nm}$ in a KCl solution ($10^{-3}M$) at $T = 25^\circ\text{C}$.

these two, the dielectric response measurement provides a more sensitive test for the accuracy of the model. Figures 1(a)-(b) show the results of a comparison between the cell model calculations and the published experimental results of Midmore et al. [11] for the conductivity and the permittivity (reproduced from [2]). In this comparison, the only parameter that can be freely adjusted is the ζ -potential. The model shows good agreement with the experimental results, simultaneously for both quantities (conductivity and permittivity) and for two different volume fractions. The ζ -potential used for the model calculations, $\zeta = -162\text{mV}$, is very close to the value as found by Midmore et al., $\zeta = -159.3\text{mV}$.

Theoretical calculations of the frequency dependent complex conductivity do not always compare well with experiment; there are two possible explanations for this. First, the discrepancy could result from the neglect of some of the physical characteristics such as surface conduction, a non-uniform charge layer, or polymeric drag, particularly in the case of particles with polymer coatings (so called “hairy” or “soft particles”). Second, it is also possible that electrode polarisation has not been properly taken into account in the impedance measurements. This second source of error can be apparent particularly at low frequencies.

Figure 1 shows that the cell model performs well, even at high volume fractions when particle-particle interaction through their electrical double layers is strong. However, at high volume fractions, the system of differential equations becomes difficult to solve, particularly at high frequencies when the equations become stiff. In order to quantify the accuracy of our calculations, we have used a matched asymptotic method to find closed form high-frequency approximations for the experimentally measurable quantities [3]. In addition to confirming the accuracy of our calculations at high frequency, these high-frequency formulas provide a more direct connection between the system parameters and the experimental quantities. In particular, the limiting form of the high frequency formula for the dielectric permittivity

$$\Delta\varepsilon = \frac{3(\varepsilon_p - \varepsilon_s)\phi}{2 + \phi + (1 - \phi)\frac{\varepsilon_p}{\varepsilon_s}},$$

where ε_p is the permittivity of the particle, is valid in the megahertz range and above and, as such, may be useful for direct and fast calculations in the laboratory.

REFERENCES

- [1] BH Bradshaw-Hajek, SJ Miklavcic, LR White, *Langmuir*, 2008, 24(9):4512-4522
- [2] BH Bradshaw-Hajek, SJ Miklavcic, LR White, *Langmuir*, 2009, 25(4):1961-1969
- [3] BH Bradshaw-Hajek, SJ Miklavcic, LR White, *Langmuir*, 2010, 26(3):1656-1665
- [4] RW O'Brien, *J. Colloid Interface Sci.*, 1986, 113(1), 81-93
- [5] RW O'Brien, *J. Fluid Mech.*, 1988, 190, 71-86
- [6] RW O'Brien, *J. Fluid Mech.*, 1990, 212, 81-93
- [7] S Ahualli, A Delgado, SJ Miklavcic, LR White, *Langmuir*, 2006, 22(16):7041-7051
- [8] CS Mangelsdorf, LR White, *J. Chem. Soc. Faraday Trans.*, 1992, 88(24), 3567-3581
- [9] S Ahualli, A Delgado, SJ Miklavcic, LR White, *J. Colloid Interface Sci.*, 2007, 309(2), 342-349
- [10] U Ascher, J Christiansen,, RD Russell, COLSYS, Netlib, <http://www.netlib.org>
- [11] BR Midmore, RJ Hunter, RW O'Brien, *J. Colloid Interface Sci.*, 1987, 120(1), 210-217

Modelling micro and nanostructured surfaces

Shaun Hendy

Te Pūnaha Matatini and Department of Physics, University of Auckland, Auckland,
New Zealand

The patterning of surfaces on the microscale, the nanoscale, or both, can be used to control the properties of material surfaces. For instance, a mildly hydrophobic planar surface can be made superhydrophobic with contact angles approaching 180° by roughening at the micro or nanoscale. Advances in so-called *top-down* lithographic techniques mean that surfaces can now be patterned with atomic precision, opening up many new possibilities for controlling surface properties. The most precise techniques are slow and expensive, however, making them difficult to apply over large areas in a manufacturing process.

In this talk I will consider two problems. The first problem considers the prediction of macroscopic material properties from knowledge of the micro or nanoscale patterning. The second concerns the development of cheap, effective methods for patterning using what are known as *bottom up* approaches such as molecular self-assembly, or techniques that use a combination of bottom-up and top-down methods.

The ability to predict macroscopic properties from microscopic material structure is a fundamental problem in materials science but one that is also of great practical significance if it allows for the design of surface patterns that lead to particular properties. We approach this problem by developing continuum approximations to the macroscopic performance in asymptotic limits where the macroscopic scale greatly exceeds that of the patterning [1, 2].

We apply this approach to investigate macroscopic flows over chemically micropatterned surfaces that vary in their wettability [1] and surfaces that are coated in chemically tethered polymer brushes [3]. Such surfaces occur in nature (e.g. the lotus leaf, which is patterned to allow facilitate the rolling of droplets that help clean the leaf's surface) and are of interest technologically (e.g. surfaces that have low drag). In the limits investigated we find that the resultant flows simply depend on the length of the patterning and the surface coverage only rather than the pattern itself. Simulations show that the approximations remain valid even in the limits of nanoscale patterning.

We also apply these methods to calculate the performance of nanostructured catalysts under diffusion-limited operated conditions [4]. In principle, the high surface area to volume ratio of nanostructured catalysts can offer dramatically superior activity by weight, which for precious metal catalysts is particularly important. We find that the effective macroscopic performance of a nanopatterned catalyst depends only on the length of the patterning and the surface coverage, but that diminishing returns can occur as the mean free path of reactant gas molecules approach the length scale of the patterning. However, in this case, when the mean free path of gaseous reactants exceeds the length scale of the surface patterning microscopic simulations show that the continuum approach underestimates performance.

We consider a number of bottom-up methods for fabricating such surfaces based on the idea of thin film dewetting. We first consider a surface coated in polymer brushes in

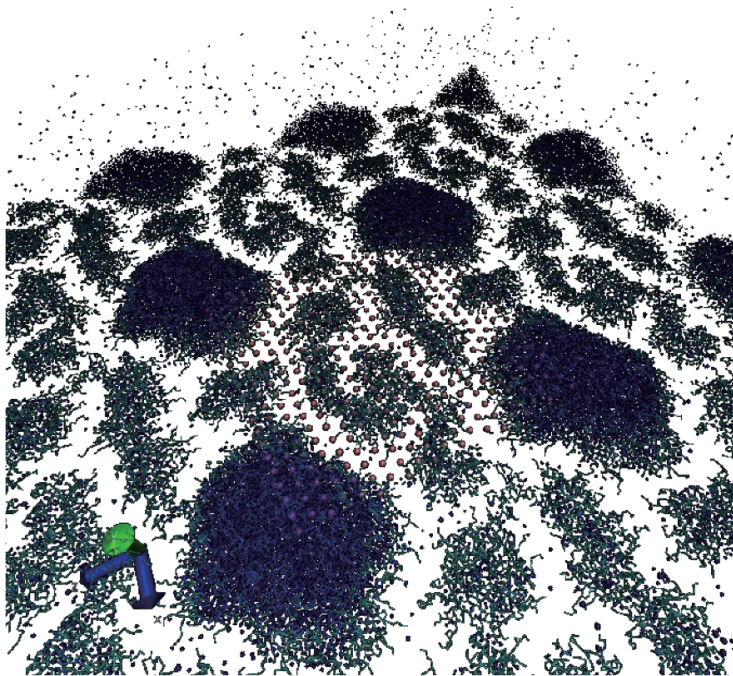


FIGURE 1. A snapshot of a molecular dynamics simulation of a forest of polymer brushes chemically tethered to a surface. The simulation shows the formation of patterned arrays of polymer micelles that form as the solvent evaporates from the surface during drying [5]. These micelles can be used to nucleate the growth of nanoparticles on the surface [6] resulting in ordered arrays of particles.

the presence of a solvent, and conduct coarse-grained simulations of the drying process. During drying we observe the formation of patterned arrays of micelles that form as the brushes collapse [5]. We show that these micelles can be used to nucleate the growth of nanoparticles on the surface in arrays that follow the patterning of the micelles [6].

Finally we use molecular dynamics simulations to study the dewetting of thin films on a nanoporous substrate as the substrate is heated [7]. We show that even if the film only partially wets the substrate, surface tension can drive the film into the pores during the dewetting process. This provides a method for filling nanoporous materials with nonwetting substances, something which is useful in the manufacture of polymer-based solar cells.

REFERENCES

- [1] Hendy, S. C.; Lund, N. J.; "Effective slip boundary conditions for flows over nanoscale chemical heterogeneities" *Physical Review E* **76** 66313 (2007)
- [2] Lund, N. J; Zhang, X. P.; Mahelona, K.; Hendy, S. C.; "Calculation of effective slip on rough chemically heterogeneous surfaces using a homogenization approach" *Physical Review E* **86** 46303 (2012)

- [3] Lee, T.; Hendy, S. C.; Neto, C.; "Interfacial Flow of Simple Liquids on Polymer Brushes: Effect of Solvent Quality and Grafting Density" *Macromolecules* **45** 6241-6252 (2012)
- [4] Rajabi, L.; Hendy, S. C.; "Effective rate constant for nanostructured heterogeneous catalysts" *Physical Chemistry Chemical Physics* **17** 30518-30524 (2015)
- [5] Lee, T.; Hendy, S. C; Neto, C.; "Tunable Nanopatterns via the Constrained Dewetting of Polymer Brushes" *Macromolecules* **46** 6326-6335 (2013)
- [6] Lee, T.; Hendy, S. C; Neto, C.; "Control of nanoparticle formation using the constrained dewetting of polymer brushes" *Nanoscale* **7** 2894-2899 (2015)
- [7] Schebarchov, D; Lefevre, B; Somerville, W. R. C; Hendy, S. C.; "Filling a nanoporous substrate by dewetting of thin films" *Nanoscale* **5** 1949-1954 (2013)

Spatial pattern of discrete and ultradiscrete Gray-Scott model

Keisuke Matsuya

Faculty of Engineering Department of Mathematical Engineering,
 Musashino University, Japan

(joint work with Mikio Murata)

1. INTRODUCTION

Discretization is a procedure to get difference equations with some parameters from given differential equations. The difference equations change to the differential equations with limits of the parameters. This procedure is often used when one computes differential equations numerically.

Ultradiscretization [1] is a limiting procedure transforming given difference equations into other difference equations which consist of addition, subtraction and maximum including cellular automata. In this procedure, a dependent variable u_n in a given equation is replaced by

$$(1) \quad u_n = \exp \left(\frac{U_n}{\varepsilon} \right),$$

where ε is a positive parameter. Then, we apply $\varepsilon \log$ to both sides of the equation and take the limit $\varepsilon \rightarrow +0$. Using identity

$$\lim_{\varepsilon \rightarrow +0} \varepsilon \log (e^{U/\varepsilon} + e^{V/\varepsilon}) = \max (U, V)$$

and exponential laws, we find that multiplication, division and addition for the original variables are replaced by addition, subtraction and maximum for the new ones, respectively. In this way, the original difference equation is approximated by a piecewise linear equation.

Gray-Scott model [2] is a variant of the auto catalytic model. Basically it considers the reactions

$$\begin{cases} U + 2V \rightarrow 3V, \\ V \rightarrow P, \end{cases}$$

in an open flow reactor where U is continuously supplied, and the product P removed. A mathematical model of the reactions above is the following reaction-diffusion system:

$$(2) \quad \begin{cases} \frac{\partial u}{\partial t} = \Delta u - uv^2 + a(1 - u), \\ \frac{\partial v}{\partial t} = D_v \Delta v + uv^2 - bv, \end{cases}$$

where $u := u(t, \vec{x})$, $v := v(t, \vec{x})$, $t \geq 0$, $\vec{x} \in \mathbb{R}^d$ and D_v , a and b are positive constants. Δ is d -dimensional Laplacian. The solutions of this system represent spatial patterns. Changing not only an initial condition but also parameters, various patterns are observed [3, 4, 5].

In this talk, the speaker proposes a discretization and an ultradiscretization of the Gray-Scott model. The ultradiscrete system is directly related to the elementary cellular automata, especially Rule 90 which gives a Sierpinski gasket pattern [6].

2. DISCRETE GRAY-SCOTT MODEL

Since it is more convenient to consider the ultradiscretization, we take the scaling $w := v + 1$ which changes (2) to

$$(3) \quad \begin{cases} \frac{\partial u}{\partial t} = \Delta u - u(w-1)^2 + a(1-u), \\ \frac{\partial w}{\partial t} = D_v \Delta w + u(w-1)^2 - b(w-1). \end{cases}$$

First we consider the discretization of following system of ordinary differential equations:

$$(4) \quad \begin{cases} \frac{du}{dt} = -u(w-1)^2 + a(1-u), \\ \frac{dw}{dt} = u(w-1)^2 - b(w-1), \end{cases}$$

where $u := u(t)$, $w := w(t)$. We consider the following system of difference equations:

$$(5) \quad \begin{cases} u_{n+1} = \frac{u_n + \delta(2u_n w_{n+1} + a)}{1 + \delta\{(w_{n+1})^2 + a + 1\}}, \\ w_{n+1} = \frac{w_n + \delta[u_n\{(w_n)^2 + 1\} + b]}{1 + \delta(2u_n + b)}, \end{cases}$$

where $n \in \mathbb{Z}_{\geq 0}$, $\delta > 0$. (5) is discretization of (4) and the method of discretization is same to that used in [6, 7]. Fixed points of (5) is same with (4) and stability of the fixed points of (5) is similar to those of (4) [6]. Using (5), we can construct a system of partial difference equations:

$$(6) \quad \begin{cases} w_{n+1}^{\vec{j}} = \frac{m_p(u_n^{\vec{j}}) + \delta(2m_p(u_n^{\vec{j}})w_{n+1}^{\vec{j}} + a)}{1 + \delta\{(w_{n+1}^{\vec{j}})^2 + a + 1\}}, \\ w_{n+1}^{\vec{j}} = \frac{m_q(w_n^{\vec{j}}) + \delta\{m_p(u_n^{\vec{j}})(m_q(w_n^{\vec{j}})^2 + 1) + b\}}{1 + \delta(2m_p(u_n^{\vec{j}}) + b)}, \end{cases}$$

where $n \in \mathbb{Z}_{\geq 0}$, $\vec{j} \in \mathbb{Z}^d$, $p, q \in \mathbb{N}$,

$$m_p(u_n^{\vec{j}}) := \sum_{k=1}^d \frac{u_n^{\vec{j}+p\vec{e}_k} + u_n^{\vec{j}-p\vec{e}_k}}{2d}, \quad m_q(w_n^{\vec{j}}) := \sum_{k=1}^d \frac{w_n^{\vec{j}+q\vec{e}_k} + w_n^{\vec{j}-q\vec{e}_k}}{2d}$$

and $\vec{e}_k \in \mathbb{Z}^d$ is a unit vector whose k th component is 1. Since (6) is equivalent to

$$\begin{cases} \frac{w_{n+1}^{\vec{j}} - w_n^{\vec{j}}}{\delta} = \sum_{k=1}^d \frac{u_n^{\vec{j}+p\vec{e}_k} - 2u_n^{\vec{j}} + u_n^{\vec{j}-p\vec{e}_k}}{(p\xi)^2} - m_p(u_n^{\vec{j}})(w_{n+1}^{\vec{j}} - 1)^2 \\ \quad + a(1 - m_p(u_n^{\vec{j}})) + o(\delta), \\ \frac{w_{n+1}^{\vec{j}} - w_n^{\vec{j}}}{\delta} = \frac{q^2}{p^2} \sum_{k=1}^d \frac{w_n^{\vec{j}+q\vec{e}_k} - 2w_n^{\vec{j}} + w_n^{\vec{j}-q\vec{e}_k}}{(q\xi)^2} + m_p(u_n^{\vec{j}})(m_q(w_n^{\vec{j}}) - 1)^2 \\ \quad - b(m_q(w_n^{\vec{j}}) - 1) + o(\delta), \end{cases}$$

where $\xi := \sqrt{2d\delta}/p$, if there exists smooth functions $u(t, \vec{x})$, $w(t, \vec{x})$ ($t \geq 0$, $\vec{x} \in \mathbb{R}^d$) that satisfy $u(\delta n, \xi \vec{j}) = u_n^{\vec{j}}$ and $w(\delta n, \xi \vec{j}) = w_n^{\vec{j}}$, we obtain (3) where $D_v = (q/p)^2$ with the limit $\delta \rightarrow 0$.

Now, let spatial dimension $d = 1$ and $p = 3$, $q = 1$, $\delta = 0.1$ and

$$u_0^j = \begin{cases} 1 - 0.3 \cos\left(\frac{\pi j}{50}\right) & |j| \leq 25 \\ 1 & |j| > 25 \end{cases}, \quad w_0^j = \begin{cases} 1 + 0.5 \cos\left(\frac{\pi j}{50}\right) & |j| \leq 25 \\ 1 & |j| > 25 \end{cases}.$$

If one plots the solutions of (6) with a periodic boundary condition, the following patterns are observed. The horizontal axis is for space variable j . The vertical axis is for time variable n . We get contour plots of the values for w_n^j .

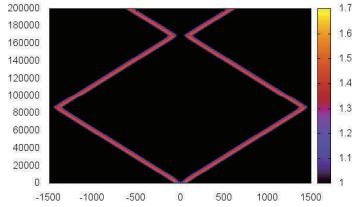


FIGURE 1. $a = 0.03$, $b = 0.10$

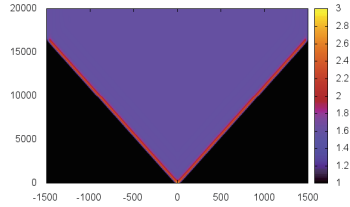


FIGURE 2. $a = 0.04$, $b = 0.06$

In Figure 1, a peak split into two peaks and two peaks move opposite side. We took a periodic boundary condition so that it is observed that two peaks pass each other. In Figure 2, a similar situation of Figure 1 is observed. Between two peaks, values of (u, w) converge to the stable equilibrium point $P_{d,+}$. Since we take periodic boundary conditions, two peaks collide at the boundary and vanish.

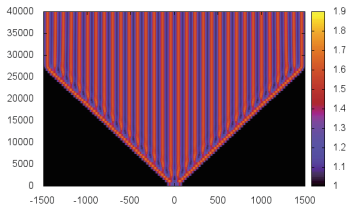


FIGURE 3. $a = 0.04$, $b = 0.09$

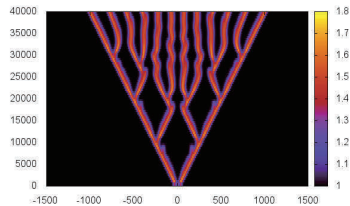


FIGURE 4. $a = 0.04$, $b = 0.11$

In Figure 3 and 4, a peak split into two peaks several times and a self-replicating pattern is observed.

3. ULTRADISCRETE GRAY-SCOTT MODEL

Let

$$u_n^{\vec{j}} = \exp\left(\frac{U_n^{\vec{j}}}{\varepsilon}\right), \quad w_n^{\vec{j}} = \exp\left(\frac{W_n^{\vec{j}}}{\varepsilon}\right),$$

$$\delta = \exp\left(\frac{D}{\varepsilon}\right), \quad a = \exp\left(\frac{A}{\varepsilon}\right), \quad b = \exp\left(\frac{B}{\varepsilon}\right)$$

and take the limit $\varepsilon \rightarrow +0$, then we have

$$(7) \quad \begin{cases} U_{n+1}^{\vec{j}} = \max[M_p(U_n^{\vec{j}}), D + \max[M_p(U_n^{\vec{j}}) + W_{n+1}^{\vec{j}}, A]] \\ \quad - \max[0, D + \max[2W_{n+1}^{\vec{j}}, A, 0]], \\ W_{n+1}^{\vec{j}} = \max[M_q(W_n^{\vec{j}}), D + \max[M_p(U_n^{\vec{j}}) + \max[2M_q(W_n^{\vec{j}}), 0], B]] \\ \quad - \max[0, D + \max[M_p(U_n^{\vec{j}}), B]], \end{cases}$$

where

$$M_p(U_n^{\vec{j}}) := \max_{k=1, \dots, d} [U_n^{\vec{j}+p\vec{e}_k}, U_n^{\vec{j}-p\vec{e}_k}],$$

$$M_q(W_n^{\vec{j}}) := \max_{k=1, \dots, d} [W_n^{\vec{j}+q\vec{e}_k}, W_n^{\vec{j}-q\vec{e}_k}].$$

Taking a limit $D \rightarrow \infty$ and assuming $W_n^{\vec{j}} \geq 0$, then (7) changes to

$$(8) \quad \begin{cases} U_{n+1}^{\vec{j}} = \max[M_p(U_n^{\vec{j}}) + W_{n+1}^{\vec{j}}, A] - \max[2W_{n+1}^{\vec{j}}, A], \\ W_{n+1}^{\vec{j}} = \max[M_p(U_n^{\vec{j}}) + 2M_q(W_n^{\vec{j}}), B] - \max[M_p(U_n^{\vec{j}}), B]. \end{cases}$$

Let spatial dimension $d = 1$ and initial data of (8) $-U_0^j \in \{0, 1\}$, $W_0^j \in \{0, 1\}$. Taking some conditions to parameters A and B , the solution of (8) becomes to a cellular automaton. There are five types of the conditions for A and B as follow:

Type I	Type II	Type III	Type IV	Type V
$A \leq -1$	$0 \leq A \leq 1$	$A \geq 2$	$A \leq -1$	$A \geq 0$
$B = 1$	$B = 1$	$B = 1$	$B \geq 2$	$B \geq 2$

Type I: The rule for $A \leq -1$, $B = 1$:

$$\begin{array}{c|c|c|c|c} -M_p(U_n^j), M_q(W_n^j) & 1, 1 & 1, 0 & 0, 1 & 0, 0 \\ \hline -U_{n+1}^j, W_{n+1}^j & 1, 0 & 1, 0 & 1, 1 & 0, 0 \end{array}$$

In this case, we can observe the patterns in Figure 5. Values of W_n^j is represent as

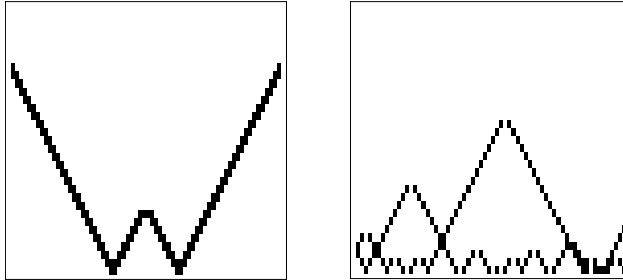


FIGURE 5. W_n^j with $A = -1$, $B = 1$ and $p = q = 1$.

follow: 0 (white) and 1 (black). The horizontal axis is for space variable j . The vertical axis is for time variable n . Time evolution started from two peaks in the left side and from several peaks in the right side. In Figure 5, every peaks split into two peaks and move opposite side. Two peaks vanish, when they collide.

Type II: The rule for $0 \leq A \leq 1, B = 1$:

$$\frac{-M_p(U_n^j), M_q(W_n^j)}{-U_{n+1}^j, W_{n+1}^j} \begin{array}{c|c|c|c} 1, 1 & 1, 0 & 0, 1 & 0, 0 \\ \hline 0, 0 & 0, 0 & 1, 1 & 0, 0 \end{array}$$

In this case, $U_{n+1}^j = -W_{n+1}^j$ and we can observe the patterns in Figure 6 and 7. Since this relation is held, W_n^j satisfies a single equation. Moreover, taking $p = q = 1$, the equation is same as ECA rule 90, which is well known for fractal design:

$$\frac{W_n^{j-1} W_n^j W_n^{j+1}}{W_{n+1}^j} \begin{array}{c|c|c|c|c|c|c|c|c} 111 & 110 & 101 & 100 & 011 & 010 & 001 & 000 \\ \hline 0 & 1 & 0 & 1 & 1 & 0 & 1 & 0 \end{array}$$

In Figure 6 and 7, time evolution started from two peaks in the left sides and from

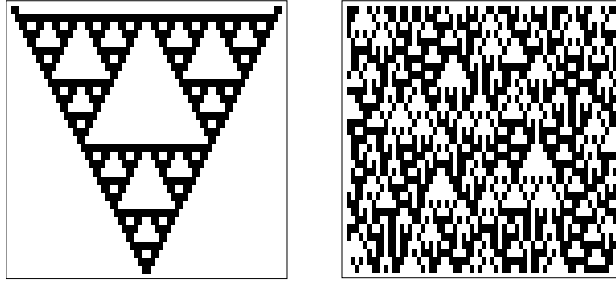


FIGURE 6. W_n^j with $A = 0, B = 1$ and $p = q = 1$.

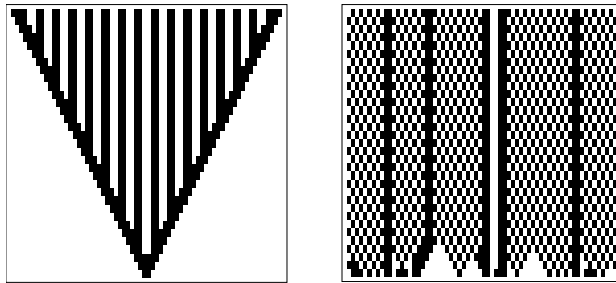


FIGURE 7. W_n^j with $A = 0, B = 1, p = 2$ and $q = 1$

several peaks in the right sides. In the left side of Figure 6, Sierpinski gasket pattern is observed.

Type III: The rule for $A \geq 2, B = 1$:

$$\frac{-M_p(U_n^j), M_q(W_n^j)}{-U_{n+1}^j, W_{n+1}^j} \begin{array}{c|c|c|c} 1, 1 & 1, 0 & 0, 1 & 0, 0 \\ \hline 0, 0 & 0, 0 & 0, 1 & 0, 0 \end{array}$$

In this case, $U_{n+1}^j = 0$ so that W_n^j satisfies $W_{n+1}^j = M_q(W_n^j)$.

Type IV: The rule of $A \leq -1, B \geq 2$:

$$\frac{-M_p(U_n^j), M_q(W_n^j)}{-U_{n+1}^j, W_{n+1}^j} \begin{array}{c|c|c|c|c} 1, 1 & 1, 0 & 0, 1 & 0, 0 \\ \hline 1, 0 & 1, 0 & 0, 0 & 0, 0 \end{array}$$

In this case, $W_{n+1}^j = 0$ so that U_n^j satisfies $U_{n+1}^j = M_p(U_n^j)$.

Type V: The rule of $A \geq 0, B \geq 2$:

$$\frac{-M_p(U_n^j), M_q(W_n^j)}{-U_{n+1}^j, W_{n+1}^j} \begin{array}{c|c|c|c|c} 1, 1 & 1, 0 & 0, 1 & 0, 0 \\ \hline 0, 0 & 0, 0 & 0, 0 & 0, 0 \end{array}$$

In this case, $U_{n+1}^j = W_{n+1}^j = 0$ so that U and W vanish immediately.

4. CONCLUDING REMARKS

In this abstract, we proposed and investigated discrete and ultradiscrete Gray-Scott model, which is a two component reaction diffusion system. We found that solutions of each equation reveal various spatial patterns. Moreover, there are solutions of the discrete equation and the ultradiscrete equation whose solutions give similar spatial patterns. The ultradiscrete Gray-Scott model has a solution which is an elementary cellular automaton and which reveals Sierpinski gasket. The method of discretization and ultradiscretization of Gray-Scott in this paper is one method to relate reaction diffusion systems to cellular automata. Clarifying the relation between solutions of discrete Gray-Scott model and those of ultradiscrete Gray-Scott model is a future work for the authors.

ACKNOWLEDGMENTS

The authors are deeply grateful to Prof. Tetsuji Tokihiro who provided helpful comments and suggestions. This work was supported by JSPS KAKENHI Grant Number 23740125.

REFERENCES

- [1] T. Tokihiro, D. Takahashi, J. Matsukidaira and J. Satsuma, From soliton equations to integrable cellular automata through a limiting procedure, Phys. Rev. Lett. 29 (1996), 3247–3250
- [2] P. Gray and S. K. Scott, Sustained oscillations and other exotic patterns of behaviour in isothermal reactions, J. Phys. Chem. 89 (1985), 22–32
- [3] W. Mazin, K. E. Rasmussen, E. Mosekilde, P. Borckmans and G. Dewel, Pattern formation in the bistable Gray-Scott model, Math. Comput. Simul. 40 (1996), 371–396
- [4] Y. Nishiura and D. Ueyama, A skeleton structure of self-replicating dynamics, Physica D 130 (1999), 73–104
- [5] Y. Nishiura and D. Ueyama, Spatio-temporal chaos for the Gray-Scott model, Physica D 150 (2001), 137–162
- [6] K. Matsuya and M. Murata, Spatial pattern of discrete and ultradiscrete Gray-Scott model, Discrete Contin. Dyn. Syst. Ser. B 20 (2015), 173–187
- [7] M. Murata, Tropical discretization: ultradiscrete Fisher-KPP equation and ultradiscrete Allen-Cahn equation, J. Difference Equ. Appl. 19 (2013), 1008–1021

Finite element analysis of viscoelastic flow problems, with application incorporating the Oldroyd-B model

TAGAMI Daisuke

Institute of Mathematics for Industry, Kyushu University, JAPAN

Viscoelastic flow is an important physical phenomena both from both theoretical and practical points of view. Blood flows in the human body and plastic flows during injection molding are typical examples of viscoelastic flow; for more examples and details, see Larson [2], Öttinger [4], and their references. Therefore, we encounter many research articles on the numerical analysis and simulation of viscoelastic flows; see, for example, Bonito–Clement–Picasso [1], Owens–Phillips [5], and their references.

In order to enhance the mathematical justification of numerical methods for viscoelastic flows, we consider the Oldroyd-B model of viscoelastic flow: Let $\Omega (\subset \mathbb{R}^d, d = 2, 3)$ be a bounded domain with the \mathcal{C}^2 -class boundary Γ . Let $T (> 0)$ be a time, $I := (0, T)$ a time interval. Then, find the velocity $u : \Omega \times I \rightarrow \mathbb{R}^d$, the pressure $p : \Omega \times I \rightarrow \mathbb{R}$, and the non-Newtonian stress $\sigma_P : \Omega \times I \rightarrow \mathbb{R}_{\text{sym}}^{d \times d}$ such that

$$\begin{aligned} \rho(\partial_t u + (u \cdot \nabla)u) - 2\eta_s \nabla \cdot D(u) + \nabla p - \nabla \cdot \sigma_P &= f, & \text{in } \Omega \times I, \\ \nabla \cdot u &= 0, & \text{in } \Omega \times I, \\ \sigma_P + \lambda(\partial_t \sigma_P + (u \cdot \nabla)\sigma_P - (\nabla u)\sigma_P - \sigma_P(\nabla u)^T) - 2\eta_p D(u) &= 0, & \text{in } \Omega \times I, \\ u &= 0 & \text{on } \Gamma \times I, \\ u &= u^0, \quad \sigma_P = \sigma_P^0 & \text{in } \Omega, \text{ at } t = 0, \end{aligned}$$

where $f : \Omega \times I \rightarrow \mathbb{R}^d$ denotes an external force, $u^0 : \Omega \rightarrow \mathbb{R}^d$ an initial velocity, $\sigma_P^0 : \Omega \rightarrow \mathbb{R}_{\text{sym}}^{d \times d}$ an initial non-Newtonian stress; $\rho (> 0)$ the density, η_s the solvent viscosity, $\eta_p (> 0)$ the polymer viscosity, and $\lambda (> 0)$ the relaxation time.

First, we establish error estimates of a pressure-stablized finite element method for a three-field Stokes model, which neglects the nonlinear components appearing in the Oldroyd-B model. Under standard assumptions for the finite element analysis of flow problems, we obtain error estimates of finite element solutions (u_h, p_h, σ_{Ph}) corresponding to (u, p, σ_P) as follows: there exists a positive constant c such that

$$\begin{aligned} \|u - u_h\|_{\ell^\infty((L^2(\Omega))^d)} &, \quad \|u - u_h\|_{\ell^2((H^1(\Omega))^d)} \leq c(\Delta t + h), \\ \|\sigma_P - \sigma_{Ph}\|_{\ell^\infty((L^2(\Omega))^{d \times d})} &\leq c(\Delta t + h), \\ \|p - p_h\|_{\ell^\infty(L^2(\Omega))} &\leq c\Delta t^{-1/2}(\Delta t + h). \end{aligned}$$

Here, Δt and h denote discretized parameters in time and in space, respectively; for the total step number in time N_T , a Banach space X , and an X -valued sequence $v = \{v^{(k)} \in X; k = 0, 1, \dots, N_T\}$, $\|\cdot\|_{\ell^\infty(X)}$ and $\|\cdot\|_{\ell^2(X)}$ denote

$$\begin{aligned} \|v\|_{\ell^\infty(X)} &:= \max\{\|v^{(k)}\|_X; k = 0, 1, \dots, N_T\}, \\ \|v\|_{\ell^2(X)} &:= \left(\Delta t \sum_{k=0}^{N_T} \|v^{(k)}\|_X^2 \right)^{1/2}, \end{aligned}$$

respectively.

Second, we consider an approximation of the upper-convected derivative along the motion of fluid particles to avoid difficulties of high Deborah number problems.

Finally, we show some numerical examples of contraction flows, and compare numerical results with experimental ones. Figs. 1–2 show some examples of the comparisons; the stream lines of the 4 to 1 contraction flow among the Stokes and the Oldroyd-B models.

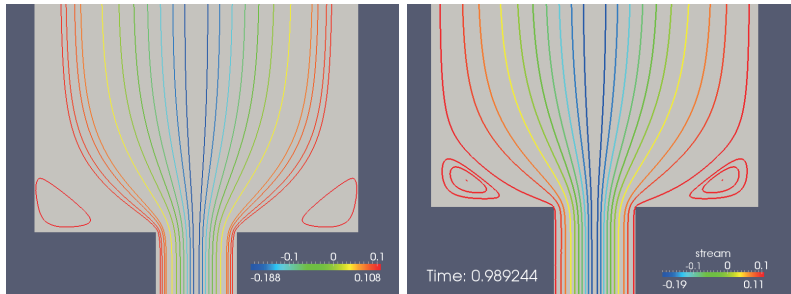


FIG. 1. Stream lines of the 4 to 1 contraction flow (Left: the Stokes model; Right: the Oldroyd-B model)

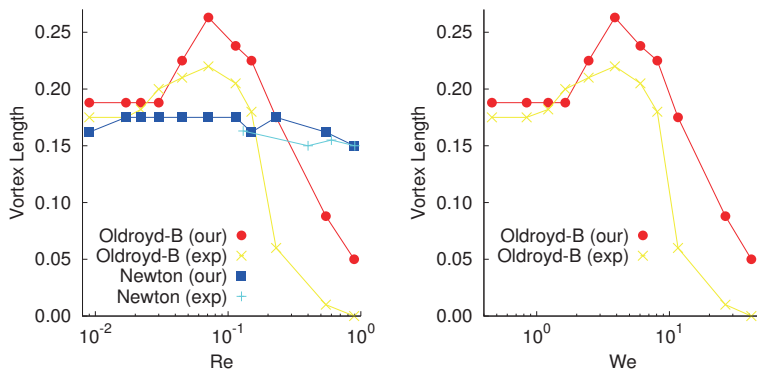


FIG. 2. Comparison of vortex length of the 4 to 1 contraction flow (Left: with respect to the Reynolds number; Right: with respect to the Weissenberg number)

REFERENCES

- [1] BONITO, A., CLÉMENT, P., AND PICASSO, M.: *Viscoelastic flows with complex free surfaces: numerical analysis and simulation*, In Ciarlet, P.-H. (Ed.), Numerical Methods for Non-Newtonian Fluids, Vol.16, 2011, Amsterdam, Elsevier/North Holland.
- [2] LARSON, R.G.: *The Structure and Rheology of Complex Fluids*, Oxford University Press, 1999.
- [3] OLDROYD, J.G.: *On the Formulation of Rheological Equation of State*, Proc. Poy. Soc, **A200** (1950), pp.523–541.
- [4] ÖTTINGER, H.-C.: *Stochastic processes in polymeric fluids*, Springer-Verlag, 1996.
- [5] OWENS, R.G. AND PHILLIPS, T.N.: *Computational Rheology*, Imperial College Press, 2005.

Continuum modelling of grain boundary evolution on metal surfaces.

Philip Broadbridge

Institute of Mathematics for Industry, Kyushu University — Australia Branch,
La Trobe University, Bundoora VIC 3086, Australia

1. FORMATION OF GRAIN BOUNDARIES

As a liquid solidifies, crystals grow from separate nucleation sites, each with a random orientation of crystal planes. Eventually these crystals grow and meet at a grain boundary. These can be observed as shallow grooves on metal surfaces. The density of grain boundaries affects the appearance of metal surfaces, as well as the strength of the solid. For example, grain boundaries are used to create a spangled appearance on the surface of some metal sheet products. Through an electron microscope, grain boundaries beginning at the nanoscale, can be observed to grow in thickness and depth. They may be several millimetre in length between triple grain junctions, in comparison to a thickness of a few micron. Therefore grain boundary evolution may be described as a two-dimensional cross section profile, $y(x, t)$ in Cartesian coordinates. From Herring (1951), the surface energy per particle is

$$(1) \quad \Phi(\phi) = \Omega[\gamma_s''(\phi) + \gamma_s(\phi)]\kappa,$$

where Ω is the mean particle volume, γ_s is surface tension, κ is curvature and $\phi = \arctan(y_x)$ is the orientation angle of the surface. Mullins' 1957 theory of surface diffusion applies the Nernst–Einstein relation to express material area flux due to surface diffusion,

$$J = -\nu\Omega \frac{D_s(\phi)}{kT} \frac{\partial \Phi}{\partial s},$$

where ν is areal density of particles, D_s is surface mobility, kT is absolute temperature multiplied by Boltzmann's constant, and s is arclength. For an ideal isotropic material, D_s and Φ are independent of surface orientation. In that case, the equation of continuity for conservation of volume, results in the surface diffusion equation

$$(2) \quad y_t = -B \partial_x \left\{ (1 + y_x^2)^{-1/2} \partial_x \frac{y_{xx}}{(1 + y_x^2)^{3/2}} \right\} ; B > 0 \text{ (constant)}$$

$$(3) \quad \begin{aligned} \text{or } \theta_t &= -B \partial_x^2 \left\{ f(\theta) \partial_x \left[\theta_x f(\theta) \sqrt{[f'(\theta)]^2 + [\theta f'(\theta) + f(\theta)]^2} \right] \right\} \\ &= -B \partial_x^2 \left\{ (1 + \theta^2)^{-1/2} \partial_x \left[(1 + \theta^2)^{-3/2} \theta_x \right] \right\}, \end{aligned}$$

$$\text{where } \theta = y_x, \quad f(\theta) = \frac{1}{\sqrt{1 + \theta^2}} = \cos \phi.$$

This equation is invariant under Euclidean isometries. By way of contrast, the small-slope approximation $f = 1$ gives the linear fourth-order diffusion equation

$$y_t = -B y_{xxxx}$$

that is not invariant under rotations in the (x,y) plane.

2. INTEGRABLE NONLINEAR MODELS.

A rotation transforms the linear equation to a nonlinear equation of the form (3) with $f(\theta) = \alpha/(\beta + \theta)$. This is a useful integrable nonlinear model, since exact solutions can be constructed when $f(\theta)$ approximates the isotropic version at both small slopes and large slopes. These solutions are exact solutions for surface diffusion on a non-isotropic material, which in general leads to a fourth-order nonlinear diffusion equation of the form

$$(4) \quad \theta_t = -\partial_x^2 \{D(\theta) \partial_x [E(\theta) \theta_x]\}.$$

The surface of the recently solidified material is assumed to be horizontal and flat, with initial condition

$$(5) \quad \theta(x, 0) = 0.$$

Just as on a material surface, within the disordered region at a grain boundary, atoms are at a higher energy state than in the crystal lattice. This gives rise to a grain boundary tension γ_b , just as for surface tension γ_s , has the units of energy per unit area or force per unit length. The groove angle is such that the grain boundary tension balances surface tension on both arms of the groove. Hence for a symmetric groove centred at $x = 0$,

$$\gamma_b = 2\gamma_s \sin(\phi).$$

This leads to the boundary condition

$$(6) \quad \theta(0, t) = m = \left[\left(\frac{2\gamma_s}{\gamma_b} \right)^2 - 1 \right]^{-1/2}.$$

For a symmetric groove, there must be zero mass flux in either direction out of the groove, implying

$$(7) \quad \partial_x [E(\theta) \theta_x] = 0, \quad x = 0.$$

Finally, far from the grain boundary, the initial condition is not disturbed, so

$$(8) \quad \theta(x, t) \rightarrow 0, \quad x \rightarrow 0,$$

$$(9) \quad \text{and } \theta_x(x, t) \rightarrow 0, \quad x \rightarrow 0.$$

The balance between grain boundary tension and surface tension is depicted in Figure 1.

The system (4)–(9) is the initial-boundary problem for evolution of a grain boundary by surface diffusion. For a near-isotropic material, this problem was solved exactly in [4] by approximating $f(\theta)$ by a reciprocal linear spline $f(\theta) = \alpha_i/(\beta_i + \theta)$ between node points $\theta_{i-1} \leq \theta \leq \theta_i$ for $i = 1, \dots, N$. In practice, increasing the number of spline segments made little difference to the solution when N was increased from 4 to 16. The spline method can be used for this particular problem because it has a similarity solution of the form $\theta = g(xt^{-1/4})$. It then follows that the location of the node value $\theta = \theta_i$ is $g^{-1}(\theta_i)t^{1/4}$.

It is desirable to be able to solve some form of the anisotropic surface diffusion equation for other useful boundary conditions that are not compatible with the similarity reduction. Then the location of the node values can no longer be determined

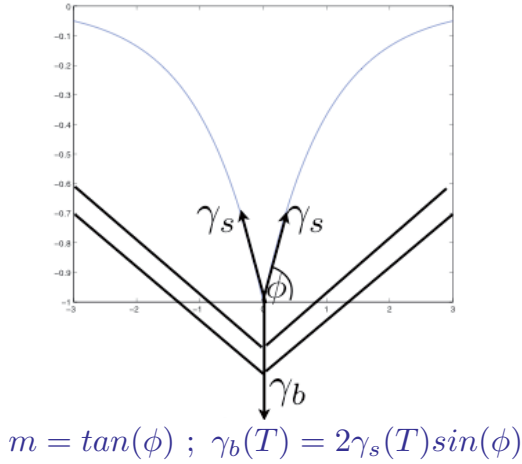


FIGURE 1. Balance between grain boundary tension and surface tension.

by elementary methods, so the spline representation of $D(\theta)$ and $E(\theta)$ can no longer be used. Nevertheless the integrable model $D(\theta) = \beta/(\beta + \theta)$, $E(\theta) = E_0\beta^3/(\beta + \theta)^3$, still gives a reasonable representation of a near-isotropic material over a wider range of inclination angles ϕ , than does the linear model. Since it can be easily transformed to the linear model, it can be solved exactly for a variety of initial and boundary conditions. The next problem to be solved, has a time dependent slope $m(t)$ prescribed at $x = 0$. The dihedral angle of the groove may be controlled by heating or cooling. As the solid surface cools, surface tension will increase, so that the equilibrium slope will decrease. In the simplest generalisation, the expression (1 for surface energy has an extra factor $\xi(T)$ that depends on temperature T . After defining a new time-like coordinate

$$\tau = \frac{1}{\nu k} \int_0^t \frac{\xi(T(t_1))}{T(t_1)} dt_1,$$

the surface diffusion equation is still autonomous, reducing again to (4) but with τ replacing t . After rotation by angle $\cot^{-1} \beta$, the integrable model transforms to the linear fourth-order diffusion equation $\bar{y}_\tau = -\bar{y}_{\bar{x}\bar{x}\bar{x}\bar{x}}$. When m is time dependent, the solution $\bar{y}(\bar{x}, \tau)$ can no longer be a function of the scaling invariant $X = \bar{x}\tau^{-1/2}$. However \bar{y} may be conveniently expanded as a series of separated solutions $\tau^{i/4}$ multiplying a function of X that is expressed in terms of generalised hypergeometric functions.

$$\begin{aligned} \bar{y} = g_0(X) + \sum_{j=1}^{\infty} \tau^{j/4} \Big[& K_{1j} {}_1F_3 \left(\frac{-j}{4}; \left[\frac{1}{4}, \frac{1}{2}, \frac{3}{4} \right], \frac{X^4}{256} \right) + K_{2j} X {}_1F_3 \left(\frac{1}{4} - \frac{j}{4}; \left[\frac{1}{2}, \frac{3}{4}, \frac{5}{4} \right], \frac{X^4}{256} \right) \\ & + K_{3j} X^2 {}_1F_3 \left(\frac{1}{2} - \frac{j}{4}; \left[\frac{3}{4}, \frac{5}{4}, \frac{3}{2} \right], \frac{X^4}{256} \right) + K_{4j} X^3 {}_1F_3 \left(\frac{3}{4} - \frac{j}{4}; \left[\frac{5}{4}, \frac{3}{2}, \frac{7}{4} \right], \frac{X^4}{256} \right) \Big]. \end{aligned}$$

When $m(\tau)$ is an analytic function in $\tau^{1/4}$, the boundary $x = 0$ can be specified as \bar{x} being a power series in $\tau^{1/4}$,

$$\bar{x} = \beta \tau^{1/4} \sum_{i=0}^{\infty} b_i \tau^{i/4}.$$

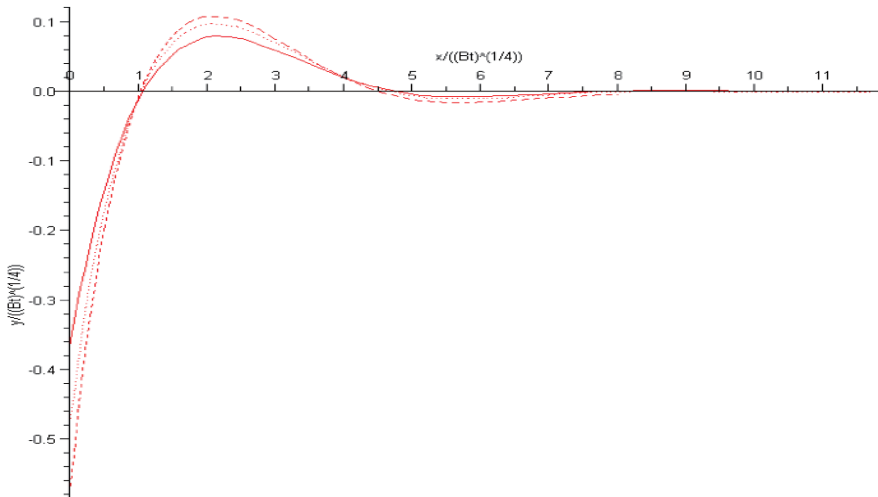


FIGURE 2. Groove with slope $m = 0.5 + 0.5\sqrt{\tau}$ at the root. Output times are $\tau = 0.0002, 0.1$ and 1.0

The coefficients b_i and K_{ij} are then uniquely determined by the boundary conditions. This solution method was completed fully for the steepening groove $m = 0.5 + 0.5\tau^{1/4}$ by Broadbridge and Goard [5]. This is shown here in Figure 2.

3. METHOD OF LINES WITH CENTRAL FINITE DIFFERENCES

Although it solves a very challenging problem, the exact solution method is complicated even after a minor change to the boundary conditions. We need also to have a back-up numerical method that can easily handle a variety of boundary conditions. One standard approach that is relatively easy to implement is the method of lines that constructs a semi-discrete model by central finite differencing of spatial derivatives. The resulting system of ordinary differential equations may be run through a numerical solver for stiff systems. For a uniform grid with spacing h , at $x = jh$, the approximate second and fourth derivatives are

$$\frac{\partial^2 \theta}{\partial x^2} = \frac{\theta_{j-1} - 2\theta_j + \theta_{j+1}}{h^2} + \mathcal{O}(h^2) \quad \text{and} \\ \frac{\partial^4 \theta}{\partial x^4} = \frac{\theta_{j-2} - 4\theta_{j-1} + 6\theta_j - 4\theta_{j+1} + \theta_{j+2}}{h^4} + \mathcal{O}(h^2).$$

The boundary at infinity is replaced by a boundary at some moderately large value $x = Nh$, where the same boundary conditions are assumed as before. At each of the boundaries $x = 0$ and $x = Nh$, the second-order boundary conditions for θ are implemented by introducing one fictitious grid point x_{-1} or x_{N+1} . However the initial and boundary conditions on an isotropic material for the grain boundary with constant dihedral angle, together imply a quadratic equation for $\theta_{-1}(0)$:

$$-3m\theta_{-1}^2 + 4(1 + m^2)\theta_{-1} - 8m(1 + m^2) = 0.$$

This does not have a real solution unless $m < 1/\sqrt{5}$. This is despite the finite real solution of the original continuum model having been constructed for an arbitrary

groove slope, even for an infinite slope of a cuspid groove. This problem with finite differencing [6] arises only for higher-order nonlinear PDEs with initial and boundary conditions with a corner singularity at $(x, t) = (0, 0)$. The boundary and initial conditions for the integral y of θ do not have such a singularity. The flux condition at $x = 0$ is now third-order in $y(x, t)$, for which we incorporate two fictitious grid points at $x = -h, -2h$. The boundary and initial conditions now imply a unique solution for $y_{-1}(0)$ and $y_{-2}(0)$. The real solution can be constructed for all later times, except that the zero-flux boundary condition at a finite value of x eventually leads to an unacceptable errors.

REFERENCES

- [1] Institute of Mathematics for Industry, Kyushu University Web Page:
<http://www.imi.kyushu-u.ac.jp/>
- [2] C. Herring. Surface tension as a motivation for sintering. In: W. E. Kingston (ed) The physics of powder metallurgy. McGraw-Hill, New York, 1951.
- [3] W. W. Mullins. Theory of thermal grooving. J. Appl. Phys. vol. 28 (pp. 333–339), 1957.
- [4] P. Tritscher and P. Broadbridge. Grain boundary grooving by surface diffusion: an analytic non-linear model for a symmetric groove. Proc. R. Soc. Lond. A vol. 450 (pp. 569–587), 1995.
- [5] P. Broadbridge and J. M. Goard. Temperature-dependent surface diffusion near a grain boundary. J. Eng. Math. vol. 66 (pp. 87–102), 2010.
- [6] P. Broadbridge and J. M. Goard. When central finite differencing gives complex values for a real solution!, Complex Variables and Elliptic Equations, vol. 57 (parts 2–4)(pp. 455–467), 2012. DOI: 10.1080/17476933.2011.647003

Viscoelastic Flows Generated by Vibrating Nanoscale Structures in Simple Liquids

John E. Sader

School of Mathematics and Statistics, The University of Melbourne, Victoria, 3010
Email jsader@unimelb.edu.au

The mechanical vibration of nanostructures in simple liquids is explored using measurement and theory. Their high resonant frequencies ($>20\text{GHz}$) probe the incompressible or compressible viscoelastic response of the liquid, depending on the structure's geometry.

1. INTRODUCTION

A fluid is said to be Newtonian if it exhibits a simple linear relationship between shear stress and strain rate. Simple liquids, such as water and glycerol, exhibit “relaxation times” on the order of $1\text{ ps} - 1\text{ ns}$ [1, 2] that are very short compared to the time scales associated with the motion of macroscopic objects in fluids. This allows interactions between solid structures and simple fluids to be described by classical Navier–Stokes treatments. Non-Newtonian fluid mechanics is normally associated only with complex fluids that have long relaxation times, such as polymer solutions and melts, dense colloidal suspensions such as corn starch in water, and fluids near their phase transitions. Scaling objects down to nanometre size scales increases their characteristic vibrational frequencies up to the GHz or THz range [3, 4]. Fluid-structure interactions on these length scales thus have the potential to show significant deviations from Newtonian behaviour, even for simple liquids.

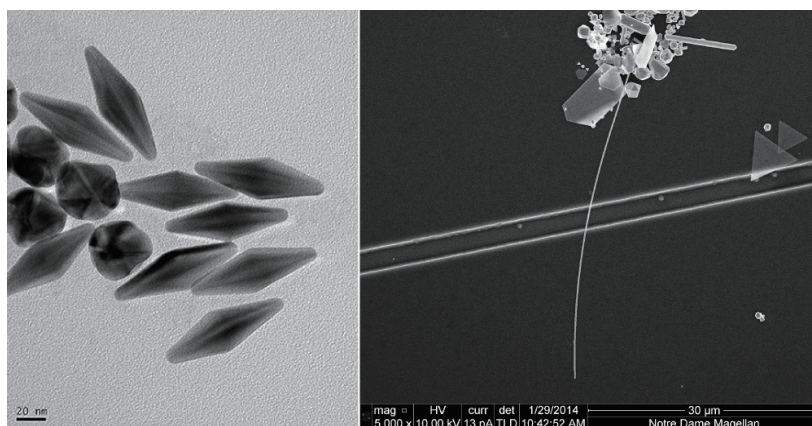


FIGURE 1. TEM images of (left) bi-pyramidal gold nanoparticles, (right) single gold nanowires.

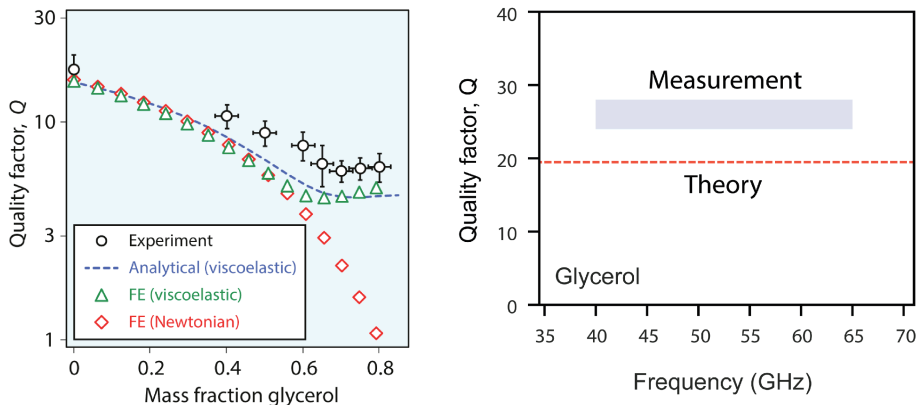


FIGURE 2. Comparison of theory and measurement (left) bipyramidal particles, (right) nanowires.

2. MEASUREMENTS

Here, we measure and theoretically characterise the vibration response of (i) a suspension of bipyramidal gold nanoparticles [5], (ii) single gold nanowires [6] in nominally Newtonian fluids. TEM images of the nanostructures are given in Fig. 1. We examine the acoustic vibrational modes of both types of nanostructures, in a range of liquids, using transient absorption spectroscopy — where laser pulses are used to excite and interrogate the structure’s motion [3, 4]. This launches predominantly extensional mode vibrations in the bipyramidal particles, and breathing modes in the nanowires. These complementary motions dramatically modify the fluid motion, and allow us to probe both incompressible and compressible flows.

3. THEORETICAL MODELS AND RESULTS

Theoretical models describing the viscoelastic response of simple liquids are presented for both incompressible and compressible flows. Fluid-structure viscoelastic simulations for incompressible flow are compared to measurements on the bipyramidal particles in glycerol–water mixtures, and to those obtained using the (Newtonian) Navier–Stokes equations. The latter framework, which is used widely in MEMS and NEMS design, does not predict measurements in the high viscosity regime. In contrast, the incompressible viscoelastic model naturally describes the observed behaviour; see Fig. 2 (left).

Many different constitutive models exist for compressible viscoelastic flows. We show that all available models for these flows, with the exception of a very recent proposal, do not reproduce the required response at high frequency [7]. Results obtained using different previous models are compared to highlight this issue. We demonstrate the utility of the recent model that does capture the required high-frequency behaviour, using measurements of the breathing mode vibrations of single gold nanowires immersed in glycerol, over the 40–70 GHz frequency range; see Fig. 2 (right).

This work is performed in collaboration with Debadi Chakraborty and Naida Lacevic from the University of Melbourne, Matthew Pelton from the University of Maryland, Baltimore County (USA), Edward Malachosky and Philippe Guyot-Sionnest from the

University of Chicago (USA), Todd A. Major, Mary Sajini Devadas and Gregory V. Hartland from the University of Notre Dame (USA).

4. ACKNOWLEDGEMENTS

We thank D. Gosztola for valuable assistance with the transient-absorption measurements. This work was performed, in part, at the Center for Nanoscale Materials, a U.S. Department of Energy, Office of Science, Office of Basic Energy Sciences User Facility under Contract No. DE-AC02-06CH11357. It was supported by Caltech's Kavli Nanoscience Institute, NSF Grant Nos. CHE-1110560 and CHE1111799, the Office of Naval Research (Award No. N00014-12-1-1030), and the University of Notre Dame Strategic Research Initiative. The authors gratefully acknowledge support of the Australian Research Council Grants Scheme.

REFERENCES

- [1] W. M. Slie, A. R. Donfor, and T. A. Litovitz, "Ultrasonic shear and longitudinal measurements in aqueous glycerol," *J. Chem. Phys.*, Vol. 44, pp. 3712–3718 (1966).
- [2] G. Maisano, P. Migliardo, F. Aliotta, C. Vasi, F. Wanderlingh, and G. D'Arrigo, "Evidence of anomalous acoustic behavior from Brillouin scattering in supercooled Water," *Phys. Rev. Lett.*, Vol. 52, pp. 1025–1018 (1984).
- [3] G. V. Hartland, "Coherent excitation of vibrational modes in metallic nanoparticles", *Annu. Rev. Phys. Chem.*, Vol. 57, pp. 403–430 (2006).
- [4] M. Pelton, J. E. Sader, J. Burgin, M. Liu, P. Guyot-Sionnest, and D. Gosztola, "Damping of acoustic vibrations in gold nanoparticles", *Nat. Nanotechnol.*, Vol. 4, pp. 492–495 (2009).
- [5] M. Pelton, D. Chakraborty, E. Malachosky, P. Guyot-Sionnest, and J. E. Sader, "Viscoelastic flows in simple liquids generated by vibrating nanostructures", *Phys. Rev. Lett.*, Vol. 111, 244502 (2013).
- [6] K. Yu, T. A. Major, D. Chakraborty, M. S. Devadas, J. E. Sader and G. V. Hartland, "Compressible viscoelastic liquid effects generated by the breathing modes of isolated metal nanostructures", *Nano Letters*, Vol. 15, pp. 3964–3970 (2015).
- [7] D. Chakraborty and J. E. Sader, "Constitutive models for linear compressible viscoelastic flows of simple liquids at nanometer length scales", *Phys. Fluids*, Vol. 27, 052002 (2015).

Application of the non-equilibrium Green's function method in the design of nanoelectronic devices

Aleksandar Staykov

International Institute for Carbon Neutral Energy Research,
Kyushu University, Japan

With the advance of miniaturization the size of electric circuit components rapidly approaches the scale of a few to several tenths of nanometers. In 2012 the leading electronic manufactures reported CPUs with elements size of 18 nm. Any further downscaling in size will lead not only to smaller devices but also to a smooth transition between the laws of classical mechanics which govern macroscopic objects to the laws of quantum mechanics which describe the properties of molecules, atoms, and subatomic particles. Many macroscopic concepts like the band structure, Ohm's law, conductivity, etc., would be replaced by their quantum mechanical equivalents like discrete molecular energy spectra, ballistic transport, conductance, tunneling, etc. All these concepts should be properly applied in the design of novel current controlling elements such as switches, diodes, and transistors.

The large amount of the reported experimental data led to the necessity of adequate theoretical models, which can deal with the single molecule electron transport. That model should provide explanation for the observed results and should suggest reasonable predictions able to lead the experimental research. In the macroscopic world, the conductance (g) is defined by Ohm's law and is proportional to the area (A) of the conductor, which is perpendicular to the direction of the current, and inverse to its length (L).

$$(1) \quad g = \sigma \frac{A}{L}$$

In eq. 1 with σ is denoted the conductivity, which is a material specific property. The conductivity provides important information for the free path of the electrons before they collide with ions from the crystal lattice. Hence, Ohm's law holds true for conductors with length many times longer than the "free path" of the electrons. Within molecular device scale, the wave function of an electron, which resides within the source electrode, has small amplitude on the drain electrode and there exists a finite possibility for tunneling between the source and the drain. That possibility will increase when a conductance channel, i.e., an atom or a molecule, is placed in the gap between the electrodes.

For such a conductor the electron will not encounter any collisions with the atoms of the molecule, since its "free path" will be longer than the length of the conductor itself. The described electron transport is called ballistic and has several important

consequences. For ballistic conductors the conductivity cannot be defined and the conductance does not follow Ohm's law dependence from the length of the channel. The ballistic electron transport excludes the possibility of collisions between the electrons and the atoms of the molecule, which means that the resistance for the current is the interface between the conductor and the electrodes. Another consequence from the lack of collisions within the channel is that the electrons do not transfer vibrational energy to the atoms, hence there is no heating of the molecule and the electrons are not losing their phase, e.g., coherent regime of electron transport. The steady-state current through a nanoscale system is given with eq. 2.

$$(2) \quad I = \frac{2e}{h} \int_{-\infty}^{+\infty} T(E) [f(E - \mu_L) - f(E - \mu_R)] dE$$

In eq. 2 with e is denoted the electron charge, with f the Fermi function of the electrodes, with μ_L and μ_R the chemical potential at the left and the right electrodes, respectively, and with $T(E)$ is denoted the transmission probability as a function of electron energy. The transmission probability is given with the following equation:

$$(3) \quad T(E) = [\Gamma_L G^L \Gamma_R G^A]$$

In eq. 3 with G^A and G^R are denoted the advanced and the retarded Green's functions, respectively. With Γ_L and Γ_R are denoted the broadening functions of the electrodes. It is worth noting that the transmission probability is a function of electron energy and applied bias. Thus, the computed zero-bias transmission probability will be different from those for applied biases.

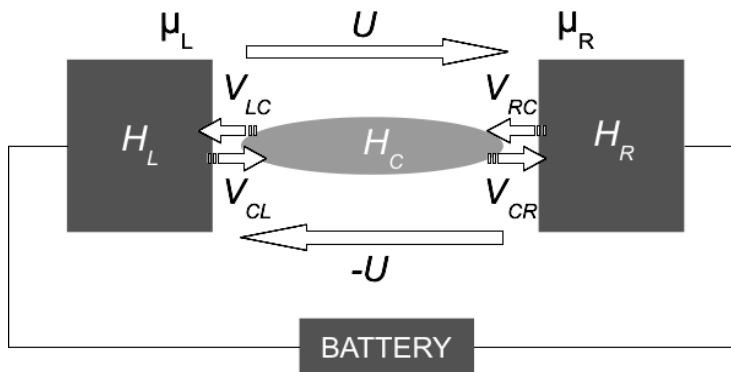


FIGURE 1. Schematic presentation of nano-device in ballistic electron transport regime, treated computationally by the NEGF method.

The non-equilibrium Green's function formalism (NEGF) is used to describe the ballistic electron transport through a many particle system. For the system shown in Figure 1 with H_C is denoted the Hamiltonian matrix of the channel, with H_L and H_R

are denoted the Hamiltonian matrices of the left and the right electrodes, and with U the potential due to the external electric field induced between the electrodes. V_{CL} and V_{LC} denote the interaction matrices between the left electrode and the channel. V_{CR} and V_{RC} denote the interaction matrices between the right electrode and the channel.

The non-equilibrium Green's method was successfully applied for the design of novel nanographene based [1] and molecular diodes [2, 3], photoresistive molecular devices and photoswitching molecules for control of logical operations at molecular level [4, 5, 6]. The method was also applied for the understanding and analysis of electron transport through complex biomolecules and DNA sequences [7].

REFERENCES

- [1] Staykov, A.; Tzenov, P. J. Phys. Chem. C, 2013, 117, 13644
- [2] Staykov, A.; Li, X.; Tsuji, Y.; Yoshizawa, K. J. Phys. Chem. C, 2012, 116, 18451
- [3] Staykov, A.; Nozaki, D.; Yoshizawa, K. J. Phys. Chem. C, 2007, 111, 11699
- [4] Staykov, A.; Watanabe, M.; Ishihara, T.; Yoshizawa, K. J. Phys. Chem. C, 2014, 118, 27539
- [5] Staykov, A.; Nozaki, D.; Yoshizawa, K.; J. Phys. Chem. C, 2007, 111, 3517
- [6] Staykov, A.; Areephong, J.; Browne, W. R.; Feringa, B. L.; Yoshizawa, K. ACS Nano, 2011, 5, 1165
- [7] Staykov, A.; Tsuji, Y.; Yoshizawa, K. J. Phys. Chem. C, 2011, 115, 3481

MI レクチャーノートシリーズ刊行にあたり

本レクチャーノートシリーズは、文部科学省 21 世紀 COE プログラム「機能数理学の構築と展開」(H.15-19 年度)において作成した COE Lecture Notes の続刊であり、文部科学省大学院教育改革支援プログラム「産業界が求める数学博士と新修士養成」(H19-21 年度)および、同グローバル COE プログラム「マス・フォア・インダストリ教育研究拠点」(H.20-24 年度)において行われた講義の講義録として出版されてきた。平成 23 年 4 月のマス・フォア・インダストリ研究所 (IMI) 設立と平成 25 年 4 月の IMI の文部科学省共同利用・共同研究拠点として「産業数学の先進的・基礎的共同研究拠点」の認定を受け、今後、レクチャーノートは、マス・フォア・インダストリに関わる国内外の研究者による講義の講義録、会議録等として出版し、マス・フォア・インダストリの本格的な展開に資するものとする。

平成 26 年 10 月

マス・フォア・インダストリ研究所
所長 福本康秀

IMI-La Trobe Joint Conference **Mathematics for Materials Science and Processing**

発行 2016年2月5日
編集 九州大学マス・フォア・インダストリ研究所 オーストラリア分室
発行 九州大学マス・フォア・インダストリ研究所
九州大学大学院数理学府
〒819-0395 福岡市西区元岡744
九州大学数理・IMI 事務室
TEL 092-802-4402 FAX 092-802-4405
URL <http://www.imi.kyushu-u.ac.jp/>

印刷 城島印刷株式会社
〒810-0012 福岡市中央区白金 2 丁目 9 番 6 号
TEL 092-531-7102 FAX 092-524-4411

シリーズ既刊

Issue	Author／Editor	Title	Published
COE Lecture Note	Mitsuhiro T. NAKAO Kazuhiro YOKOYAMA	Computer Assisted Proofs - Numeric and Symbolic Approaches - 199pages	August 22, 2006
COE Lecture Note	M.J.Shai HARAN	Arithmetical Investigations - Representation theory, Orthogonal polynomials and Quantum interpolations- 174pages	August 22, 2006
COE Lecture Note Vol.3	Michal BENES Masato KIMURA Tatsuyuki NAKAKI	Proceedings of Czech-Japanese Seminar in Applied Mathematics 2005 155pages	October 13, 2006
COE Lecture Note Vol.4	宮田 健治	辺要素有限要素法による磁界解析 - 機能数理学特別講義 21pages	May 15, 2007
COE Lecture Note Vol.5	Francois APERY	Univariate Elimination Subresultants - Bezout formula, Laurent series and vanishing conditions - 89pages	September 25, 2007
COE Lecture Note Vol.6	Michal BENES Masato KIMURA Tatsuyuki NAKAKI	Proceedings of Czech-Japanese Seminar in Applied Mathematics 2006 209pages	October 12, 2007
COE Lecture Note Vol.7	若山 正人 中尾 充宏	九州大学産業技術数理研究センター キックオフ ミーティング 138pages	October 15, 2007
COE Lecture Note Vol.8	Alberto PARMEGGIANI	Introduction to the Spectral Theory of Non-Commutative Harmonic Oscillators 233pages	January 31, 2008
COE Lecture Note Vol.9	Michael I.TRIBELSKY	Introduction to Mathematical modeling 23pages	February 15, 2008
COE Lecture Note Vol.10	Jacques FARAUT	Infinite Dimensional Spherical Analysis 74pages	March 14, 2008
COE Lecture Note Vol.11	Gerrit van DIJK	Gelfand Pairs And Beyond 60pages	August 25, 2008
COE Lecture Note Vol.12	Faculty of Mathematics, Kyushu University	Consortium “MATH for INDUSTRY” First Forum 87pages	September 16, 2008
COE Lecture Note Vol.13	九州大学大学院 数理学研究院	プロシーディング「損保数理に現れる確率モデル」 — 日新火災・九州大学 共同研究 2008 年 11 月 研究会 — 82pages	February 6, 2009

シリーズ既刊

Issue	Author／Editor	Title	Published
COE Lecture Note Vol.14	Michal Beneš, Tohru Tsujikawa Shigetoshi Yazaki	Proceedings of Czech-Japanese Seminar in Applied Mathematics 2008 77pages	February 12, 2009
COE Lecture Note Vol.15	Faculty of Mathematics, Kyushu University	International Workshop on Verified Computations and Related Topics 129pages	February 23, 2009
COE Lecture Note Vol.16	Alexander Samokhin	Volume Integral Equation Method in Problems of Mathematical Physics 50pages	February 24, 2009
COE Lecture Note Vol.17	矢嶋 徹 及川 正行 梶原 健司 辻 英一 福本 康秀	非線形波動の数理と物理 66pages	February 27, 2009
COE Lecture Note Vol.18	Tim Hoffmann	Discrete Differential Geometry of Curves and Surfaces 75pages	April 21, 2009
COE Lecture Note Vol.19	Ichiro Suzuki	The Pattern Formation Problem for Autonomous Mobile Robots —Special Lecture in Functional Mathematics— 23pages	April 30, 2009
COE Lecture Note Vol.20	Yasuhide Fukumoto Yasunori Maekawa	Math-for-Industry Tutorial: Spectral theories of non-Hermitian operators and their application 184pages	June 19, 2009
COE Lecture Note Vol.21	Faculty of Mathematics, Kyushu University	Forum "Math-for-Industry" Casimir Force, Casimir Operators and the Riemann Hypothesis 95pages	November 9, 2009
COE Lecture Note Vol.22	Masakazu Suzuki Hoon Hong Hirokazu Anai Chee Yap Yousuke Sato Hiroshi Yoshida	The Joint Conference of ASCM 2009 and MACIS 2009: Asian Symposium on Computer Mathematics Mathematical Aspects of Computer and Information Sciences 436pages	December 14, 2009
COE Lecture Note Vol.23	荒川 恒男 金子 昌信	多重ゼータ値入門 111pages	February 15, 2010
COE Lecture Note Vol.24	Fulton B.Gonzalez	Notes on Integral Geometry and Harmonic Analysis 125pages	March 12, 2010
COE Lecture Note Vol.25	Wayne Rossman	Discrete Constant Mean Curvature Surfaces via Conserved Quantities 130pages	May 31, 2010
COE Lecture Note Vol.26	Mihai Ciucu	Perfect Matchings and Applications 66pages	July 2, 2010

シリーズ既刊

Issue	Author／Editor	Title	Published
COE Lecture Note Vol.27	九州大学大学院 数理学研究院	Forum “Math-for-Industry” and Study Group Workshop Information security, visualization, and inverse problems, on the basis of optimization techniques 100pages	October 21, 2010
COE Lecture Note Vol.28	ANDREAS LANGER	MODULAR FORMS, ELLIPTIC AND MODULAR CURVES LECTURES AT KYUSHU UNIVERSITY 2010 62pages	November 26, 2010
COE Lecture Note Vol.29	木田 雅成 原田 昌晃 横山 俊一	Magma で広がる数学の世界 157pages	December 27, 2010
COE Lecture Note Vol.30	原 隆 松井 卓 廣島 文生	Mathematical Quantum Field Theory and Renormalization Theory 201pages	January 31, 2011
COE Lecture Note Vol.31	若山 正人 福本 康秀 高木 剛 山本 昌宏	Study Group Workshop 2010 Lecture & Report 128pages	February 8, 2011
COE Lecture Note Vol.32	Institute of Mathematics for Industry, Kyushu University	Forum “Math-for-Industry” 2011 “TSUNAMI-Mathematical Modelling” Using Mathematics for Natural Disaster Prediction, Recovery and Provision for the Future 90pages	September 30, 2011
COE Lecture Note Vol.33	若山 正人 福本 康秀 高木 剛 山本 昌宏	Study Group Workshop 2011 Lecture & Report 140pages	October 27, 2011
COE Lecture Note Vol.34	Adrian Muntean Vladimír Chalupecký	Homogenization Method and Multiscale Modeling 72pages	October 28, 2011
COE Lecture Note Vol.35	横山 俊一 夫 紀恵 林 卓也	計算機代数システムの進展 210pages	November 30, 2011
COE Lecture Note Vol.36	Michal Beneš Masato Kimura Shigetoshi Yazaki	Proceedings of Czech-Japanese Seminar in Applied Mathematics 2010 107pages	January 27, 2012
COE Lecture Note Vol.37	若山 正人 高木 剛 Kirill Morozov 平岡 裕章 木村 正人 白井 朋之 西井 龍映 柴 伸一郎 穴井 宏和 福本 康秀	平成 23 年度 数学・数理科学と諸科学・産業との連携研究ワーク ショップ 拡がっていく数学 ～期待される“見えない力”～ 154pages	February 20, 2012

シリーズ既刊

Issue	Author／Editor	Title	Published
COE Lecture Note Vol.38	Fumio Hiroshima Itaru Sasaki Herbert Spohn Akito Suzuki	Enhanced Binding in Quantum Field Theory 204pages	March 12, 2012
COE Lecture Note Vol.39	Institute of Mathematics for Industry, Kyushu University	Multiscale Mathematics; Hierarchy of collective phenomena and interrelations between hierarchical structures 180pages	March 13, 2012
COE Lecture Note Vol.40	井ノ口順一 太田 泰広 寛 三郎 梶原 健司 松浦 望	離散可積分系・離散微分幾何チュートリアル 2012 152pages	March 15, 2012
COE Lecture Note Vol.41	Institute of Mathematics for Industry, Kyushu University	Forum “Math-for-Industry” 2012 “Information Recovery and Discovery” 91pages	October 22, 2012
COE Lecture Note Vol.42	佐伯 修 若山 正人 山本 昌宏	Study Group Workshop 2012 Abstract, Lecture & Report 178pages	November 19, 2012
COE Lecture Note Vol.43	Institute of Mathematics for Industry, Kyushu University	Combinatorics and Numerical Analysis Joint Workshop 103pages	December 27, 2012
COE Lecture Note Vol.44	萩原 学	モダン符号理論からポストモダン符号理論への展望 107pages	January 30, 2013
COE Lecture Note Vol.45	金山 寛	Joint Research Workshop of Institute of Mathematics for Industry (IMI), Kyushu University “Propagation of Ultra-large-scale Computation by the Domain-decomposition-method for Industrial Problems (PUCDIP 2012)” 121pages	February 19, 2013
COE Lecture Note Vol.46	西井 龍映 栄 伸一郎 岡田 勘三 落合 啓之 小磯 深幸 斎藤 新悟 白井 朋之	科学・技術の研究課題への数学アプローチ —数学モデリングの基礎と展開— 325pages	February 28, 2013
COE Lecture Note Vol.47	SOO TECK LEE	BRANCHING RULES AND BRANCHING ALGEBRAS FOR THE COMPLEX CLASSICAL GROUPS 40pages	March 8, 2013
COE Lecture Note Vol.48	溝口 佳寛 脇 隼人 平坂 貢 谷口 哲至 島袋 修	博多ワークショップ「組み合わせとその応用」 124pages	March 28, 2013

シリーズ既刊

Issue	Author／Editor	Title	Published
COE Lecture Note Vol.49	照井 章 小原 功任 濱田 龍義 横山 俊一 穴井 宏和 横田 博史	マス・フォア・インダストリ研究所 共同利用研究集会 II 数式処理研究と産学連携の新たな発展 137pages	August 9, 2013
MI Lecture Note Vol.50	Ken Anjyo Hiroyuki Ochiai Yoshinori Dobashi Yoshihiro Mizoguchi Shizuo Kaji	Symposium MEIS2013: Mathematical Progress in Expressive Image Synthesis 154pages	October 21, 2013
MI Lecture Note Vol.51	Institute of Mathematics for Industry, Kyushu University	Forum “Math-for-Industry” 2013 “The Impact of Applications on Mathematics” 97pages	October 30, 2013
MI Lecture Note Vol.52	佐伯 修 岡田 勘三 高木 剛 若山 正人 山本 昌宏	Study Group Workshop 2013 Abstract, Lecture & Report 142pages	November 15, 2013
MI Lecture Note Vol.53	四方 義啓 櫻井 幸一 安田 貴徳 Xavier Dahan	平成25年度 九州大学マス・フォア・インダストリ研究所 共同利用研究集会 安全・安心社会基盤構築のための代数構造 ～サイバー社会の信頼性確保のための数理学～ 158pages	December 26, 2013
MI Lecture Note Vol.54	Takashi Takiguchi Hiroshi Fujiwara	Inverse problems for practice, the present and the future 93pages	January 30, 2014
MI Lecture Note Vol.55	栄 伸一郎 溝口 佳寛 脇 隼人 洪田 敬史	Study Group Workshop 2013 数学協働プログラム Lecture & Report 98pages	February 10, 2014
MI Lecture Note Vol.56	Yoshihiro Mizoguchi Hayato Waki Takafumi Shibuta Tetsuji Taniguchi Osamu Shimabukuro Makoto Tagami Hirotake Kurihara Shuya Chiba	Hakata Workshop 2014 ～ Discrete Mathematics and its Applications ～ 141pages	March 28, 2014
MI Lecture Note Vol.57	Institute of Mathematics for Industry, Kyushu University	Forum “Math-for-Industry” 2014: “Applications + Practical Conceptualization + Mathematics = fruitful Innovation” 93pages	October 23, 2014
MI Lecture Note Vol.58	安生健一 落合啓之	Symposium MEIS2014: Mathematical Progress in Expressive Image Synthesis 135pages	November 12, 2014

シリーズ既刊

Issue	Author／Editor	Title	Published
MI Lecture Note Vol.59	西井 龍映 岡田 勘三 梶原 健司 高木 剛 若山 正人 脇 隼人 山本 昌宏	Study Group Workshop 2014 数学協働プログラム Abstract, Lecture & Report 196pages	November 14, 2014
MI Lecture Note Vol.60	西浦 博	平成 26 年度九州大学 IMI 共同利用研究・研究集会 (I) 感染症数理モデルの実用化と産業及び政策での活用のための新 たな展開 120pages	November 28, 2014
MI Lecture Note Vol.61	溝口 佳寛 Jacques Garrigue 萩原 学 Reynald Affeldt	研究集会 高信頼な理論と実装のための定理証明および定理証明器 Theorem proving and provers for reliable theory and implementations (TPP2014) 138pages	February 26, 2015
MI Lecture Note Vol.62	白井 朋之	Workshop on “ β -transformation and related topics” 59pages	March 10, 2015
MI Lecture Note Vol.63	白井 朋之	Workshop on “Probabilistic models with determinantal structure” 107pages	August 20, 2015
MI Lecture Note Vol.64	落合 啓之 土橋 宜典	Symposium MEIS2015: Mathematical Progress in Expressive Image Synthesis 124pages	September 18, 2015
MI Lecture Note Vol.65	Institute of Mathematics for Industry, Kyushu University	Forum “Math-for-Industry” 2015 “The Role and Importance of Mathematics in Innovation” 74pages	October 23, 2015
MI Lecture Note Vol.66	岡田 勘三 藤澤 克己 白井 朋之 若山 正人 脇 隼人 Philip Broadbridge 山本 昌宏	Study Group Workshop 2015 Abstract, Lecture & Report 156pages	November 5, 2015



Institute of Mathematics for Industry
Kyushu University

九州大学マス・フォア・インダストリ研究所
九州大学大学院 数理学府

〒819-0395 福岡市西区元岡744 TEL 092-802-4402 FAX 092-802-4405
URL <http://www.imi.kyushu-u.ac.jp/>